MULTI-FIDELITY CONSTRUCTION OF EXPLICIT BOUNDARIES: APPLICATION TO AEROELASTICITY

by

Christoph Dribusch

A Dissertation Submitted to the Faculty of the

DEPARTMENT OF AEROSPACE AND MECHANICAL ENGINEERING

In Partial Fulfillment of the Requirements
For the Degree of

DOCTOR OF PHILOSOPHY
WITH A MAJOR IN MECHANICAL ENGINEERING

In the Graduate College

THE UNIVERSITY OF ARIZONA

2013

THE UNIVERSITY OF ARIZONA
GRADUATE COLLEGE

As members of the Dissertation Committee, we certify that we have read the dissertation prepared by Christoph Dribusch titled Multi-Fidelity Construction of Explicit Boundaries: Application to Aeroelasticity and recommend that it be accepted as fulfilling the dissertation requirement for the Degree of Doctor of Philosophy.

Samy Missoum — Date: April 17th, 2013

Parviz Nikravesh — Date: April 17th, 2013

Sergey Shkarayev — Date: April 17th, 2013

Jonathan Sprinkle — Date: April 17th, 2013

Final approval and acceptance of this dissertation is contingent upon the candidate's submission of the final copies of the dissertation to the Graduate College.
I hereby certify that I have read this dissertation prepared under my direction and recommend that it be accepted as fulfilling the dissertation requirement.

Dissertation Director: Samy Missoum — Date: April 17th, 2013

STATEMENT BY AUTHOR

This dissertation has been submitted in partial fulfillment of requirements for an advanced degree at the University of Arizona and is deposited in the University Library to be made available to borrowers under rules of the Library.

Brief quotations from this dissertation are allowable without special permission, provided that accurate acknowledgment of source is made. Requests for permission for extended quotation from or reproduction of this manuscript in whole or in part may be granted by the head of the major department or the Dean of the Graduate College when in his or her judgment the proposed use of the material is in the interests of scholarship. In all other instances, however, permission must be obtained from the author.

SIGNED: Christoph Dribusch

TABLE OF CONTENTS

TABLE OF CONTENTS – *Continued*

LIST OF FIGURES

LIST OF FIGURES – *Continued*

LIST OF FIGURES – *Continued*

LIST OF FIGURES – *Continued*

LIST OF FIGURES – *Continued*

LIST OF TABLES

ABSTRACT

Wings, control surfaces and rotor blades subject to aerodynamic forces may exhibit aeroelastic instabilities such as flutter, divergence and limit cycle oscillations which generally reduce their life and functionality. This possibility of instability must be taken into account during the design process and numerical simulation models may be used to predict aeroelastic stability.

Aeroelastic stability is a design requirement that encompasses several difficulties also found in other areas of design. For instance, the large computational time associated with stability analysis is also found in computational fluid dynamics (CFD) models. It is a major hurdle in numerical optimization and reliability analysis, which generally require large numbers of call to the simulation code. Similarly, the presence of bifurcations and discontinuities is also encountered in structural impact analysis based on nonlinear dynamic simulations and renders traditional approximation techniques such as Kriging ineffective. Finally, for a given component or system, aeroelastic instability is only one of multiple failure modes which must be accounted for during design and reliability studies.

To address the above challenges, this dissertation proposes a novel algorithm to predict, over a range of parameters, the qualitative outcomes (pass/fail) of simulations based on relatively few, classified (pass/fail) simulation results. This is different from traditional approximation techniques that seek to predict simulation outcomes quantitatively, for example by fitting a response surface. The predictions of the proposed algorithm are based on the theory of support vector machines (SVM), a machine learning method originated in the field of pattern recognition. This process yields an analytical function that explicitly defines the boundary between feasible and infeasible regions of the parameter space and has the ability to reproduce nonlinear, disjoint boundaries in n dimensions. Since training the SVM

only requires classification of training samples as feasible or infeasible, the presence of discontinuities in the simulation results does not affect the proposed algorithm. For the same reason, multiple failure modes such as aeroelastic stability, maximum stress or geometric constraints, may be represented by a single SVM predictor.

Often, multiple models are available to simulate a given design at different levels of fidelity and small improvements in accuracy may increase simulation cost by an order of magnitude. In many cases, a lower-fidelity model will classify a case correctly as feasible or infeasible. Therefore a multi-fidelity algorithm is proposed that takes advantage of lower-fidelity models when appropriate to minimize the overall computational burden of training the SVM. To this end, the algorithm combines the concepts of adaptive sampling and multi-fidelity analysis to iteratively select not only the training samples, but also the appropriate level of fidelity for evaluation.

The proposed algorithm, referred to as multi-fidelity explicit design space decomposition (MF-EDSD), is demonstrated on various models of aeroelastic stability to either build the stability boundary and/or to perform design optimization. The aeroelastic models range from linear and nonlinear analytical models to commercial software (ZAERO) and represent divergence, flutter, and limit cycle oscillation instabilities. Additional analytical test problems have the advantage that the accuracy of the SVM predictor and the convergence to optimal designs are more easily verified. On the other hand the more sophisticated models demonstrate the applicability to real aerospace applications where the solutions are not known a priori.

In conclusion, the presented MF-EDSD algorithm is well suited for approximating stability boundaries associated with aeroelastic instabilities in high-dimensional parameter spaces. The adaptive selection of training samples and use of multi-fidelity models leads to large reductions of simulation cost without sacrificing accuracy. The SVM representation of the boundary of the feasible design space provides a single differentiable constraint function with negligible evaluation cost, ideal for numerical optimization and reliability quantification.

CHAPTER 1

INTRODUCTION

In aerospace engineering, aeroelastic stability constraints present a difficult obstacle to simulation-based design methods such as numerical optimization and reliability analysis. Though simulation models exist to predict the stability of a design under given flight conditions, their evaluation is often computationally very expensive. In addition, aeroelasticity problems exhibit bifurcations and discontinuities. As such, they are representative of a class of design constraints characterized by high evaluation cost and non-smooth responses, also encountered, for example, in the evaluation of automobiles via crash test simulations.

Unlike the use of surrogates, which seek to approximate the model responses, this dissertation proposes a classification-based method to generalize the results of simulations based on their classification as feasible or infeasible. The advantages of this approach include its insensitivity to binary or discontinuous responses and the possibility of incorporating various different models into a single predictor of design feasibility. While previous work has presented algorithms for the selection of simulation cases in order to build and refine such predictors via support vector machines (SVM), the current work leverages the availability of various levels of fidelity. More precisely, during the computational design process, function evaluations are often preformed using higher fidelity models. While these models are typically more accurate, they are also more computationally intense. On the other hand, lower-fidelity models may provide large savings, while correctly classifying many designs as feasible or infeasible, thus providing valuable information. To explore the possible advantage of incorporating lower-fidelity results, this dissertation develops an algorithm for selecting appropriately lower or higher fidelity models to refine prediction models based on SVM. The proposed algorithm will be applied to the construction of aeroelastic stability boundaries.

In preparation of a more detailed treatment, the following sections highlight the concepts of aeroelastic stability and numerical design optimization before outlining the multi-fidelity approach of this work. In addition, an overview of subsequent chapters organizes this dissertation and its background, methodology and results sections.

1.1 Aeroelasticity

The study of aeroelasticity is concerned with flexible bodies subject to fluid flow. The air streaming around the body exerts aerodynamic forces, causing deflections, which in turn, alter the fluid flow. This interaction is the characteristic of aeroelasticity and allows for interesting system behavior, very relevant to several disciplines of engineering.

In aircraft design, aeroelasticity affects drag, lift, ride comfort and maneuverability. Results of aeroelastic analysis are required for structural design and control system design for example. Likewise, aeroelasticity must be taken into account when designing propellers and turbines to accurately predict performance and loading, affected by the flexibility of the fan blades. In reed instruments such as the clarinet, the airflow induces oscillations in a thin blade (reed), which are amplified in the resonating chamber to produce music. Electricity lines, tall buildings and suspension bridges are all susceptible to aeroelastic oscillations, causing noise, discomfort or even collapse as seen on the Tacoma-Narrows bridge in 1940.

The collapse of the Tacoma-Narrows bridge is a frequently cited example of the destructive forces of aeroelastic instabilities. The bridge was designed to easily withstand the aerodynamic forces in its undeformed state, but the feedback loop of air flow induced deformations and deformation induced variations of the air flow was not sufficiently understood. Under certain conditions this feedback loop was unstable and oscillations were amplified until structural failure occurred. With buildings, such aeroelastic instabilities are a rare exception, but airplane wings, being less rigid and exposed too much higher air speeds, are generally prone to this phenomenon.

Historically, aeroelastic instabilities of wings and control surfaces have been a great obstacle to building faster airplanes and most of the progress in aeroelasticity was motivated by aviation. For example, the transition from biplane aircraft to higher-performance monoplane designs in the 1920s was delayed by unexpected aeroelastic instabilities (static divergence) (Bhatia (2003)). Tragically, many lessons were learned too late: Crashes due to aeroelastic instabilities were responsible for hundreds of fatalities, primarily between 1920 and 1970. Since then, advances in the analysis and prediction of instabilities along with specialized flight testing improved safety tremendously.

Today, every aircraft design must undergo aeroelastic analysis to ensure its safety. Simulation models play an ever increasing role, but wind-tunnel and flight tests are still indispensable and likely will be for decades to come. Such wind-tunnel tests can easily cost millions of dollars and many months of development time (Bhatia (2003)) and ideally they are only used late in the design process to confirm simulation results. To this end, great effort has been invested in the improvement of accuracy and reliability of aeroelastic simulations and today, extensively verified, off-the-shelf software packages are available. Unfortunately, there is still room for improvement: In 2003 the record-setting high-altitude, solar powered, unmanned Helios aircraft crashed due to a dynamic aeroelastic instability and the subsequent NASA report blamed the failure in part on lack of adequate analysis methods (Noll et al. (2004)). However, in the case of conventional aircraft, the science of aeroelasticity is actually considered matured and the popularity of air travel proves industry's ability to build safe airplanes that meet our basic requirements.

It may be just as obvious, that this is not enough to be successful in a competitive market, because new aircraft must always be significantly better than existing designs to justify the immense development costs. In this context, better or best refers to a compromise of often conflicting objectives such as operating cost, speed, capacity, safety, complexity, etc. Not only the design is expected to improve, but also the design process: Resources such as manpower, time and computational capabilities

are limited, which challenges aeroelastic analysis to provide quick and accurate predictions on a budget. Inefficiencies in analysis mean that fewer alternative designs may be considered, which indirectly affects the quality of the final design. On the other hand, using simpler, faster, but less accurate models is also problematic: Any inaccuracies in the prediction of instability may necessitate larger safety factors, possibly leading to bulkier and heavier designs. The importance of efficient analysis becomes particularly apparent if numerical methods for design optimization and reliability analysis are used to systematically search for better designs and to predict design failures.

1.2 Numerical Optimization

For the purpose of numerical optimization, a design is parametrized as a set of variables. The variable ranges constitute the design space which may contain regions deemed infeasible due to constraints of manufacturability, material stress limits, etc. The prospect of numerical optimization is to find the feasible design that minimizes a given objective function, which is dictated by goals of the designer, such as minimum weight. This optimization process generally requires the evaluation of numerous samples, selected by the algorithm, to iteratively locate the optimal design. Typically, the most efficient algorithms consider the gradient of objective and constraint functions with respect to the design parameters to determine promising additional samples. Gradient-free formulations such as genetic algorithms are available as well, but they usually require much larger numbers of samples to converge to an optimal design.

However, in the case of wing design, even a single design evaluation necessitates the simulation of thousands of relevant flight scenarios to confirm overall aeroelastic stability (Bhatia (2003)). The considerable computational cost of each of these complex simulations may easily create a bottle-neck that renders the whole process of numerical optimization infeasible. The large cost of design evaluations is a common obstacle to numerical optimization in many fields of engineering and has

received much attention from academia. Two powerful "work-arounds" are the use of surrogate models and multi-fidelity analysis methods.

A surrogate model estimates model response values based on evaluated training samples. That is, a surrogate model is able to predict the output of a simulation model for a range of design parameters, based on previously simulated samples. For example, a very basic surrogate model may use linear interpolation to predict the model response in between evaluated training samples. In numerical optimization the expectation is that relatively few, carefully selected case studies are sufficient to obtain a surrogate for expensive simulation models. The optimization algorithm will then search the surrogate for the optimum design, which is an approximate optimal design with respect to the underlying simulation model. Surrogate models are often very sophisticated to use as few training samples as possible and they may be updated during the optimization process to refine the accuracy of their predictions locally. The widespread use of surrogate models in optimization is due to the demonstrated ability to reduce overall simulation times to a fraction on a wide range of design problems. However, surrogate models are based on the assumption that the approximated model represents a continuous, if not smooth, function. Therefore, they are not suited for aeroelastic stability constraints with binary response values (stable or unstable) or bifurcations, where a small change in parameters alters the system behavior qualitatively, leading to discontinuities in the responses.

Like the use of surrogates, multi-fidelity methods are intended to reduce the computational burden of simulations during numerical optimization. The premise of this approach is that it is often unnecessary to use the highest-fidelity simulations available in the earlier stages of the design process. Most simulation models have straight forward fidelity parameters, often related to discretization, such as mesh size. In addition, the underlying assumptions of a model will affect its fidelity: An aerodynamic model that neglects viscous effects, for example, has lower fidelity than a more realistic model that takes these effects into account. Higher fidelity models require larger computational resources and a careful selection of the proper level of fidelity might substantially decrease the computational burden. Further, it

is customary to use lower-fidelity models for preliminary study of the design space and higher-fidelity models for refinement where necessary. Multi-fidelity methods formalize these practices to employ them automatically in numerical design optimization.

Such research on multi-fidelity methods is more recent than on surrogates, but considerable progress has already been made in the last 25 years. Several algorithms have demonstrated significant improvements on the efficiency of numerical optimization, often reducing run-time to a fraction, without sacrificing the accuracy of the final result. Unfortunately these methods are generally based on the assumption that the model responses constitute a continuous, if not smooth, function of the design parameters. Just like surrogate models, the existing multi-fidelity approaches are not suitable for the case of aeroelastic stability constraints with binary or discontinuous simulation outputs.

1.3 Scope

Aeroelastic stability constraints present a difficult obstacle to numerical optimization as they represent a class of constraint characterized by high cost of evaluating the corresponding simulation models and binary or discontinuous nature of responses. Because of the high cost of each evaluation, straight-forward numerical design methods such as genetic programming, pattern search and Monte-Carlo sampling are not feasible. On the other hand, more efficient algorithms are severely hampered by non-smooth responses. Likewise, drastic improvements of efficiency in optimization due to surrogate models and multi-fidelity methods are not transferable as they are limited to continuous response models, which are admittedly more common in engineering.

As opposed to the use of meta-models, which seek to approximate the model responses via a continuous surrogate function, this dissertation proposes a classification-based method to generalize the results of simulations based on their classification as feasible or infeasible. The advantages of this approach include its

insensitivity to binary or discontinuous responses and the possibility of incorporating various different models into a single predictor of design feasibility. In the case of multiple constraint models one may evaluate each model sequentially for each case study and the evaluation may be stopped as soon as one model classifies the design as infeasible, thus reducing the evaluation cost of infeasible designs.

While previous work has presented algorithms for the selection of simulation cases in order to build and refine such predictors via the machine learning method of support vector machines (SVM), the current work focuses specifically on the fidelity of the simulations. Specifically, a case study may often be evaluated at different levels of fidelity, where higher fidelity models generally produce more accurate results at the price of higher computational cost. On the other hand, lower-fidelity models may provide large savings, while correctly classifying many case studies as feasible or infeasible.

To explore the possible advantage of incorporating lower-fidelity results, this dissertation develops an algorithm for selection of both case studies and corresponding fidelity levels in order to build and iteratively refine prediction models of design feasibility based on SVM. The resulting smooth, analytical predictor function, whose zero contour approximates the boundary of the feasible design parameter space, is well suited for gradient-based optimization algorithms. In addition, evaluating the predictor is very efficient computationally, enabling propagation of uncertainties, for example via Monte-Carlo sampling. The accuracy of the SVM predictor is dependent on the number and distribution of evaluated designs (training samples) and it has been shown that higher accuracy is obtained if samples are concentrated in the vicinity of the actual boundary of the feasible space. Towards this end, an adaptive sampling method was developed to iteratively improve the SVM via additional training samples, carefully selected with respect to the current SVM boundary (Basudhar and Missoum (2010)). However, the previous algorithm did not consider the availability of multiple levels of simulation fidelity, that is each sample was evaluated via the same high-fidelity model.

This dissertation addresses this limitation by proposing a multi-fidelity algorithm

that incorporates a lower-fidelity simulation model. The motivation of this effort is derived from the observation that many designs are either clearly feasible or clearly infeasible and will be classified as such even by a low-fidelity model. Since the classification is the only information necessary to train the SVM, the careful use of lower-fidelity analysis models promises to improve the overall efficiency of approximating the failure boundary considerably. To investigate this assumption an adaptive sampling algorithm is developed that not only selects the SVM training samples, but also determines the appropriate level of fidelity for each sample. This could be a straight-forward task if it was known a priori which regions of the design space are classified correctly by low-fidelity analysis. However, such assumptions would likely limit the algorithm to few special applications and are therefore avoided. Instead, it is only assumed that samples close to the actual boundary of the feasible space will need to be evaluated by the higher fidelity model to ensure valid results.

By default, the algorithm aims to achieve accurate predictions over the whole design space, but an option exists to focus sampling on regions of interest based on an objective function. This yields an algorithm for numerical design optimization where accurate predictions of feasibility are primarily needed to locate the constrained optimal design. The details of the multi-fidelity algorithm, that offers the efficient use of low-fidelity analysis while converging to the constraint boundary implicitly defined by the high-fidelity model, are described in Chapter 3.

The dissertation is organized as follows: Chapter 2 provides the background knowledge on current surrogate models and multi-fidelity methods used for numerical optimization. In addition an introduction to the theory of aeroelasticity is provided, including a detailed derivation of aeroelastic models later used as example applications. Another section is dedicated to support vector machines, summarizing their general use as a classifier and recent research on explicit design space decomposition. Chapter 3 presents in detail the core contribution of this research, which is the multi-fidelity algorithm for the iterative construction of the constraint boundary as an SVM. All aspects ranging from the selection of SVM parameters

to the different kinds of adaptive samples and the update of the current boundary approximation at each iteration are explained in depth. Chapter 4 shows the application of the algorithm to establish stability boundaries for two aeroelastic stability models, the first of which simulates a rigid two degree of freedom airfoil supported by nonlinear springs, capable of reproducing several failure modes such as flutter, static divergence and limit cycle oscillation. The second model uses a commercial software package to assess the aeroelastic stability of a flexible cantilevered wing via modal flutter analysis. Chapter 5 demonstrates the variant of the algorithm geared towards numerical optimization to determine the constrained optimal design for several test problems as well as the stable cantilevered wing configuration with minimum weight.

CHAPTER 2

BACKGROUND AND LITERATURE REVIEW

2.1 Surrogate Models

The focus of this section is on surrogate models used in simulation aided design analysis where engineers need to know the effect of design parameters on product performance to find better designs and to predict performance under variation or uncertainty in the parameters. Most general optimization and uncertainty quantification algorithms require large numbers of design evaluations, but in practice the number of simulations is limited by computational resources. Surrogate models are therefore employed to predict simulation results based on few, carefully selected, simulated samples. Formally, "surrogate modeling can be seen as a non-linear inverse problem for which one aims to determine a continuous function y of a set of design variables $\boldsymbol{x}_i$ from a limited amount of available data y_i" (Queipo et al. (2005)). Linear interpolation, for example, is a simple form of surrogate model. In general the application of surrogates starts with a set of evaluated samples $\boldsymbol{x}_i$, which may be selected based on the criteria discussed in Section 2.1.2. As the next step a surrogate model (Sections 2.1.3, 2.1.4, 2.1.5, 2.1.6) is selected and fitted to the simulation results y_i. Additional training samples may be selected iteratively to refine the surrogate model in regions of interest (Section 2.1.5). It is of course critical to know how accurate the predictions of the surrogate model are and Section 2.1.1 introduces various methods to estimate prediction error.

2.1.1 Generalization error

In general the surrogate model will not match the underlying simulation model perfectly and this section reviews various methods to quantify the accuracy of the surrogate. Since the focus of this dissertation is on deterministic simulation models,

this section is geared towards, but not limited to surrogate models that interpolate the results of evaluated samples. While a Kriging model, for example, is guaranteed to match the actual model at the training samples $\boldsymbol{x}_i$ perfectly, its predictions over the rest of the design space are an approximation of the actual model. Methods to predict the generalization error away from the training samples are very useful to judge if a surrogate is sufficiently accurate for engineering purposes such as design optimization or probability of failure assessment.

Some models, such as Kriging, provide a measure of the accuracy of their predictions, based on statistical analysis of the training samples. Specifically, the Kriging model estimates the variance of the actual function value with respect to the Kriging prediction. In the general case the following methods may be used to approximate the generalization error of any surrogate (Queipo et al. (2005)).

Error Measures

Global error measures quantify the average deviation of surrogate predictions $\hat{y}(\boldsymbol{x})$ from the actual function values $y(\boldsymbol{x})$. A global error measure is generally defined by integrals of a loss function L over the design space S:

$$\text{error} = \frac{\int_S L(\hat{y}(\boldsymbol{x}), y(\boldsymbol{x}))\,\mathrm{d}\boldsymbol{x}}{\int_S \mathrm{d}\boldsymbol{x}} \tag{2.1}$$

where the loss function measures the local deviation of the surrogate model from the actual function value and the integral provides an average over the design space. In practice the integral of Equation 2.1 is approximated via a finite set of N_s samples:

$$\text{error} \approx \frac{1}{N_s} \sum_{i=1}^{N_s} L(\hat{y}(\boldsymbol{x}_i), y(\boldsymbol{x}_i)) \tag{2.2}$$

Various loss functions are used to compare the surrogate outputs $\hat{y}(\boldsymbol{x})$ to the actual model outputs $y(\boldsymbol{x})$ in order to quantify the accuracy of the surrogate. The most popular loss functions are:

- Quadratic: $L(f_1, f_2) = (f_1 - f_2)^2$
- Laplace: $L(f_1, f_2) = |f_1 - f_2|$

- ϵ-insensitive: $L(f_1, f_2) = \begin{cases} 0 & \text{if } |f_1 - f_2| < \epsilon \\ |f_1 - f_2| - \epsilon & \text{otherwise} \end{cases}$
- Huber: $L(f_1, f_2) = \begin{cases} 0.5\,(f_1 - f_2)^2 & \text{if } |f_1 - f_2| < \epsilon \\ \epsilon(|f_1 - f_2| - \epsilon/2) & \text{otherwise} \end{cases}$
- log cosh: $L(f_1, f_2) = \log\cosh(f_1 - f_2)$

The quadratic loss function yields the mean square error (MSE), an often used global error measure in the numerical design community. Another popular error measure, called the coefficient of determination R^2:

$$R^2 = 1 - \frac{\sum_{i=1}^{N_s}(y(\boldsymbol{x}_i) - \hat{y}(\boldsymbol{x}_i))^2}{\sum_{i=1}^{N_s}(y(\boldsymbol{x}_i) - \bar{y})^2} \tag{2.3}$$

is also based on the quadratic loss function. Here $\bar{y}(\boldsymbol{x})$ denotes the mean actual function value of all evaluated samples and the maximum value of $R^2 = 1$ corresponds to a perfect surrogate. In general the quadratic loss function is often preferred over the Laplace loss function because it is differentiable, but is sometimes criticized for over-emphasizing outliers. The ϵ-insensitive loss function only penalizes deviation greater than a threshold ϵ and plays a major role in support vector regression (Section 2.1.6). The Huber loss function (Huber (1964)) combines the advantages of Laplace and quadratic loss functions: It is once differentiable and less sensitive to outliers due to its linear extension. The log cosh function behaves similar to the Huber function but is infinitely differentiable.

Though a surrogate model may have a low global error measure, there may be points in the design space where the deviation is unacceptably high. This may be discovered by considering local error measures that quantify the maximum error in the predictions of the surrogate model. For example the maximum absolute error (MAE) is defined as the maximum of the Laplace loss function over the design space:

$$\text{MAE} = \max_{\boldsymbol{x}} |\hat{y}(\boldsymbol{x}) - y(\boldsymbol{x})| \quad \text{with } \boldsymbol{x} \in S \tag{2.4}$$

In practice it is approximated based on a finite number of evaluated samples and often divided by the standard deviation of the actual function values to estimate

the relative absolute error RMAE:

$$\text{RMAE} = \frac{\max_i |\hat{y}(\boldsymbol{x_i}) - y(\boldsymbol{x_i})}{\sigma_y} \tag{2.5}$$

Validation Set

After the surrogate has been obtained from the training samples, the most straightforward approach to approximate the generalization error is by evaluating another set of samples (validation set) and comparing their actual function values to the predicted values of the approximation. A brief history and analysis of this method is provided by Stone (1974). The obvious drawback of this method is the expense of evaluating the test set, which may have to be large if a small error is to be detected. However the error measure obtained from a separate validation set is unbiased and the method is practical if the cost of evaluating samples is small.

Cross-Validation

Cross-validation is a method to approximate the generalization error of a surrogate model without the evaluation of additional samples. This cross-validation error is frequently used as a merit function to inform the selection of surrogate model parameters. Given a surrogate model $\hat{y}(\boldsymbol{x})$ based on N_s evaluated training samples $\boldsymbol{x}_i$ with actual function values y_i, the cross-validation estimate of the generalization error ϵ_{cv} of $\hat{y}(\boldsymbol{x})$ is calculated via the following steps:

First the training samples are divided into k sets (folds) of approximately equal size. k additional surrogate models $\hat{y}_k(\boldsymbol{x})$ are constructed in the same way as $\hat{y}(\boldsymbol{x})$, each using all training samples, except the kth fold. Now each of the N_s samples $\boldsymbol{x}_i$ is evaluated by the surrogate model $\hat{y}_k(\boldsymbol{x})$ that was trained without said sample providing prediction $\hat{y}_i$. Finally the cross-validation estimate of the generalization error is obtained by comparison of these predictions to the actual function values y_i:

$$\epsilon_{cv} = \frac{1}{N_s} \sum_{i=1}^{N_s} L(y_i, \hat{y}_i) \tag{2.6}$$

If the quadratic loss function is used, ϵ_{cv} is an estimate of the mean squared error of the surrogate obtained from using all training samples. It is almost unbiased if the number of folds equals the number of training samples (leave-one-out cross-validation (LOO-CV)).

In general, using LOO-CV has the disadvantage that as many models as samples have to be trained. However in the case of polynomial regression and Kriging, analytical expressions for the leave-one-out cross-validation error are available that avoid the construction of n surrogates (Myers and Montgomery (1995); Martin and Simpson (2005)). In has also been reported that using only 5-10 folds already gives a very good approximation of the LOO-CV error (Friedman et al. (2001)). Cross-validation and its variants are discussed in more detail by Lachenbruch and Mickey (1968) with a focus on classification problems and in a wider context by Stone (1974).

Bootstrapping

Bootstrapping is another method to approximate the generalization error of a surrogate model and is closely related to cross-validation. Its most distinct advantage is likely the ability of estimate confidence intervals on the outputs of the surrogate model (Hall (1986); Carpenter and Bithell (2000)). Like cross-validation, bootstrapping consists of repeatedly removing a number of training samples for validation, but samples are selected randomly with replacement. For example if there are 100 training samples then 15 samples may be removed at each round for validation and the results of all rounds will be averaged to approximate the generalization error. To ensure convergence of the error measure a large number of rounds may be required. A comparison on a number of test problems has shown bootstrapping to be slightly superior to cross-validation (Efron (1983)) in terms of estimating the generalization error, but for many applications the difference will be negligible.

The confidence interval obtained via bootstrapping quantifies the confidence in the predictions of the surrogate model. For example if a surrogate model predicts a certain value $\hat{y}_i$, the 95% confidence interval γ makes a probabilistic statement

about the true value y_i:

$$P(-\gamma \leq y_i - \hat{y}_i \leq \gamma) = 95\% \tag{2.7}$$

In other words the true function value y_i has a 95% chance of being within γ of the predicted value $\hat{y}_i$. An in-depth introduction to bootstrapping in general is provided by Efron and Tibshirani (1993) and Carpenter and Bithell (2000) is a recent review of the various methods to estimate confidence intervals via bootstrapping.

2.1.2 Sample Selection, Design of Experiments

In the case of computer simulations the engineer is generally free to choose the set of training samples to build the initial surrogate model, which may be refined by adaptive sampling. While Chapter 3 discusses in great detail the adaptive selection of samples for the construction of SVM, the current section introduces several concepts for the selection of initial samples. A much more in-depth presentation is provided for example by Myers et al. (2009); Box and Draper (1987); Koehler and Owen (1996) and concise summaries are given in Simpson et al. (2001); Queipo et al. (2005).

The goal of experimental design is to select a set of samples, often referred to as design of experiments (DOE), that is the best compromise between the cost of evaluating samples and the need for a sufficiently accurate surrogate model. The DOE may be represented by a matrix, where each row contains a set of simulation parameters. Columns correspond to design variables (factors) and the variable values are referred to as levels.

Assessment

Based on the assumptions on the function to approximate and the model to be used, one may compare DOEs with respect to certain criteria or measures of merit. As a simple example in the case of deterministic simulations, repeated samples are clearly a waste of resources. Popular measures of merit are bias and variance which both assume that the outputs of the actual function $y(\boldsymbol{x})$ follow a probability

distribution (Queipo et al. (2005)). Bias quantifies the extent to which the surrogate model outputs ($\hat{y}(\boldsymbol{x})$) differ from the true values ($y(\boldsymbol{x})$) calculated as an average over all possible data sets. Each data set consists of a random sample of the model outputs. Bias is equivalent to the expected generalization error (Equation 2.1). A one-dimensional example may clarify this measure: Assume a function $f(x)$ is sampled n times at x_1, x_2 and x_3. The two sets of n function values at x_1 and x_2, that is y_{1i} y_{2i} are used to build n surrogate models $\hat{y}_i(x)$. The bias at x_3 is then approximated by the mean difference between measured and predicted values:

$$\text{bias}(x_3) \approx \frac{1}{n}\sum^{n} \hat{y}_i(x_3) - y_{3i} \tag{2.8}$$

The variance is simply the variance of the predicted values about their mean $\hat{\mu}$:

$$\hat{\mu}(x_3) \approx \frac{1}{n}\sum^{n} \hat{y}_i(x_3) \tag{2.9}$$

$$\text{var}(x_3) \approx \frac{1}{n}\sum^{n} \left(\hat{y}_i(x_3) - \hat{\mu}(x_3)\right)^2 \tag{2.10}$$

Under rather restrictive conditions it may be possible to obtain DOEs that will yield minimum bias or variance, for example if a polynomial function is approximated by a polynomial regression surrogate model (Myers and Montgomery (1995)). Other measures of merit such as orthogonality, rotatability, etc. can be shown to produce optimal DOEs in certain cases, such as when the actual function is linear.

However in the case of complex nonlinear functions with unknown correlation it has been observed that these classical criteria hold little value and samples should instead be distributed uniformly over the design space (Sacks et al. (1989b,a)). Further Swiler et al. (2006) compared five methods to obtain space filling DOEs and concluded that the obtained surrogate models were all comparable in terms of accuracy. In other words the three methods for generating uniformly distributed designs of experiments discussed in the following sections can be expected to produce equally good surrogates.

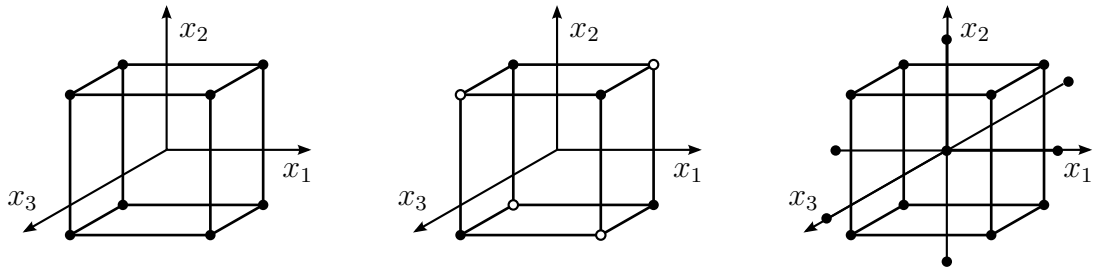

(a) full factorial (b) fractional factorial (c) central composite

Figure 2.1: Three variants of factorial designs in three-dimensional design space. Samples are denoted by solid black dots.

Factorial Designs

Full factorial designs are likely the simplest space filling designs. For each parameter a set of values is selected and the DOE consists simply of every possible combination, forming a grid spanning the design space. For example Figure 2.1a shows a full factorial design with two levels in a three-dimensional design space. Two and three levels per variable are most common and the assumption is that this provides enough information to discover linear and quadratic dependencies. The number of samples is an exponential function of the number of levels, therefore full factorial designs are generally not practical for high-dimensional problems. A possible solution is to use fractional factorial designs such as Plackett-Burman designs (Plackett and Burman (1946)) which leave out some of the samples. Figure 2.1b) shows a half-fractional design consisting of half as many samples as the corresponding full factorial design. Another variation of the factorial design is the central composite design (CCD) (Figure 2.1c), which may be considered as a compromise between 2- and 3-level full factorial designs. A thorough introduction to full and fractional factorial designs and their variations is given by Myers et al. (2009) for example.

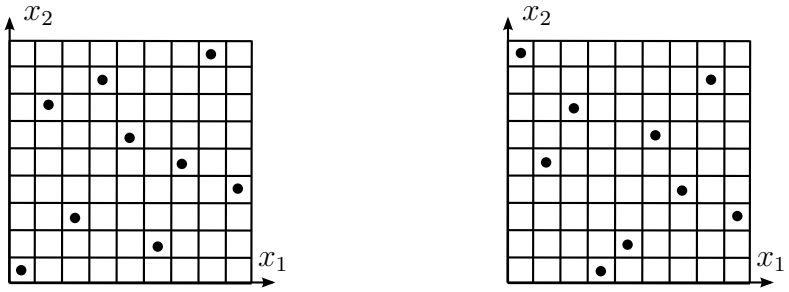

(a) LHS design 1 (b) LHS design 2

Figure 2.2: Two examples of latin hypercube sampling with 9 levels in a two-dimensional design space. In each design, none of the 9 segments is sampled twice.

Latin Hypercube Sampling (LHS)

A latin hypercube sampling (McKay et al. (1979)) is obtained by dividing each parameter range into n segments of equal probability. n samples are composed randomly such that each segment is sampled once and no two samples contain the same level for any of the factors as shown by two examples of LHS in Figure 2.2. In the case where the parameters are not random variables, n equally spaced values are selected for each parameter. Latin hypercube sampling has been used for over thirty years and this standard procedure is covered by most texts on computer experiments.

Advantages of LHS are the simplicity of the algorithm which allows to generate large DOEs very efficiently as compared to central voronoi tesselation (Section 2.1.2). Also unlike factorial designs (Section 2.1.2) any number of samples may be generated. A possible disadvantage of LHS is that it can be lacking in terms of uniformity as measured by maximum minimum-distance between samples (Queipo et al. (2005)). This has been addressed by various optimized LHS (Ye et al. (2000); Viana et al. (2010)).

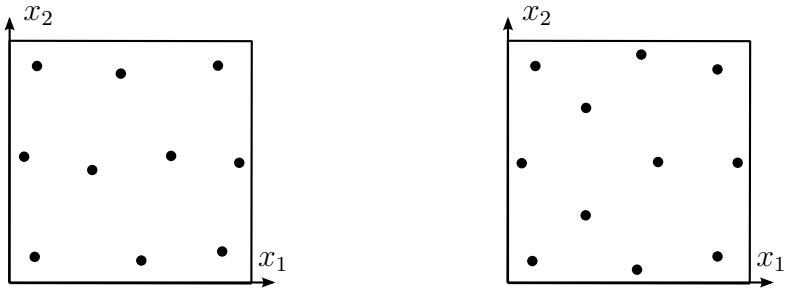

(a) CVT design: 10 samples (b) CVT design: 11 samples

Figure 2.3: Two examples of CVT design with uniformly distributed samples in a two-dimensional design space.

Central Voronoi Tessellation (CVT)

Voronoi Tessellation (Voronoi (1908)) has many applications in science and engineering, but here we are only interested in their application to obtain a DOE of uniformly distributed samples. Unlike factorial designs, CVT designs can be obtained for any number of samples, as demonstrated by the two DOEs in Figure 2.3.

In general a Voronoi tessellation is a decomposition of an n-dimensional space S into m Voronoi cells. A Voronoi cell V_i associated with location $\boldsymbol{z}_i$ is defined as:

$$V_i = \{\boldsymbol{x} \in X | d(\boldsymbol{x}, \boldsymbol{z}_i) \leq d(\boldsymbol{x}, \boldsymbol{z}_j) \text{ for all } j \neq k\} \tag{2.11}$$

where d is a distance measure such as Euclidean distance.

Of special interest are Voronoi tessellations in which the cell locations $\boldsymbol{z}_i$ coincide with their centroids $\boldsymbol{c}_i$:

$$\boldsymbol{c}_i = \frac{\int_{V_i} \boldsymbol{x}\rho(\boldsymbol{x})\,\mathrm{d}\boldsymbol{x}}{\int_{V_i} \rho(\boldsymbol{x})\,\mathrm{d}\boldsymbol{x}} \tag{2.12}$$

If a constant density function ρ is used the locations of these *central* Voronoi tessellations are uniformly distributed. In general, the problem of decomposing a given design space via a CVT with a given number of cells has multiple solutions. Various iterative algorithms have been proposed to obtain central Voronoi tessellations from an initial set of locations. Lloyd's algorithm (Lloyd (1982)) for example essentially

consists of replacing the cell locations by their closest centroid at each iteration. A concise summary of CVT and it's applications is offered by Du et al. (1999). A very comprehensive treatment is the classical text Okabe et al. (1992).

2.1.3 Polynomials

While the more powerful surrogate models of radial basis functions and Kriging discussed in later sections are relatively recent developments, polynomial functions were among the first surrogate models. These surrogate models are parameterized in terms of the polynomial coefficients, and searching for the parameters that give the closest fit to a given set of results is known as regression.

This section provides a brief summary of the fundamentals of polynomial surrogate models. Various review articles offer concise introductions (Forrester and Keane (2009); Simpson et al. (2001); Queipo et al. (2005)) and in-depth coverage is provided by many text books such as the classic Box and Draper (1987).

In the case of a single variable, a polynomial surrogate model of degree m is given as:

$$\hat{y}(x) = \sum_{i=0}^{m} \beta_i x^i \tag{2.13}$$

In the n-dimensional case the most-common polynomials of degree 1 and 2 are:

$$\hat{y}(\boldsymbol{x}) = \beta_0 + \sum_{i=1}^{n} \beta_i x_i \tag{2.14}$$

$$\hat{y}(\boldsymbol{x}) = \beta_0 + \sum_{i=1}^{n} \beta_i x_i + \sum_{i=1}^{n} \sum_{i=1}^{j} \beta_{ij} x_i x_j \tag{2.15}$$

Given a set of s samples $\boldsymbol{x}_i$ the predictions $\hat{y}_i$ may be written in matrix form as:

$$\hat{\boldsymbol{y}} = \boldsymbol{\Phi}\boldsymbol{\beta} \tag{2.16}$$

where $\boldsymbol{\beta}$ contains all the coefficients and $\hat{\boldsymbol{y}}$ is a column vector of predictions. In the

one-dimensional case $\mathbf{\Phi}$ is the Vandermonde matrix:

$$\mathbf{\Phi} = \begin{bmatrix} 1 & x_1 & x_1^2 & \dots & x_1^m \\ 1 & x_2 & x_2^2 & \dots & x_2^m \\ \vdots & \vdots & \vdots & \ddots & \vdots \\ 1 & x_s & x_s^2 & \dots & x_s^m \end{bmatrix} \tag{2.17}$$

In the n-dimensional case $\mathbf{\Phi}$ also contains mixed terms. Assuming that the number of samples s exceeds the number of coefficients, the coefficients can be determined uniquely by minimizing the quadratic prediction error:

$$\boldsymbol{\beta} = \arg\min_{\boldsymbol{\beta}} \frac{1}{s} \sum^{s} ||\hat{\boldsymbol{y}} - \boldsymbol{y}||^2 \tag{2.18}$$

The quadratic loss function is differentiable (Section 2.1.1) and the coefficients are obtained by setting the derivative of the sum of errors to zero. This results in a linear equation for $\boldsymbol{\beta}$ with the solution:

$$\boldsymbol{\beta} = \left(\mathbf{\Phi}^T \mathbf{\Phi}\right)^{-1} \boldsymbol{y} \tag{2.19}$$

The degree m of the polynomial surrogate may be selected based on minimum estimated generalization error using, for example, cross-validation 2.1.1. Alternatively one may use the null-hypothesis under which the degree is increased as long as the improvement of a scaled error measure is significant (Ralston and Rabinowitz (1978)).

In theory any continuous function is approximated to arbitrary accuracy by a Taylor series of high enough order, but in practice polynomial surrogate models are ill-suited for highly non-linear models. Since the polynomial itself is smooth, trying to approximate a discontinuous response via a polynomial surrogate via Equation 2.18 will always produce a poor fit, not necessarily limited to the discontinuity. In high dimensions only low order polynomials may be feasible due to the large number of coefficients. Additional concerns are the oscillatory shape of high degree polynomials and numerical stability.

2.1.4 Radial Basis Functions

Here a weighted sum of simple basis functions is used to approximate the function of interest based on a set of n evaluated samples $\boldsymbol{x}_i$ and corresponding function values $y_i = f(\boldsymbol{x}_i)$ (Broomhead and Lowe (1988)). The surrogate model $\hat{f}(\boldsymbol{x})$ is constructed as:

$$\hat{f}(\boldsymbol{x}) = \sum_{i=1}^{n} w_i \psi \left(\|\boldsymbol{x} - \boldsymbol{x}_i\| \right) \tag{2.20}$$

with weights w_i and radial basis function ψ. The function argument $\|\boldsymbol{x} - \boldsymbol{x}_i\|$ equals the distance to the training sample $\boldsymbol{x}_i$ as is often referred to as radius. Equation 2.20 is so general that it encompasses several popular surrogate models. For example, splines can be represented as radial basis functions if the basis function is selected properly. Similarly, single layer neural networks with radial coordinate neurons may be represented by equation 2.20 (Duch and Jankowski (1999)). Kriging models however do not conform to equation 2.20 since their basis function is not a function of euclidean distance. The basis function $\psi(r)$ may be fixed or parametric and some popular choices are (Forrester and Keane (2009)):

- linear $\psi(r) = r$
- cubic $\psi(r) = r^3$
- thin plate spline $\psi(r) = r^2 \ln(r)$
- Gaussian $\psi(r) = e^{-r^2/2\sigma^2}$
- multi-quadratic $\psi(r) = (r^2 + \sigma)^{1/2}$
- inverse multi-quadratic $\psi(r) = (r^2 + \sigma)^{-1/2}$

In general parametric kernels may lead to better approximations with fewer samples if the parameters are chosen wisely. However estimation of the parameters such as σ, based on for example cross-validation (Friedman et al. (2001)), will add considerable over-head and therefore fixed basis functions may be a better choice.

For a given basis function the weights $\boldsymbol{w}$ are obtained by solving the interpolation condition 2.21 which can also be stated in matrix form 2.22:

$$\hat{f}(\boldsymbol{x}) = \sum_{i=1}^{n} w_i \psi \left(||\boldsymbol{x} - \boldsymbol{x}_i|| \right) = y_i) \tag{2.21}$$

$$\boldsymbol{\Psi w} = \boldsymbol{y} \tag{2.22}$$

Often the number of basis function is chosen to match the number of evaluated samples and then the interpolation condition is easily solved for $\boldsymbol{w}$. In the case of Gaussian and inverse multi-quadratic basis functions $\boldsymbol{\Psi}$ will be symmetric positive-definite enabling computation of $\boldsymbol{w}$ via Cholesky factorization (Vapnik (1998)). Further, in the case of Gaussian kernels the mean squared error of the prediction is approximated as

$$MSE(\boldsymbol{x}) = \sqrt{1 - \boldsymbol{\psi}(\boldsymbol{x})^T \boldsymbol{\Psi}^{-1} \boldsymbol{\psi}(\boldsymbol{x})} \tag{2.23}$$

as derived in detail in Sóbester (2003); Gibbs (1997).

If the evaluated samples are known to contain "noise", then an exact interpolation is known as overfitting and results in poor generalization of the model. To avoid overfitting, only a small number of basis function may be selected via support vector regression (Section 2.1.6). Alternatively a regularization parameter λ may be introduced (Keane and Nair (2005)):

$$(\boldsymbol{\Psi} + \lambda \boldsymbol{I})\boldsymbol{w} = \boldsymbol{y} \tag{2.24}$$

With the resulting weights of the RBF function given by the least-squares solution of the above equation. If it is known, λ should be set to the standard deviation of the noise (Keane and Nair (2005)).

2.1.5 Kriging

The concept of Kriging was introduced by Danie G. Krige to model geospacial distributions with the goal of selecting the most promising locations for mining (Krige (1951)). A detailed history of the origins of Kriging is given by Cressie (1990). Kriging was first proposed as a surrogate model of deterministic simulations by Sacks

et al. (1989b) and is now widely used for this purpose (Kleijnen (2009)). The popularity of Kriging is founded in part in the generality of the approach as the only assumption about the approximated function is its continuity. On the other hand the large number of parameters to be estimated create considerable overhead and Kriging is therefore best suited to replace relatively expensive simulations. For the same reason it is rarely used for problems with more than 20 variables (Forrester and Keane (2009)). The availability of the estimated prediction error is very helpful to select additional samples to refine the model. The model parameters, estimated based on statistical analysis of the training data, may provide valuable information about the actual function, especially for high-dimensional problems where the response values are not easily visualized. For example, parameter θ_k can be used to identify the most important variables (Keane (2003)) and exponent p_k characterizes the smoothness of the response (see Equation 2.30).

Concept

The basic assumption in Kriging is that the unknown function $y(\boldsymbol{x})$ can be approximated by the sum of global trend $f(\boldsymbol{x})$ and local deviation $Z(\boldsymbol{x})$.

$$y(\boldsymbol{x}) \approx f(\boldsymbol{x}) + Z(\boldsymbol{x}) \tag{2.25}$$

$f(x)$ known polynomial (global function), often constant (Sacks et al. (1989b); Welch et al. (1990, 1992)). Working with $f(\boldsymbol{x})$ equal to the mean value μ may be referred to as ordinary Kriging and instead using some known function is referred to as universal Kriging (Cressie (1993)). The Gaussian process $Z(x)$ is characterized by its variance σ^2, and non-zero covariance, defined in the following paragraphs.

Variance, often denoted as σ^2, is a measure of the variation in the values of the random variable X and is defined as the expected value of squared deviation from the expected value of X ($E[X]$).

$$Var(X) = \sigma^2 = E[(X - E[X])^2] \tag{2.26}$$

It is of course closely related to another common measure of variation called standard deviation σ (also called root mean square deviation).

Covariance is a measure of the dependence between two random variables (X and Y):

$$Cov(X,Y) = E[(X - E[X])(Y - E[Y])] \tag{2.27}$$

For example, $Cov(X,Y) > 0$ signifies that X is more likely to be above average if Y is above average, while $Cov(X,Y) < 0$ suggests an inverse relationship. However, covariance detects only linear dependence and one cannot conclude that two variables are independent based on their covariance.

While closely related, correlation is a better measure of the strength of the linear dependence since it is scaled by the product of standard deviations:

$$Corr(X,Y) = Cov(X,Y)/(\sigma_X \sigma_Y) \tag{2.28}$$

The value of correlation ranges from -1 to 1, where $|Corr(X,Y)| = 1$ signifies a perfectly linear relationship between the two variables.

Model Construction

Based on training samples $\boldsymbol{x}_i$ the correlation $\boldsymbol{R}$ matrix of the Gaussian process Z is defined as:

$$R_{ij} = Corr(Z(\boldsymbol{x}_i), Z(\boldsymbol{x}_j)) = \frac{1}{\sigma^2} Cov(Z(\boldsymbol{x}_i), Z(\boldsymbol{x}_j)) \tag{2.29}$$

The correlation function R_{ij} is generally not known and therefore assumed to be of the form:

$$R_{ij} = \exp\left(-\sum_{k=1}^{d} \theta_k |x_{ik} - x_{jk}|^{p_k} \right) \tag{2.30}$$

where d is the dimensionality of the design space. This continuous function equals 1 for $\boldsymbol{x}_i = \boldsymbol{x}_j$ and approaches 0 as distance $\|\boldsymbol{x}_i - \boldsymbol{x}_j\|$ approaches infinity. For large values of θ function values change rapidly even over small distances. Exponents p_k close to 2 characterize a smooth function, while p_k close to zero point to rough, nondifferentiable functions. (Jones (2001))

The parameters μ, σ, θ_k and p_k are selected to maximize the likelihood 2.31 of the observed data. Given a set of n evaluated samples $\boldsymbol{x}_i$ and corresponding function

values y_i, then the log of the likelihood $\mathcal{L}$ of this outcome (without constant terms) is:

$$\log(\mathcal{L}) = -\frac{n}{2}\log(\sigma^2) - \frac{1}{2}\log(|\boldsymbol{R}|) - \frac{(\boldsymbol{y} - \mathbf{1}\mu)'\boldsymbol{R}^{-1}(\boldsymbol{y} - \mathbf{1}\mu)}{2\sigma^2} \tag{2.31}$$

A more in-depth presentation is given in Jones (2001). It is also common to use simpler correlation modes where for example p_k is fixed to 2 or only a single θ is used on all dimensions (Sacks et al. (1989b,a); Koehler and Owen (1996)). The boundaries between radial basis functions and Kriging are therefore fluid and Kriging is sometimes considered a variation of radial basis functions.

Once the estimates for μ, σ, θ_k and p_k are obtained they can be used to estimate the likelihood of any outcome at any additional sample $\boldsymbol{x}^*$. This yields not only the expected value of $y(\boldsymbol{x}^*)$, but also its estimated probability density function. Both the expected value y^* and its mean square error (variance) are efficiently calculated in closed form (Jones (2001)). One must be careful that the prediction error σ^2 is only an estimate based on estimated parameters and the whole process is based on the assumption that the dependence between two samples is given by Equation 2.30. So clearly, the estimated prediction error is not a reliable measure, but maybe helpful for example to select additional samples. In particular, the estimated prediction error plays an important role in the efficient global optimization (EGO) algorithm presented in the following section.

Efficient Global Optimization (EGO)

This section offers a brief introduction to the efficient global optimization algorithm which is closely tied to the Kriging approach. In the case of design optimization the goal is to find the sample $\boldsymbol{x}^*$ with the lowest function value y^*. Maybe the most straight forward method is to use a sufficiently large number of samples to build the surrogate model such that the generalization error (Section 2.1.1)is negligible for the application. The surrogate is then used to find the location of the lowest predicted function value, which may be evaluated to obtain the actual lowest function value

y^*. This is a very simple and robust algorithm, but due to the cost of evaluations, it may be intractable. Fortunately lots of research effort has been directed at locating the optimum design with much fewer sample evaluations.

A function may have several local optima, and surrogate-based optimization algorithms may be divided into local algorithms that seek a local optimum in the neighborhood of an initial design and global algorithms, developed to locate the overall (global) optimum. Further one may distinguish between methods that can take into account various design constraints and other algorithms specializing in unconstrained problems. Another distinction is between algorithms geared towards deterministic models versus random models. In general, global algorithms will evaluate an initial set of samples to obtain some initial knowledge about the function behavior. During a second phase additional samples are selected iteratively to further explore regions of interest. This is often referred to as adaptive sampling or adaptive updating. The additional samples may be called infill points which are selected based on infill criteria. A broad overview of recent progress in deterministic global optimization is provided by Floudas and Gounaris (2009). A review of surrogate based infill criteria is presented by Forrester and Keane (2009). Not so recent, but not at all outdated, Jones (2001) gives an excellent summary with particular focus on the failure modes of various Kriging-based methods for unconstrained global optimization. Most recently Parr et al. (2012) gives a good summary of the latest research regarding infill criteria.

This section only discusses in detail one global unconstrained optimization algorithm based on Kriging surrogates and the maximum expected improvement criterion often referred to as efficient global optimization (Jones et al. (1998)). The presentation loosely follows Forrester and Keane (2009); Jones (2001).

Concept Initially a Kriging model is build from a relatively small set of evaluated samples. At each subsequent iteration another sample is selected at maximum expected improvement to update the Kriging model. The expected improvement infill criterion may be calculated for any point in the design space based on the predicted

value and estimated prediction error of the Kriging model as detailed in the following paragraph. Various global optimization algorithms such as genetic programming may be used to find the infill point with maximum expected improvement. Due to the low cost of evaluating the criterion the choice of algorithm is not critical and is not treated in this section.

Expected Improvement is estimated based on the assumption that the true function value at any point follows a normal distribution with variance s and mean $\hat{y}(\boldsymbol{x})$:

$$P(-\infty < \frac{y(\boldsymbol{x}) - \hat{y}(\boldsymbol{x})}{s(\boldsymbol{x})} \leq u) = \Phi(u) = \frac{1}{\sqrt{2\pi}} \int_{-\infty}^{u} \exp\left(\frac{-t^2}{2}\right) \mathrm{d}t \tag{2.32}$$

Where $\Phi(u)$ is the standard normal cumulative distribution function. If n samples $\boldsymbol{x}_i$ have been evaluated and the best (lowest) function value is y_{min} then the estimated probability that the actual function value at $\boldsymbol{x}$ will be lower is given by:

$$P(y(\boldsymbol{x}) \leq y_{min}) = \Phi\left(\frac{y_{min} - \hat{y}(\boldsymbol{x})}{s(\boldsymbol{x})}\right) \tag{2.33}$$

The improvement over the current best sample is defined as:

$$I = \begin{cases} y_{min} - y(\boldsymbol{x}) & \text{if } y(\boldsymbol{x}) < y_{min} \\ 0 & \text{otherwise} \end{cases} \tag{2.34}$$

The probability density function of improvement is a normal probability density function:

$$\frac{1}{\sqrt{2\pi}s(\boldsymbol{x})} \exp\left(-\frac{(y_{min} - I - \hat{y}(\boldsymbol{x}))^2}{2s^2(\boldsymbol{x})}\right) \tag{2.35}$$

and finally the inspected improvement is obtained by integration:

$$E(I) = \int_{I=0}^{I=\infty} \frac{1}{\sqrt{2\pi}s(\boldsymbol{x})} \exp\left(-\frac{(y_{min} - I - \hat{y}(\boldsymbol{x}))^2}{2s^2(\boldsymbol{x})}\right) \mathrm{d}I \tag{2.36}$$

The choice of convergence criterion to decide when to terminate the sampling process is always subjective and application dependent. A natural choice seems to stop the algorithm when the expected improvement is below a certain threshold. The threshold should be selected rather conservatively since the expected improvement is only an estimate. In particular Cressie (1993) shows that the prediction error

tends to be underestimated, which leads to unrealistically low estimates of expected improvement. In practical applications the number of iterations may be dictated by design schedules and computational resources.

The presented algorithm is considered a two-stage approach, where the first stage of each iteration consists of estimating the parameters of the Kriging model. The second stage relies on the accuracy of the estimated parameters to select an additional sample for evaluation. This reliance on possibly poor estimates creates various pitfalls and failure modes discussed in detail by Jones (2001). In particular the estimate of prediction error is prone to inaccuracy as pointed out by Den Hertog et al. (2005); Cressie (1993). Various alternative estimates of the variance based on bootstrapping are proposed by Den Hertog et al. (2005) and Kleijnen et al. (2012) shows how these may lead to better estimates of expected improvement. In most cases the pitfalls of the presented two-stage algorithm can be avoided by choosing a large enough set of initial samples. Alternatively one-stage algorithms have been proposed (Gutmann (2001); Jones (2001); Forrester and Jones (2008)) where the likelihood of a certain function value at an additional sample is evaluated based on training a new Kriging model passing through that point. In theory these one-stage algorithms may be the "silver bullet" of numerical optimization with surrogates, but they are also much more computationally intense and may only be practical for applications with extremely expensive model evaluations (Forrester and Keane (2009)).

2.1.6 Support Vector Regression

Support Vector Regression may be considered as a special case of radial basis functions, where only a subset of the evaluated samples is used to construct the surrogate. With reference to Equation 2.20 the number of bases n_b is much smaller than the number of evaluated samples n_s. Historically support vector regression originates in the theory of support vector machines (Vapnik (1995)), which are covered in detail in Section 2.4

Similar to radial basis functions the support vector regression seeks an approxi-

mation model of the following form:

$$\hat{f}(\boldsymbol{x}) = \mu + \sum_{i=1}^{n_b} w_i \psi\left(\boldsymbol{x}, \boldsymbol{x}_i^{sv}\right) \tag{2.37}$$

Here $\psi(\boldsymbol{x}, \boldsymbol{y})$ is referred to as kernel function and and the so-called support vectors $\boldsymbol{x}_j^{sv}$ are a subset of the evaluated samples $\boldsymbol{x}_i$. The weights w_i and support vectors are selected to minimize an objective function defined in terms of $\boldsymbol{w}$, penalized by constraints on the approximation error at the evaluated samples:

$$\boldsymbol{w} = \arg\min_{\boldsymbol{w}} \frac{1}{2}\|\boldsymbol{w}\|^2 + C \sum_{i=1}^{n_s} L(\hat{f}(\boldsymbol{x}_i), y_i) \tag{2.38}$$

Here $C > 0$ is the penalty factor and L is the ϵ-insensitive loss function introduced in Section 2.1.1:

$$L(f_1, f_2) = \begin{cases} 0 & \text{if } |f_1 - f_2| < \epsilon \\ |f_1 - f_2| - \epsilon & \text{otherwise} \end{cases} \tag{2.39}$$

and support vectors are characterized by $w_i \neq 0$. The cost function only penalizes deviations larger than ϵ and minimizing $\|\boldsymbol{w}\|^2$ may be seen as a way of minimizing model complexity (Forrester and Keane (2009)). Figure 2.4 shows an example of a one-dimensional SVR surrogate model based on a number of training samples.

The parameters ϵ and C may be chosen based on prior knowledge about the noise in the response values y_i, but that is generally not available. Alternatively cross-validation can be employed to compare ϵ, C pairs in order to find the best values. The accuracy of the support vector regression is not very sensitive to the choice of parameters and a simple grid search often yields good results.

An in-depth introduction to SVR is given by Schölkopf and Smola (2001). SVR is compared to other surrogate models on 26 engineering test problems by Clarke et al. (2005) and it was found that though Kriging may result in slightly lower generalization error, SVR appears to be more robust. Other empirical studies of the performance of SVR showed very promising results as well (Gunn (1998); Vapnik et al. (1996)). Though Kriging appears to be the surrogate model of choice for

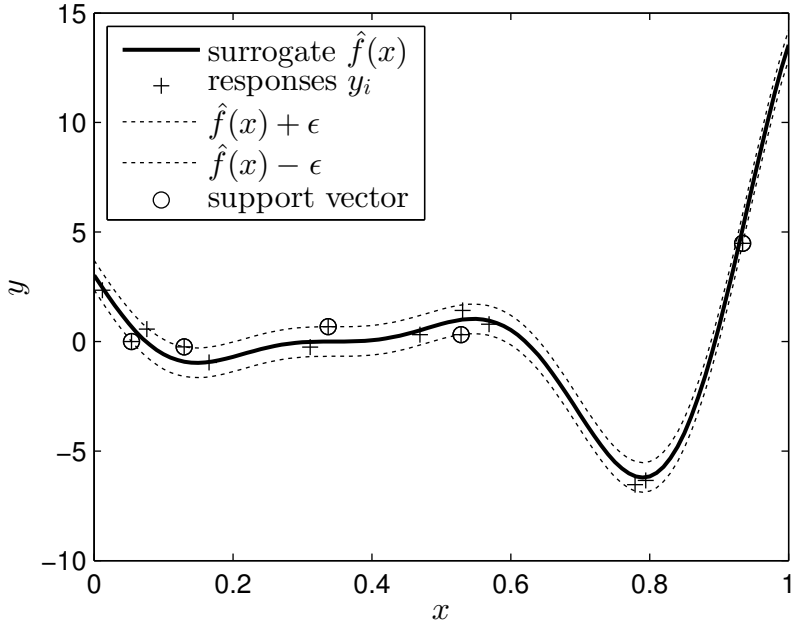

Figure 2.4: One-dimensional example of SVR surrogate model (solid) obtained from training samples, denoted by +. Only few of the samples are support vectors and the predictions of the surrogate are always within ϵ of the response values y_i

many low-dimensional applications, support vector regression is well suited for high-dimensional (> 20) problems where the application of Kriging is limited by the computational cost of parameter estimation (Forrester and Keane (2009)).

2.1.7 Ensembles of Surrogate Models

An extensive literature review (Goel et al. (2007)) concludes that there is no single most accurate surrogate model for all applications, which leaves the user with two options: Select a single surrogate model based on, for example, estimated generalization error or instead employ the weighed average prediction of an ensemble of surrogate models. The ensemble may include different kinds of models such as polynomial and Kriging or just different variants of the same model such as support vector regression models with different ϵ parameters. Estimated generalization error measures are used to determine the weight of each surrogate. Proponents of the ensemble approach argue that it acts like an insurance policy against poorly

fitted models (Viana et al. (2009)) and will improve the robustness of surrogate-based optimization (Glaz et al. (2009); Saijal et al. (2011)). On the other hand Viana et al. (2009) also concedes that while in theory the most accurate surrogate can be beaten by an ensemble, this is very difficult in practice, especially in high dimensions. Most likely the most complete and up to date review of the ensemble approach is provided by Viana (2011). In conclusion one may argue that ensembles of surrogates may become increasingly popular with the availability of more computational power and better software, when the added cost of training multiple surrogates become negligible.

2.2 Multi-Fidelity Techniques

The last 25 years have seen a major increase in publications on multi-fidelity methods for computational design. These methods use at least two models for the evaluation of designs: The high-fidelity model provides the reference in terms of accuracy and the low-fidelity model produces less accurate response values, but at significantly lower expense. In part these methods are a formalization of long-since established design practices: Engineers have always used simpler approximations for preliminary design or to rule out flagrantly inadequate designs. With the exponential increase in computational capabilities of previous decades, state of the art simulation models have become ever more sophisticated and powerful, but it is often observed that the highest accuracy available is rarely required. In addition, modern algorithms for numerical optimization and uncertainty quantification often require the evaluation of massive numbers of similar designs, which is simply not feasible at the highest level of fidelity. This situation creates the challenge of using various levels of analysis fidelity most efficiently to free up resources for cheaper and faster design processes or to investigate more alternative designs.

Section 2.2.1 discusses the benefits of building a preliminary response surface based on a low-fidelity approximation. Section 2.2.2 summarizes several algorithms to obtain a surrogate of the high-fidelity response model from a low-fidelity model

and additional high-fidelity training samples, referred to as model correction. Such modified low-fidelity models that are fitted to locally match the high-fidelity response are at the backbone of the multi-fidelity trust region optimization method reviewed in Section 2.2.3

2.2.1 Preliminary Low-Fidelity Study

Most simulation models have some straight-forward fidelity parameters which affect both accuracy and computational cost of the simulations. Examples of such parameters, which often relate to discretization, are finite element mesh size, integrator step size, number of Monte-Carlo samples, etc. When given such a model to investigate parameterized designs, it is customary to start with a relatively low fidelity setting to gain some preliminary insight into the model behavior. This is generally helpful to identify regions in the design space of particular interest and these low-fidelity results may also serve as a baseline to later determine convergence of the results with higher fidelity settings. For the purpose of design optimization the low-fidelity simulation model or a corresponding surrogate model may be used to identify "nonsense regions" which should be ignored because they are clearly far from optimal, as demonstrated on aerodynamic wing design (Giunta et al. (1995a,b)). In addition the low-fidelity response surface may be used to study the "make up" of the function, possibly identifying intervening functions that compose the model and are easier to approximate (Kaufman et al. (1996)).

2.2.2 Low-Fidelity Model Correction

Section 2.1 discusses general purpose surrogate models and it is reported that different models are better for different problems and that it is very difficult to predict which surrogate will perform best for a given response model. However, in the case of multi-fidelity models, one can use the lower-fidelity model to help in the approximation of the higher-fidelity model. It is often reasonable to assume that a surrogate model that approximates the low-fidelity model efficiently will also per-

form well on the high-fidelity model, therefore low-fidelity samples can be used to select a suitable surrogate and corresponding parameters to approximate the high-fidelity model. In other words, domain-specific information from the low-fidelity model leads to improvements in the high-fidelity model approximation.

It has been observed in the field of empirical model building that carefully constructed, special-purpose approximation models (also referred to as mechanistic models) generally outperform the general-purpose models discussed in Section 2.1 (Box and Draper (1987)). In the case of multi-fidelity analysis we have the domain-specific knowledge to build such a specialized model and several approaches have been suggested to build an approximation $\hat{f}_H(\boldsymbol{x})$ of the high-fidelity $f_H(\boldsymbol{x})$ model based on the low-fidelity model $f_L(\boldsymbol{x})$ and additional parameters $\boldsymbol{a}$ as:

$$f_H(\boldsymbol{x}) \approx \tilde{f}(f_L(\boldsymbol{x}), \boldsymbol{a}) \tag{2.40}$$

In the following paragraphs the four most popular formulations for constructing this high-fidelity surrogate will be discussed. Which of these methods is best for a given scenario is problem dependent and may be decided based on experience or approximated generalization error (Section 2.1.1). Alternatively an ensemble of surrogates may be used (Section 2.1.7).

Additive correction consists of approximating the difference in response values between the high-fidelity and the low-fidelity response values (Equation 2.41). This correction function $C(\boldsymbol{x}, \boldsymbol{a})$ may be as simple as a constant or as sophisticated as a Kriging model (Keane (2003)):

$$\hat{f}_H(\boldsymbol{x}) = C(\boldsymbol{x}, \boldsymbol{a}) + f_L(\boldsymbol{x}) \tag{2.41}$$

Additive Correction has been used successfully during a wing optimization problem by Keane (2003), but it appears that scaling as described in the following paragraph is considerably more popular.

Scaling uses a factor to match the low-fidelity model to the high-fidelity outputs:

$$\hat{f}_H(\boldsymbol{x}) = C(\boldsymbol{x}, \boldsymbol{a}) f_L(\boldsymbol{x}) \tag{2.42}$$

The approach is of course general and any surrogate maybe used to construct the correction function $C(\boldsymbol{x}, \boldsymbol{a})$, but a particularly popular approach is to use a first order Taylor series of the ratio of response values β (Alexandrov et al. (2001)):

$$\beta(\boldsymbol{x}) = \frac{f_H(\boldsymbol{x})}{f_L(\boldsymbol{x})} \tag{2.43}$$

This results in an approximation $\hat{f}_H$ that matches the high-fidelity model in value and gradient at a single point. It was first demonstrated in the Global-Local Approximation method (GLA) to match a coarse FE beam model (low fidelity) to the results of a more refined FE model (Haftka (1991)) and later employed during aerodynamic and structural optimization (Unger et al. (1992); Chang et al. (1993); Hutchison et al. (1994); Alexandrov et al. (2000, 2001); Gano et al. (2005, 2006)) using Variable Complexity Modeling (VCM) and Approximation Management Framework (AMF). Eldred et al. (2004); Eldred and Dunlavy (2006) proposed the use of second order Taylor series and compares this approach to other surrogate models. All of these methods have in common that the high-fidelity approximation $\hat{f}_H(\boldsymbol{x})$ is used as part of a gradient-based optimization routine to obtain a local optimum. For this purpose the high-fidelity approximation was repeatedly constructed to match both value and gradients of the high-fidelity model at the current iterate. A possible disadvantage of the multiplicative corrective function is the singularity if $f_L(\boldsymbol{x}) = 0$.

A more "intrusive" approach is termed parameter tuning. Here a set of parameters $\boldsymbol{a}$ of the low-fidelity model are set to fit the low-fidelity output to high-fidelity response values:

$$\hat{f}_H(\boldsymbol{x}) = f_L(\boldsymbol{x}, \boldsymbol{a}) \tag{2.44}$$

Often the low-fidelity model is specifically constructed for this purpose, for example Toropov et al. (1997) simulated a mechanical system with rigid bodies and used the mass distributions as artificial parameters to match simulation results of the same system with flexible members. Berci et al. (2011) used parameter tuning to model the gust response of a very flexible wing and Toropov and Van der Giessen (1993) approximated nonlinear deformations of a solid bar specimen. The parameter

tuning approach is most promising if the simulated system is well understood and not suitable for black-box models. If available, parameter tuning appears to be the most efficient model correction method as found in several comparative studies (Toropov et al. (1997); Berci et al. (2009, 2011)).

Space mapping is another model correction method that modifies the input of the low-fidelity model to match its outputs to the high-fidelity responses. Instead of model parameters, the design variables are transformed via a linear or nonlinear mapping function $C(\boldsymbol{x}, \boldsymbol{a})$ such that the deviation of the low-fidelity model is minimized:

$$\hat{f}_H(\boldsymbol{x}) = f_L(C(\boldsymbol{x}, \boldsymbol{a})) \tag{2.45}$$

Space mapping is often compared to drawing the contours of the low-fidelity response on a rubber sheet, which is then distorted to match the high-fidelity contours (Keane and Nair (2005)), but space mapping is of course applicable to higher dimensional design spaces as well. Space mapping is a standard tool in microwave circuit design (Bandler et al. (2004); Koziel et al. (2008)) and has been gaining popularity in other areas of design, such as structural optimization (Leary et al. (2003); Redhe and Nilsson (2006)). In general, the low-fidelity model and the high-fidelity model may have different design spaces, that is the design variables may be different in type and number. This issue was addressed via corrected space mapping proposed by Robinson et al. (2006b,a); Robinson (2007); Robinson et al. (2008) as demonstrated on wing design and flapping wing problems.

The low-fidelity model is often a surrogate fitted to low-fidelity training samples, therefore instead of applying a correction to the low-fidelity model, one may apply a correction to the low-fidelity training samples to obtain an approximation of high-fidelity response model. This was investigated by Balabanov et al. (1998) and it was found that the difference was rather small.

2.2.3 Multi-Fidelity Optimization with Trust Regions

Many researchers have focused their attention on gradient-based optimization with multi-fidelity models. Here the goal is to locate a local optimum in the vicinity of an initial guess $\boldsymbol{x}_0$, such that the objective function is minimized and any constraint functions are satisfied. In the single-fidelity case a wide array of established algorithms is available and discussed in detail in various textbooks such as Nocedal and Wright (2006); Vanderplaats (2005). In general, the first step of each iteration of gradient-based optimization consists of using the derivatives of objective and constraint functions to determine the direction in the design space in which an improvement is most likely. In the second step a line search determines the approximate local optimum along this direction, which becomes the initial guess for the next iteration. This procedure requires the evaluation of large numbers of samples, especially if finite differences are used to approximate gradients, which is often the case. In the single fidelity case, model evaluations may be replaced by calls to a surrogate model as described in Section 2.1. In the multi-fidelity case several approaches have been presented to obtain the optimum of the high-fidelity model at reduced computational cost: For example, Balabanov and Venter (2004) demonstrates using the low-fidelity model to evaluate the gradients and the high-fidelity model during the line search.

However a more robust algorithm is based on the trust region approach: Here the model correction discussed in Section 2.2.2 uses the low-fidelity model to obtain a surrogate of the high-fidelity model that matches the value and gradient at the current location $\boldsymbol{x}_i$. This surrogate is then searched by a regular single-fidelity algorithm for a predicted local optimum (minimum) $\boldsymbol{x}^*$ within a trust region of radius δ defined by $\|\boldsymbol{x} - \boldsymbol{x}_i\| < \delta$. $\boldsymbol{x}^*$ is then evaluated by the high-fidelity model to compare the improvement predicted by the surrogate to the actual improvement over $\boldsymbol{x}_i$. Only if there is an actual improvement, does $\boldsymbol{x}^*$ become the new iterate

$\boldsymbol{x}_{i+1}$, otherwise a new local optimum is obtained within a smaller trust region:

$$\boldsymbol{x}_{i+1} = \begin{cases} \boldsymbol{x}^* & \text{if } f_H(\boldsymbol{x}^*) < f_H(\boldsymbol{x}_i) \\ \boldsymbol{x}_i & \text{otherwise} \end{cases} \tag{2.46}$$

If the predicted improvement is very close to the actual improvement the trust region radius may be increased.

In summary, one may say that the line search of the single-fidelity algorithm is replaced by a broader search of a surrogate. This leads to larger improvements at each iteration and therefore the gradients of the high-fidelity model are calculated less often, which is responsible for significant reductions of run-time. The trust region update was formalized as Approximation Management Framework (AMF) (later renamed Approximation Model Management Framework (AMMF)) by Alexandrov et al. (1998) and it was proven that it converges to a local optimum. In this formulation the trust region radius is increased or reduced based on the ratio r of actual improvement over expected improvement:

$$r = \frac{f_H(\boldsymbol{x}_i) - f_H(\boldsymbol{x}^*)}{f_H(\boldsymbol{x}_i) - \hat{f}_H(\boldsymbol{x}^*)} \tag{2.47}$$

The trust region of the next iteration is determined via thresholds:

$$\delta_{i+1} = \begin{cases} c_1 \, \|\boldsymbol{x}^* - \boldsymbol{x}_i\| & \text{if } r < r_1 \\ c_2 \, \delta_i & \text{if } r > r_2 \\ \|\boldsymbol{x}^* - \boldsymbol{x}_i\| & \text{otherwise} \end{cases} \tag{2.48}$$

with $r_1 < r_2 < 1$ and $c_1 < 1$, $c_2 > 1$. The selection of the constants is somewhat arbitrary and generally not critical. Typical values are $r_1 = 0.1$, $r_2 = 0.75$, $c_1 = 0.5$ and $c_2 = 2$ (Alexandrov et al. (2001)).

Previously, similar approaches had been proposed as Global-Local Approximation (GLA) (Haftka (1991)) and Variable Complexity Modeling (VCM) (Unger et al. (1992)). The common theme of these algorithms is that the actual optimization is performed on the low-fidelity model, which is corrected to match the high-fidelity model value and slope at the current iterate.

Discussion Impressive savings of up to 80% in computational cost have been reported for optimization problems related to structural and aerodynamic design problems (Unger et al. (1992); Chang et al. (1993); Hutchison et al. (1994); Alexandrov et al. (2000, 2001); Gano et al. (2005, 2006)). Eldred et al. (2004) proposed to not only match value and slope of the high-fidelity model, but also the second derivative, and this modification compared favorably to previous methods (Eldred and Dunlavy (2006)) by allowing for larger trust regions. Usually scaling is used, but space-mapping model correction (Section 2.2.2) is compatible with the trust region approach as well, as demonstrated on wing design and flapping wing problems (Robinson et al. (2006b,a); Robinson (2007); Robinson et al. (2008)). However, it has been pointed out that these gradient-based approaches are adversely affected by numerical noise in the response values (Knill et al. (1998)).

2.3 Aeroelasticity

Aeroelasticity studies flexible bodies subject to fluid flow or more precisely, the fluid structure interaction. Applications range from civil engineering (particularly chimneys, roofs and bridges) and bio-science (e.g. blood vessels) to aerospace design, and lack of understanding of aeroelasticity has lead to many, sometimes tragic, design failures. Most research on aeroelasticity was motivated by the desire to build better (faster, lighter, cheaper, etc) aircraft in the last eighty years. In part due to lack of powerful engines many of the earliest airplanes had very light, flexible wings and many crashes could have been avoided by better understanding of aeroelasticity.

A phenomenon of particular concern is aeroelastic instability: In the absence of air flow any small deformation of a flexible body will be reversed by restorative forces, and oscillations will die out quickly due to structural damping. The addition of fluid flow however may alter this benign behavior completely and small deformations may be amplified resulting in structural failure. For example, the development of high-performance monoplane (as opposed to biplane) aircraft in the 1920s was delayed by unexpected aeroelastic instabilities (static divergence) (Bhatia (2003)).

Since then, aeroelastic analysis has become an established part of aircraft design: "Today, every crewed vehicle that flies through our atmosphere undergoes some level of aeroelastic analysis before flight and virtually every major uncrewed flight vehicle is similarly analyzed." (Schuster et al. (2003)) Many of the aeroelastic behaviors of interest, such as steady-state deformations during flight and instabilities such as flutter, may be predicted by simulations, but wind tunnel tests and flight tests are still indispensable tools. Wind-tunnel tests can easily cost millions of dollars and many months of development time (Bhatia (2003)), therefore improvements in the accuracy and reliability of simulations are highly welcome. Unfortunately analyzing all relevant flight scenarios of an airplane design requires thousands of load cases (Bhatia (2003)), thus limiting the use of high-fidelity simulations by the availability of computational resources and lack of automation.

This section will give a brief review of three aeroelastic instabilities: static divergence, flutter and limit cycle oscillations. A much broader introduction to aeroelasticity, including applications in civil engineering is provided by Clarke et al. (2005). Wright and Cooper (2007) and most recently Rodden (2011) offer an equally detailed treatment focusing on fixed wings (as opposed to propeller blades for example). Hodges (2012) gives a much briefer introduction, also limited to fixed wing applications in aerospace. Bisplinghoff et al. (1962) may be somewhat outdated, but includes one of the most detailed histories of aeroelasticity starting at the beginning of the 20th century.

2.3.1 Aeroelastic Instabilities

Of the many known aeroelastic instability scenarios, this section will only discuss flutter, divergence and subcritical limit cycle oscillations of fixed wings in subsonic flow because of their relevance to the results presented in Section 4. Equally important instabilities due to closed-loop control systems, transonic shocks etc are found in many textbooks (Clarke et al. (2005); Rodden (2011); Wright and Cooper (2007)). This section will introduce instabilities in a conceptual way with the goal of intuitive understanding of the mechanisms. A more rigorous derivation based on

the equations of motion, geared towards numerical analysis, follows in Section 2.3.2.

As mentioned earlier, in the absence of air flow any small deformation of a flexible body will be reversed by restorative forces and oscillations will die out quickly due to structural damping. The addition of fluid flow however may alter this benign behavior completely and small deformations may be amplified resulting in structural failure. Typically, as the flow velocity is increased steadily, some type of instability will eventually occur at the so-called critical velocity. The instability may be classified based on the type of motion: Flutter is characterized by oscillations of increasing amplitude. In experiments the amplitudes can grow very quickly, exceeding the limits of structural integrity so fast that it is referred to as "explosive flutter". Divergence can be defined as the special case of zero oscillation frequency, that is part of the structure just snaps of in one motion. Limit cycle oscillation on the other hand generally does not result in complete failure. Here the oscillation amplitude only grows to a certain level at which the oscillation becomes relatively stable. This is often due to nonlinear damping effects that are strong enough to limit the oscillation to a certain range. Depending on affected components and the amplitude and frequency, the effects of limit-cycle oscillations range from mere nuisance to unacceptable degradation of ride comfort, maneuverability and accelerated material fatigue.

Static Divergence

A simple two-dimensional example where divergence may occur is shown in Figure 2.5, which shows a rigid surface attached to a spring loaded pivot point. Intuitively one may see that the horizontal airflow from the left will act to increase the angle between the surface and the horizontal. This rotation is opposed by the spring force pushing the surface back towards the horizontal. It appears that both the moment exerted by the aerodynamic forces and the restorative moment of the spring increase with the rotation angle of the surface. If the aerodynamic moment grows faster than the spring moment the scenario is unstable and any small rotation will grow, possibly breaking the spring. This is just a very simple example, but it shows two common

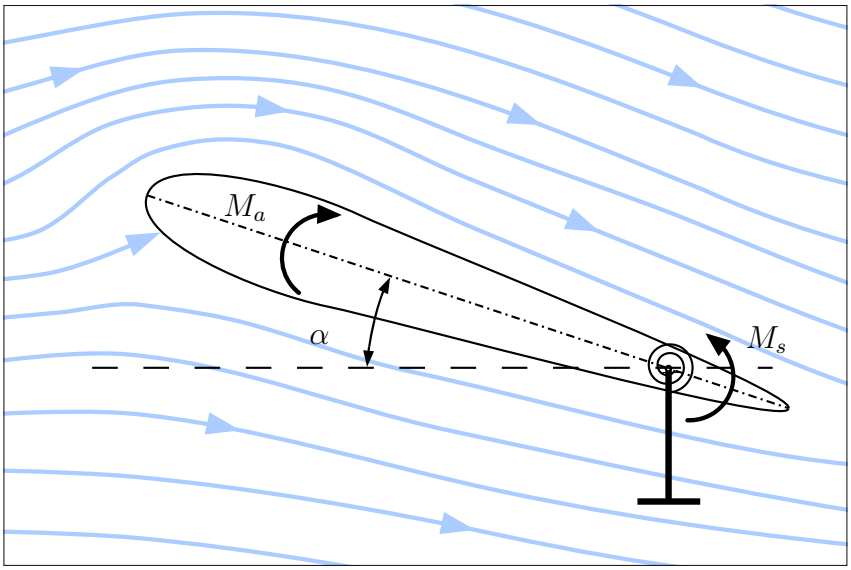

Figure 2.5: Scenario of static divergence if $\frac{\partial M_a}{\partial \alpha} > \frac{\partial M_s}{\partial \alpha}$.

properties of static divergence: First the resultant aerodynamic forces generally apply upstream of where the wing is fixed. Forward swept wings are much more susceptible to this instability. Second, to classify a situation as stable or not stable, dynamic effects often need not be taken into account. The term static divergence may be misleading, because the actual phenomenon is not static at all. When a wing goes through static divergence it may in fact look like an explosion, but it is called "static" because the speed at which this happens may be predicted using static analysis. That is, one can assume a steady state when studying the aerodynamic and structural forces with respect to deformation to discern stability, which greatly simplifies the analysis as discussed in Section 2.3.2.

Flutter

The occurrence of amplified oscillations is not understood as intuitively as static divergence. Here inertia effects, both of the structure and the fluid, play a prominent role and a quasi-steady analysis will fall short. However, oscillations as a result of steady airflow are often encountered. Musical instruments, such as flute and trumpet

use this effect to generate sounds. A flag "fluttering" in the wind is another example. Flutter is often predicted based on linear models that assume displacements to be small and do not take into account structural damping and other nonlinear effects. If the system is unstable, small oscillations will quickly grow in amplitude and the linear assumptions are no longer valid. At this point, two scenarios are possible:

- The oscillations continue to grow until structural failure occurs. This is generally referred to as flutter.
- Nonlinear effects provide sufficient damping to restrict the oscillations to a relatively small, sustained amplitude. This is referred to as limit cycle oscillation (LCO).

Under this definition, the examples of the fluttering flag and wind instruments would be considered limit cycle oscillations, since they are obviously limited in amplitude and do lead to structural failure. In terms of aerospace design, limit cycle oscillations may be tolerated to some extend, but flutter must be avoided at all cost. Generally, flutter predicted based on a linear model may turn out as limit cycle oscillation in experiments. Rigorous analysis of flutter based on the equations of motion is covered in Section 2.3.2.

Limit Cycle Oscillations (LCO)

As described in Section 2.3.1, limit cycle oscillation is a self-sustained vibration of limited amplitude, which only occurs in nonlinear systems. It is usually not a dramatic event, but LCO might hamper, for instance, control and maneuverability and has therefore emerged as an interesting design challenge (Kousen and Bendiksen (1994); Dowell and Tang (2002)). From a design point of view, the challenge lies in developing approaches to manage LCO and mitigate their effects in a way prescribed by the designer.

It is commonly accepted that two situations might be associated with LCO:

- In the transonic regime, shock waves can trigger LCO. Wing configurations

involving stores and missiles (e.g., F-16) are particularly prone to LCO (Beran et al. (2004)).

- Structural nonlinearities can also be at the origin of LCO. Such nonlinearities are found in high aspect ratio wings, such as those found in high altitude surveillance airplanes, and are characterized by a high flexibility and large deformations (Patil et al. (2001)).

Therefore, LCO are sustained by either aerodynamic nonlinearities and/or structural nonlinearities (Lee et al. (1999b)). In some situations, it might be difficult to clearly separate the contributions of these two factors. Studies have typically focused on one or the other (Kousen and Bendiksen (1994); Dowell and Tang (2002); Patil et al. (2001)). In this work, only LCO due to structural nonlinearities will be considered.

LCO may be categorized as "subcritical" or "supercritical" to distinguish whether oscillations appear before or after the critical velocity at which the linearized system experiences flutter. Subcritical LCO require a special treatment in aeroelastic design not only because they appear before the critical flutter velocity, but also because they lead to discontinuous responses that hamper the use of classical computational design tools for optimization or reliability assessment. Figure 2.6 schematically shows the amplitude of oscillations for subcritical and supercritical LCO.

2.3.2 Aeroelastic Analysis

The following sections are dedicated to aeroelastic stability analysis, which is generally the first step of any aeroelastic analysis (Schuster et al. (2003)). Other important aspects of aeroelastic analysis such as trim or gust response analysis are not treated here, since this section is focused on the models used in Chapter 4. The discussion of flutter and static divergence speed is limited to fixed wing models who's structure is represented by linear finite elements. Further, only subsonic compressible potential flow is considered as a model to predict aerodynamic forces. Discussion of limit cycle oscillation is limited to models with structural nonlinearities.

Section 2.3.3 derives the equations of motion for linear flutter analysis and introduces the solution techniques routinely employed in industry. Section 2.3.1 treats the prediction of static divergence as a special case of flutter analysis that is greatly simplified by the elimination of inertia effects. Section 2.3.1 introduces limit cycle oscillation as flutter where the amplitude of oscillation is limited by structural nonlinearities represented by nonlinear springs.

2.3.3 Flutter Analysis

This section will present the classical aeroelastic equations of motion, relating structural deformations and aerodynamic forces, for the investigation of dynamic instabilities (flutter) in fixed wings exposed to uniform airflow. In accordance with practical applications it is assumed that the structure is modeled via linear finite elements, but it should be mentioned that aeroelastic stability analysis of simple systems is possible without resorting to finite element methods. Many textbooks, such as Hodges and Pierce (2011) present mechanical setups that are analyzed purely based on simple dynamics and beam theory. The theory of finite elements is not discussed in any detail and the interested reader is referred to the multitude of available textbooks, Fish and Belytschko (2007) for example offers an excellent introduction.

The effect of the free stream fluid velocity on dynamic stability is the following.

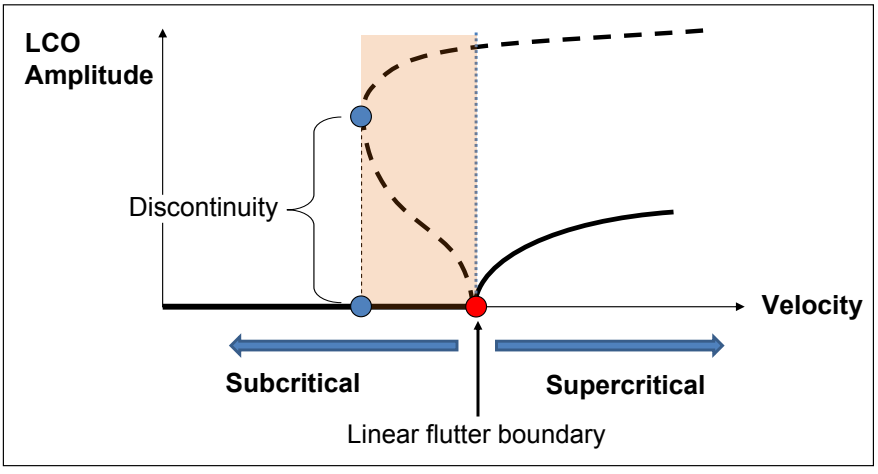

Figure 2.6: LCO amplitude in the sub- and supercritical regions.

At zero velocity the air has a minimal damping effect on structural deformation due to the effort associated with the displacement of air. As the velocity increases the damping effect generally increases initially, but if the velocity is increased further, this trend is often reversed. For many structures a velocity threshold exists at which the dampening effect of the airflow reverses. Beyond this flutter velocity the aerodynamic forces feed oscillations which grow until structural failure occurs. The general approach for determining the flutter velocity is to assume the existence of steady harmonic oscillations of deformation at the flutter velocity. An iterative process is employed to determine the fluid velocity and the oscillation that satisfy the equation of motion.

State Space

In the finite element method the deformation of a flexible structure is represented by the displacements of a finite set of locations (nodes). These nodes are connected by elements representing relationships between the displacements based on geometry and material properties. Assuming linear relationships between the stress and strain in each element, and further assuming that the nodal displacements are small and structural damping is negligible, the deformation of this discretized structure is governed by the following equation of motion:

$$\hat{\boldsymbol{M}}\ddot{\tilde{\boldsymbol{x}}}(t) + \hat{\boldsymbol{K}}\tilde{\boldsymbol{x}}(t) = \hat{\boldsymbol{f}}(t) \tag{2.49}$$

where $\tilde{\boldsymbol{x}}$ is the vector of time dependent nodal displacements and $\ddot{\tilde{\boldsymbol{x}}}$ is its second time derivative. The mass matrix $\hat{\boldsymbol{M}}$ represents inertia effects, the stiffness matrix $\hat{\boldsymbol{K}}$ models the flexibility of the structure, and $\hat{\boldsymbol{f}}$ represents the external forces applied to the structure including aerodynamic forces.

The simpler steady state equation with constant displacement and applied forces is given as:

$$\hat{\boldsymbol{K}}\tilde{\boldsymbol{x}}_s = \hat{\boldsymbol{f}}_s \tag{2.50}$$

For the purpose of stability analysis the system is often linearized with respect to

the steady state solution $\tilde{\boldsymbol{x}}_s$ via coordinate transformation:

$$\boldsymbol{x}(t) = \tilde{\boldsymbol{x}}(t) - \tilde{\boldsymbol{x}}_s \tag{2.51}$$

Which leads to the following equation of motion in which $\hat{\boldsymbol{f}}_a$ represents the transient aerodynamic forces caused by deformation from the steady state:

$$\hat{\boldsymbol{M}}\ddot{\boldsymbol{x}}(t) + \hat{\boldsymbol{K}}\boldsymbol{x}(t) = \hat{\boldsymbol{f}}_a(\boldsymbol{x}(t)) = \hat{\boldsymbol{f}}(t) - \hat{\boldsymbol{f}}_s \tag{2.52}$$

The notation $\hat{\boldsymbol{f}}_a(\boldsymbol{x}(t))$ indicates that the aerodynamic forces are a function not only of the current displacements, but the complete history of displacements and could be of the form: $\hat{\boldsymbol{f}}_a = \int \ldots \boldsymbol{x}(t)\mathrm{d}t$

Equation 2.52 is a closed-loop system and it is stable if any arbitrary small deformation $\boldsymbol{x}_0$ converges to zero. It is possible to use Equation 2.52 directly, for example by employing unsteady computational fluid dynamics (CFD) to obtain the aerodynamic forces. Here the fluid velocity would be increased slowly while simulating the system in a time-marching scheme until either the displacements diverge or the maximum velocity of interest is reached. However this approach is computationally very expensive and, therefore, the following sections will transform the equation of motion to allow for more efficient methods of linear flutter analysis commonly used in industry (Schuster et al. (2003)).

Modal Approach

A coordinate transformation $\boldsymbol{\Phi}$ will express the displacements in terms of the eigenmodes of the structure. The rationale of using this particular transformation is that flutter is most often characterized by interactions of the first few modes, and using as few as ten modes the flutter speed of a wing may be determined accurately (Zona (2011)). In contrast, the number of structural nodes is often in the thousands, so the transformation reduces the number of coordinates by orders of magnitude:

$$\boldsymbol{x}(t) = \boldsymbol{\Phi}\boldsymbol{q}(t) \tag{2.53}$$

with the generalized coordinates $\boldsymbol{q}(t)$. Each column of $\boldsymbol{\Phi}$ is an eigenvector $\boldsymbol{\phi}_i$ of the structure, that is $\boldsymbol{x}(t) = \boldsymbol{\phi}_i \sin(\omega_i t)$ with eigenvalue ω_i is a solution of the

homogeneous equation:

$$\hat{\boldsymbol{M}}\ddot{\boldsymbol{x}}(t) + \hat{\boldsymbol{K}}\boldsymbol{x}(t) = 0 \tag{2.54}$$

Substitution and premultiplication with $\boldsymbol{\Phi}^T$ yields the transformed equation of motion:

$$\boldsymbol{\Phi}^T\hat{\boldsymbol{M}}\boldsymbol{\Phi}\,\ddot{\boldsymbol{q}}(t) + \boldsymbol{\Phi}^T\hat{\boldsymbol{K}}\boldsymbol{\Phi}\,\boldsymbol{q}(t) = \boldsymbol{\Phi}^T\hat{\boldsymbol{f}}_a(\boldsymbol{\Phi}\boldsymbol{q}(t)) \tag{2.55}$$

$$\boldsymbol{M}\ddot{\boldsymbol{q}}(t) + \boldsymbol{K}\boldsymbol{q}(t) = \boldsymbol{f}_a(\boldsymbol{q}(t)) \tag{2.56}$$

where Equation 2.56 implicitly defines the transformed mass matrix $\boldsymbol{M}$, stiffness matrix $\boldsymbol{K}$ and aerodynamic forces $\boldsymbol{f}_a$ as:

$$\boldsymbol{M} = \boldsymbol{\Phi}^T\hat{\boldsymbol{M}}\boldsymbol{\Phi} \tag{2.57}$$

$$\boldsymbol{K} = \boldsymbol{\Phi}^T\hat{\boldsymbol{K}}\boldsymbol{\Phi} \tag{2.58}$$

$$\boldsymbol{f}_a(\boldsymbol{q}(t)) = \boldsymbol{\Phi}^T\hat{\boldsymbol{f}}_a(\boldsymbol{\Phi}\boldsymbol{q}(t)) \tag{2.59}$$

Amplitude Linearization

A common assumption is that dynamic stability can be determined based on convergence of infinitesimal displacements from the steady state. This is generally not true in the case of limit cycle oscillations, but it leads to great simplifications for flutter analysis. Based on the assumption of small displacements it is reasonable to assume that the resulting aerodynamic forces are linear with respect to the deformation:

$$\boldsymbol{f}_a(k_1\boldsymbol{q}_1(t) + k_2\boldsymbol{q}_2(t)) = k_1\boldsymbol{f}_a(\boldsymbol{q}_1(t)) + k_2\boldsymbol{f}_a(\boldsymbol{q}_2(t)) \tag{2.60}$$

with constant factors k_1 and k_2. Further assuming a zero initial displacement completes the requirements of a continuous linear time-invariant system for which several useful theorems are available. Specifically, the outputs (aerodynamic forces $\boldsymbol{f}_a(t)$) are related to the inputs (displacement $\boldsymbol{x}(t)$) by the convolution integral:

$$\boldsymbol{f}_a(\boldsymbol{q}(t)) = \int_0^t \tilde{\boldsymbol{H}}(t-\tau)\,\boldsymbol{q}(t)\,\mathrm{d}\tau \tag{2.61}$$

where $\tilde{\boldsymbol{H}}(t)$ is a matrix consisting of the (generally unknown) system's response to input pulses. However, it is more common to assume an impulse response that is linear with respect to the free stream dynamic pressure q_∞ and scale the argument by the free stream velocity V divided by a reference length L, which is often defined as half of the average chord length:

$$\boldsymbol{f}_a(\boldsymbol{q}(t)) = \int_0^t q_\infty \boldsymbol{H}\left(\frac{V}{L}(t-\tau)\right)\boldsymbol{q}(t)\,\mathrm{d}\tau \tag{2.62}$$

Frequency Domain

In order to simplify the analysis, the problem is transferred to the frequency domain via the Laplace transform defined as:

$$\mathcal{L}\{y(s)\} = \int_0^\infty e^{-st}y(t)\,\mathrm{d}t = \check{y}(s) \tag{2.63}$$

where the unusual $\check{}$ notation is chosen to maintain the convention that bold uppercase letters denote matrices. Equation 2.62 is transformed using the convolution theorem providing the Laplace transform of a convolution integral as:

$$\mathcal{L}\left\{\int_0^t f(t)g(t-\tau)\mathrm{d}\tau\right\} = \mathcal{L}\{f(t)\}\,\mathcal{L}\{g(t)\} \tag{2.64}$$

This yields:

$$\check{\boldsymbol{f}}_a(s) = q_\infty \check{\boldsymbol{H}}\left(\frac{V}{L}s\right)\check{\boldsymbol{q}}(s) \tag{2.65}$$

with $\check{\boldsymbol{H}}$ known as the aerodynamic transfer function that relates aerodynamic forces to displacements in the Laplace domain.

Transformation of the Equation of motion 2.56 also requires the theorem applicable to time differentials of signals with zero initial condition:

$$\mathcal{L}\left\{\ddot{f}(t)\right\} = s^2\mathcal{L}\{f(t)\} \tag{2.66}$$

Now the Equation of motion 2.56 maybe transferred to the Laplace domain as:

$$\boldsymbol{M}s^2\check{\boldsymbol{q}}(s) + \boldsymbol{K}\check{\boldsymbol{q}}(s) = q_\infty\check{\boldsymbol{H}}\left(\frac{L}{V}s\right)\check{\boldsymbol{q}}(s) \tag{2.67}$$

It is generally possible to obtain the aerodynamic transfer function $\check{\boldsymbol{H}}$ in the s-domain to solve the equation of motion for $\check{\boldsymbol{q}}$, which would then be transformed back to the time domain via inverse Laplace transform. However it is much more efficient to restrict solutions to the positive complex axis of the s-domain, which corresponds to simple harmonic motion of the structure. This greatly simplifies the calculation of the aerodynamic transfer function, but has the disadvantage that the equation of motion 2.67 generally does not have such a solution. In fact, such a harmonic solution only exists at certain velocities, the lowest positive of which is defined as the flutter velocity. At all other velocities oscillations will either die out (stable behavior) or grow exponentially (unstable). The corresponding equation of motion is obtained by substituting $i\omega$ for s, with ω being the frequency of the harmonic oscillation:

$$-\omega^2 \boldsymbol{M}\check{\boldsymbol{q}}(i\omega) + \boldsymbol{K}\check{\boldsymbol{q}}(i\omega) = q_\infty \check{\boldsymbol{H}}\left(\frac{L}{V}i\omega\right)\check{\boldsymbol{q}}(i\omega) \tag{2.68}$$

This equation is commonly expressed using the reduced frequency k:

$$k = \frac{L\omega}{V} \tag{2.69}$$

$$\left(-\omega^2 \boldsymbol{M} + \boldsymbol{K} - q_\infty \check{\boldsymbol{H}}\left(ik\right)\right)\check{\boldsymbol{q}}(i\omega) = 0 \tag{2.70}$$

Solution techniques for this equation are presented in Section 2.3.3 after a brief discussion of modeling the unsteady aerodynamics.

Aerodynamic Models

Solving the flutter equation 2.70 requires a model of the aerodynamic forces that act on the structure. This section will be restricted to a brief description of the model used to obtain the aerodynamic forces in the subsonic model presented in the results section. A concise overview of aerodynamic models relevant to aeroelastic analysis is provided in many text books, for example chapter 3 of Rodden (2011). The ZAERO theory manual (Zona (2011)) is also a very good reference, especially with respect to numerical implementation.

In subsonic unsteady potential flow theory, it is assumed that the velocity field is governed by a potential ϕ such that the components of the fluid velocity along the x, y and z coordinates are given as:

$$\begin{aligned} u(x,y,z) &= \frac{\partial\phi(x,y,z)}{\partial x} \\ v(x,y,z) &= \frac{\partial\phi(x,y,z)}{\partial y} \\ w(x,y,z) &= \frac{\partial\phi(x,y,z)}{\partial z} \end{aligned} \tag{2.71}$$

where u, v and w are the components of fluid velocity along the x, y and z coordinates and $\omega(x,y,z)$ is the velocity potential. Given a steady stream of fluid along the x-axis, the velocity potential around an obstacle (wing) is approximately governed by

$$(1 - M_\infty)\,\phi_{xx} + \phi_{yy} + \phi_{zz} - 2\frac{M_\infty}{a_\infty}\phi_{xt} - \frac{1}{a_\infty^2}\phi_{tt} = 0 \tag{2.72}$$

where it is assumed that the disturbances from the steady flow are small. M_∞ and a_∞ are respectively the Mach number and the speed of sound of the undisturbed flow, and the indices denote partial derivatives. In the case where the movement of the wing is given by a simple harmonic motion, the potential equation can be solved numerically relatively efficiently in the Laplace domain. In general, the numerical solution involves dividing the surface of the wing into small elements, each containing one control point. At each control point the velocity potential is obtained, which also yields the pressure on the surface based on the assumption of adiabatic flow:

$$p = p_\infty \left(1 - \frac{\gamma}{a_\infty^2}\left(V_\infty\phi_x + \phi_t\right)\right)^{\frac{\gamma}{\gamma-1}} \tag{2.73}$$

where p_∞ and V_∞ denote the pressure and velocity of the undisturbed flow and γ is the ratio of the specific heat at constant pressure to the specific heat at constant volume of the fluid. The aerodynamic forces at the control points of the wing are obtained by integration of the surface pressure. The equivalent generalized forces on the structural model are provided by a spline model, which converts forces and displacements between the structural finite element model and the aerodynamic mesh.

Flutter Solution Methods

After deriving the equations of motion in the Laplace domain in Section 2.3.3, the current Section discusses several solution techniques to determine the stability boundary. To improve readability, the equation of motion in the Laplace domain and the equation for harmonic motion, often referred to as the flutter equation, are repeated here:

$$\boldsymbol{M}s^2\check{\boldsymbol{q}}(s) + \boldsymbol{K}\check{\boldsymbol{q}}(s) = q_\infty \check{\boldsymbol{H}}\left(\frac{L}{V}s\right)\check{\boldsymbol{q}}(s) \tag{2.74}$$

$$\left(-\omega^2\boldsymbol{M} + \boldsymbol{K} - q_\infty \check{\boldsymbol{H}}\left(ik\right)\right)\check{\boldsymbol{q}}(i\omega) = 0 \tag{2.75}$$

The basic concept, shared by the following solution methods, is to modify the flutter equation by adding a damping term so that it has solutions for all velocities. This equation is then solved for a list of velocities and interpolated to obtain the solution with zero added damping (if it exists).

The K-method, also referred to as the American method, introduces artificial structural damping that is proportional to the stiffness as first proposed by Theodorson (1935):

$$\left(-\omega^2\boldsymbol{M} + (1+ig_s)\boldsymbol{K} - q_\infty \check{\boldsymbol{H}}\left(ik\right)\right)\check{\boldsymbol{q}}(i\omega) = 0 \tag{2.76}$$

where g_s is a real number. The dynamic pressure q_∞ is then expressed in terms of the reduced frequency k (Equation 2.69) and fluid density ρ:

$$q_\infty = \frac{1}{2}\rho V_\infty^2 = \frac{1}{2}\rho\left(\frac{\omega L}{k}\right)^2 \tag{2.77}$$

and the resulting equation is divided by ω^2 to obtain:

$$\left(\boldsymbol{M} + \frac{\rho}{2}\left(\frac{L}{k}\right)^2 \check{\boldsymbol{H}}\left(ik\right) + \frac{1+ig_s}{\omega^2}\boldsymbol{K}\right)\check{\boldsymbol{q}} = 0 \tag{2.78}$$

A final substitution for the coefficient of K gives the final flutter equation for the K-method:

$$\lambda = \frac{1+ig_s}{\omega^2} \tag{2.79}$$

$$\left(\boldsymbol{M} + \frac{\rho}{2} \left(\frac{L}{k} \right)^2 \check{\boldsymbol{H}} (ik) + \lambda \boldsymbol{K} \right) \check{\boldsymbol{q}} = 0 \tag{2.80}$$

Now the eigenvalue problem of Equation 2.80 is solved for a list of reduced frequencies k_i. For each k value there are as many solutions as generalized coordinates, and a mode tracking scheme is employed to discover all solutions: At the highest k value the influence of the aerodynamic forces is smallest and the n eigenvalues λ_j are closest to $\frac{1}{\omega_j^2}$, with ω_j being the n eigenfrequencies of the structure. As k is reduced incrementally, the eigenvalues λ_j are solved for iteratively, using the solutions of the previous k value as initial guesses. Assuming a list of m reduced frequencies and n generalized coordinates, $m \times n$ eigenvalues are obtained. The oscillation frequency ω, damping factor g_s and air speed V may be recovered from each eigenvalue λ:

$$\omega = \frac{1}{\sqrt{\Re(\lambda)}} \tag{2.81}$$

$$g_s = \omega^2 \Im(\lambda) = \frac{\Im(\lambda)}{\Re(\lambda)} \tag{2.82}$$

$$V = \frac{\omega L}{k} \tag{2.83}$$

Note that a positive real valued frequency and velocity may not be obtained if the real part of λ is negative. The flutter velocity is the lowest velocity at which the damping factor g_s switches from negative positive for any of the generalized coordinates. These results are typically presented by plotting the damping values g_s and the frequencies ω associated with each generalized coordinate with respect to velocity V as shown in Figure 2.7.

Though the K-method has been used extensively and successfully in industry, it is no longer considered the state of the art. The disadvantages of the K-method are the following:

- During the calculation of the aerodynamic forces $\check{\boldsymbol{H}}$, a certain Mach number must be assumed and during the solution process a fluid density is also assumed and then the flutter velocity is obtained from the solution. However this velocity is generally inconsistent with the assumed air density, Mach number

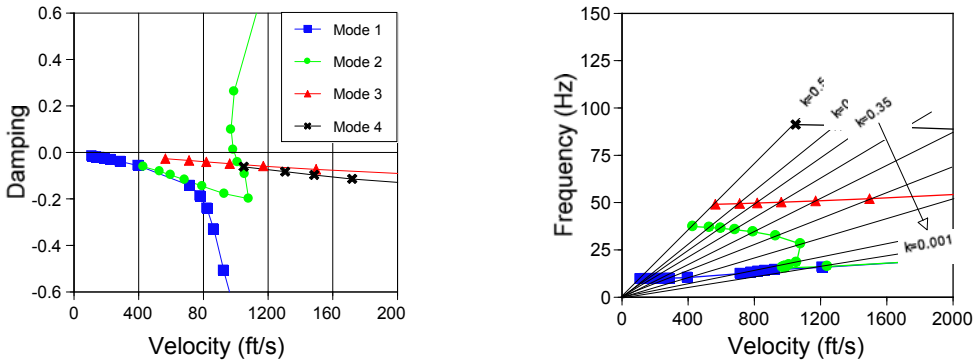

Figure 2.7: Typical results of K-method presented in Zona (2011): The damping value g_s and the frequency ω are plotted for each of the four generalized coordinates with respect to velocity V.

and the standard atmosphere on earth. The K-Method is therefore a non-matchpoint analysis.

- The assumed damping factor does not have much physical significance. It may actually be multi-valued with respect to velocity as shown in Figure 2.7.
- Solutions of the flutter equation with zero frequency, which are physically significant as static divergence, may not be obtained, because of the formulation of the eigenvalue problem (Equation 2.79).

These shortcomings are addressed by the following P-K-Method and G-Method which are modifications of the original K-Method.

The P-K-method, also called the English method, was originally proposed by Irwin and Guyett (1965) and later modified by Rodden et al. (1979) to its current form. It seeks solutions of the following equation of motion (Equation 2.84), and the K-method equation is shown for comparison (Equation 2.85):

$$\left(\gamma(\gamma+2i)\check{\boldsymbol{M}} - \gamma q_\infty \Im\left(\check{\boldsymbol{H}}(ik)\right) - \omega^2\boldsymbol{M} + \boldsymbol{K} - q_\infty\check{\boldsymbol{H}}\left(ik\right)\right)\check{\boldsymbol{q}}(i\omega) = 0 \qquad (2.84)$$

$$\left(ig_s\boldsymbol{K} - \omega^2\boldsymbol{M} + \boldsymbol{K} - q_\infty\check{\boldsymbol{H}}\left(ik\right)\right)\check{\boldsymbol{q}}(i\omega) = 0 \qquad (2.85)$$

The P-K-method uses real parameter γ to introduce artificial damping via the mass matrix $\check{\boldsymbol{M}}$ and the real imaginary part of the aerodynamic forces $\Im\left(\check{\boldsymbol{H}}(ik)\right)$. The

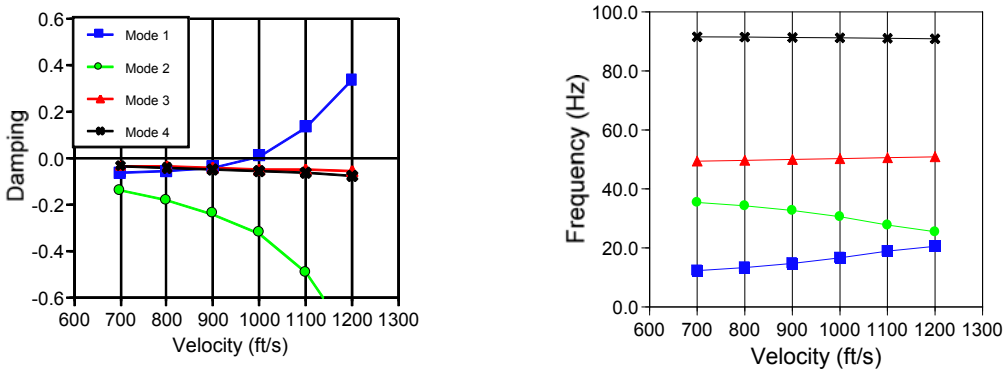

Figure 2.8: Typical results of P-K-method presented in Zona (2011): The damping value γ and the frequency ω are plotted for each of the four generalized coordinates with respect to velocity V.

K-method, on the other hand, uses real parameter g_s to introduce artificial damping via the stiffness matrix. For given pairs of velocity V and fluid density ρ, Equation 2.84 is solved for γ and k via an iterative procedure. One such algorithm is detailed in Rodden and Johnson (1994). Figure 2.8 shows the results of a flutter analysis using the P-K-method for the same problem as in Figure 2.7.

Both the K-Method and the P-K-Method have been widely used in practice and are discussed in virtually every textbook on aeroelasticity. The P-K-Method is generally preferred and may be considered the standard for linear flutter analysis, due to the following advantages:

- Equation 2.84 is solved for selected velocity/density pairs and the corresponding Mach number is used the calculate the aerodynamic forces. This means the analysis is a match point analysis, consistent with the standard atmosphere.

- The obtained damping values, for example in Figure 2.8, are generally perceived to be more realistic and never multi-valued with respect to velocity.

- Because of it's formulation, the P-K-method can obtain solutions with zero frequency ω, corresponding to static divergence.

The G-Method (Chen (2000)) is another variation of the K-method that is implemented in ZAERO Zona (2011). Its main advantage over the P-K-method is that it generally provides a more realistic approximation of the damping coefficient. The flutter equation is formulated in the s domain as:

$$\left(\frac{V^2}{L^2}p^2\boldsymbol{M} + \boldsymbol{K} - \frac{1}{2}\rho V^2 \check{\boldsymbol{H}}\left(p\right)\right)\check{\boldsymbol{q}}(i\omega) = 0 \tag{2.86}$$

$$p = g + ik = k\gamma + ik \tag{2.87}$$

This is quite similar to the P-K-method equation, which may be written as:

$$\left(\frac{V^2}{L^2}p^2\boldsymbol{M} + \boldsymbol{K} - \frac{1}{2}\rho V^2 \Im\left(\check{\boldsymbol{H}}\left(ik\right)\right)\gamma - \frac{1}{2}\rho V^2 \check{\boldsymbol{H}}\left(ik\right)\right)\check{\boldsymbol{q}}(i\omega) = 0 \tag{2.88}$$

$\check{\boldsymbol{H}}$ is only available along the positive complex axis, therefore the G-method uses a linear Taylor series:

$$\check{\boldsymbol{H}}(p) \approx \check{\boldsymbol{H}}(ik) + g\left.\frac{\partial \check{\boldsymbol{H}}(p)}{\partial g}\right|_{g=0} \tag{2.89}$$

The partial derivative may be transformed based on the Cauchy-Riemann equations, such that only the function along the complex axis need to be known:

$$\left.\frac{\partial \check{\boldsymbol{H}}(p)}{\partial g}\right|_{g=0} = \frac{d\check{\boldsymbol{H}}(ik)}{d(ik)} \tag{2.90}$$

which can be approximated by numerical differentiation (finite differences).

Both the P-K-Method and the G-Method are well suited to predict both flutter and static divergence instabilities and will determine the same maximum velocity. However, one may argue that the G-method is more rigorously derived and provides more realistic damping values over the whole velocity range. It has also been shown that the G-method will detect bifurcations in the roots of the flutter equation, where additional solutions (aerodynamic lag roots) appear at a certain velocities. Using the P-K-method, these bifurcations may cause discontinuities in the damping values with respect to the velocity, whereas the damping values obtained by the G-method are continuous with respect the velocity (Zona (2011)).

Various software packages are available for the linear flutter analysis described in this section, but large airspace companies often prefer their own proprietary solutions due to better integration into their design process (Bhatia (2003)). Experienced engineers routinely perform linear flutter analysis with relative ease and it is therefore considered a mature science (Schuster et al. (2003)). However, this generally involves manual selection of parameters affecting fidelity such as mesh density and manual interpretation of results. Completely automated linear flutter analysis still poses considerable challenges: For example even small changes in the natural frequencies can have unexpectedly large effects on the obtained flutter velocity, which is generally linked to the interplay of different modes. As another example, interpolation error in the calculation of aerodynamic forces may lead to "spurious" roots of the flutter equation, causing underestimation of the flutter speed (Zona (2011)).

2.3.4 Static Divergence

As described in Section 2.3.3, some flutter solution techniques are capable of predicting static divergence as well. However, if only the prediction of static divergence is desired, then a much simpler static analysis is sufficient. This section describes such analysis suitable for restrained cantilevered wings as proposed by Rodden and Love (1985). Similar algorithms are implemented in virtually all commercial software packages for aeroelastic analysis and extensively covered by textbooks such as Rodden (2011) on which the following derivation is based.

Consider a thin cantilevered wing whose planform in the X-Y plane is represented by a mesh of structural grid points. The airfoil, that is the shape of the cross-section of the wing, is approximated by the Z-coordinates h_i of the grid points. The airflow along the X-axis is deflected by the wing and the resulting aerodynamic forces at the grid points $\boldsymbol{f}_a$ may be approximated by a linear equation:

$$\boldsymbol{f}_a = \frac{qS}{c}\boldsymbol{C}_a\boldsymbol{h} \tag{2.91}$$

with dynamic pressure q, reference wing area S, reference chord length c and aerodynamic influence coefficient matrix $\boldsymbol{C}_a$. The aerodynamic influence coefficient matrix $\boldsymbol{C}_a$ is obtained from numerical solution of the static velocity potential equation (Section 2.3.3):

$$(1 - M_\infty)\,\phi_{xx} + \phi_{yy} + \phi_{zz} = 0 \tag{2.92}$$

The fraction $\frac{qS}{c}$ is merely a scaling factor and could be absorbed into the aerodynamic influence coefficient matrix, but the representation above is more common and it is important to realize that the aerodynamic forces are proportional to the dynamic pressure, which is a quadratic function of the uniform velocity of the undisturbed air flow:

$$q = \frac{1}{2}\rho v^2 \tag{2.93}$$

with air density ρ and velocity v. The deviation $\boldsymbol{h}$ from the X-Y plane is comprised of two components

$$\boldsymbol{h} = \boldsymbol{h}_r + \boldsymbol{h}_f \tag{2.94}$$

where $\boldsymbol{h}_r$ represents the known undeformed shape and $\boldsymbol{h}_f$ corresponds to the flexible deflection of the wing, which is related to the aerodynamic forces by the stiffness matrix $\boldsymbol{K}$:

$$\boldsymbol{K}\boldsymbol{h}_f = \boldsymbol{f}_a \tag{2.95}$$

Substitution of Equations 2.94 and 2.95 into Equation 2.91 relates the undeformed shape $\boldsymbol{h}_r$ to the flexible deformations $\boldsymbol{h}_f$:

$$\boldsymbol{K}\boldsymbol{h}_f = \frac{qS}{c}\boldsymbol{C}_a(\boldsymbol{h}_r + \boldsymbol{h}_f) \tag{2.96}$$

which may be written as

$$(\boldsymbol{K} - \frac{qS}{c}\boldsymbol{C}_a)\boldsymbol{h}_f = \frac{qS}{c}\boldsymbol{C}_a\boldsymbol{h}_r \tag{2.97}$$

This equation may only be solved for the flexible deformation $\boldsymbol{h}_f$ if the matrix on the left hand side is nonsingular, therefore the following eigenvalue problem is of special interest:

$$(\boldsymbol{K} - \frac{qS}{c}\boldsymbol{C}_a)\boldsymbol{h}_f = 0 \tag{2.98}$$

Negative values of dynamic pressure q that solve this equation have no physical relevance, but positive solutions signify static divergence. If positive solutions exist, Equation 2.93 may be solved for the lowest critical velocity at which divergence will occur:

$$v_d = 2\rho\sqrt{q} \tag{2.99}$$

2.3.5 Limit Cycle Oscillations

As described in Section 2.3.1, limit cycle oscillations only occur in nonlinear systems. Generally speaking, either aerodynamic or structural nonlinearities must be present. For this reason, only a nonlinear model may predict LCO consistently. In many cases numerical time integration of the state space model is employed to obtain the time history for a given initial state and the presence of LCO must be judged from this time history. For a single simulation this may be done manually by studying the deformation history to detect sustained vibration. However, an automatic detection algorithm is needed when larger numbers of samples are to be evaluated in the context of numerical optimization or uncertainty quantification.

Detection of LCO based on mechanical energy

For the LCO test problem described in Section 4.1, the time response considered is the mechanical energy defined as the sum of the kinetic and the strain energies. This approach has the advantage of encompassing all the degrees of freedom of the system in one quantity. For an asymptotically stable system, the energy will converge to the steady state equilibrium characterized by constant zero kinetic energy and constant potential energy. For a diverging system (static divergence or flutter) the system energy will continue to grow unboundedly. In the case of LCO the mechanical energy will hover consistently above the steady-state level and the kinetic energy will oscillate periodically. Based on this criterion, design configurations may be classified as stable or unstable and the method of support vector machines, described in the following section, may be used to approximate the stability boundary.

2.4 Support Vector Machines (SVM)

This section will focus on a machine learning process, called support vector machine (SVM), that is used throughout this work to approximate the boundaries between feasible and infeasible regions of a parameterized design space. A review of the theory behind SVM in Section 2.4.2 will be followed by a discussion of the advantages and pitfalls in Section 2.4.3. It should be noted that SVM is a very popular approach to the classification problem and a number of classic text books such as Alpaydin (2004); Abe (2010); Schölkopf and Smola (2001) will provide a deeper understanding than the following treatment.

2.4.1 Motivation

Many applications require the classification of samples into one or more classes. Take for example the classification of emails into regular correspondence and spam. Obviously an algorithm that will automatically sort out the spam mail is very useful, but while it is easy for people to recognize unsolicited emails, the underlying "algorithm" is not known and varies between users. What is known, however, is that the decision is based on the content and origin of each message. The email classification problem is therefore a popular application of machine learning algorithms that build a classification function based on empirical data. Such an algorithm would analyze a set of manually classified emails in order to categorize additional emails. Similar problems exist in many areas of science, relating for example to the classification of tissue samples, face recognition and of course, the classification of parameterized designs as feasible or infeasible, which is the topic of this work.

2.4.2 Construction of SVM

The classification problem introduced above is formally defined as follows: Assume an n-dimensional parameter space $S \subset \Re^n$ and a computable, deterministic classifier $c : S \to \{-1, 1\}$ with binary output. Based on a set of training data: $\{\boldsymbol{x}_i, y_i\}$, $i = 1, \ldots, l$, $y_i = c(\boldsymbol{x}_i)$, $\boldsymbol{x}_i \in S$ predict the class (-1 or 1) of any additional

sample $\boldsymbol{x} \in S$. In general, c may be stochastic, but this section will be limited to the deterministic case, relevant to the deterministic simulation models presented in Chapter 4.

Confusingly, the term SVM is generally used both for the predicting function and for the machine learning process, which produces the predicting function. In the first sense, the SVM is a scalar, analytical function $s : S \to \Re$ of the form

$$s(\boldsymbol{x}) = b + \sum_{i=1}^{l} \lambda_i y_i K(\boldsymbol{x}_i, \boldsymbol{x}) \tag{2.100}$$

The training data is incorporated via the kernel function K and the SVM value is a weighted sum with coefficients λ_i and offset b. Ideally, b and λ_i are selected such that the sign of the SVM value predicts the class of any sample:

$$\text{sgn}(s(\boldsymbol{x})) \approx c(\boldsymbol{x}) \tag{2.101}$$

and the most probable approximation of the boundary between the two domains is the zero contour:

$$s(\boldsymbol{x}) = 0 \tag{2.102}$$

To describe the accuracy of the SVM, one distinguishes between the empirical error (training error) and the true error of the SVM. The empirical error quantifies the ability of the SVM to correctly classify the training samples and may be defined as

$$\epsilon_t = \frac{1}{l} \sum_{i=1}^{l} f_e(\boldsymbol{x}_i) \quad \text{with } f_e(\boldsymbol{x}) = \begin{cases} 1 & \text{if } c(\boldsymbol{x}) \neq \text{sgn}(s(\boldsymbol{x})) \\ 0 & \text{otherwise} \end{cases} \tag{2.103}$$

The simulation models presented in this dissertation are deterministic and with proper selection of the kernel function (Section 2.4.2) the SVM will separate the training samples. Therefore all SVMs discussed in Section 4 have zero training error. The true error quantifies the ability of the SVM to correctly classify *any* sample in the design space and is equivalent to the generalization error discussed in Section 2.1.1. Only for very few analytical problems is it possible to calculate the true error exactly. In the general case, the true error is approximated based

on additional samples (validation set), or approximation techniques, such a cross-validation or bootstrapping (Section 2.1.1).

Linear SVM

A linear SVM is obtained if the Euclidean dot-product is used as the kernel function K as proposed by Vapnik (1963).

$$s(\boldsymbol{x}) = b + \sum_{i=1}^{l} \lambda_i y_i (\boldsymbol{x}_i \cdot \boldsymbol{x}) \tag{2.104}$$

This basic case will be used to introduce the maximum-margin concept for the selection of b and λ_i. The SVM boundary simplifies to the equation of a hyper-plane with normal vector $\boldsymbol{w}$:

$$s(\boldsymbol{x}) = b + \boldsymbol{w} \cdot \boldsymbol{x} = 0 \quad \text{with } w_k = \sum_{i=1}^{l} \lambda_i y_i x_{ik} \tag{2.105}$$

Consider a two-dimensional design space as shown in Figure 2.9a, where a deterministic classifier labels any point as belonging to one of two classes, and the corresponding regions are separated by the so-called true boundary. If only the classification of a few points is known, then an infinite number of hyperplanes may separate the two classes of training samples as shown in Figure 2.9b. Without any further assumptions, all of these hyperplanes are equally likely to predict the correct classification of additional points. The SVM learning process, however, is based on the assumption that the most probable boundary lies at maximum distance from the training samples, while separating the two classes, as shown in Figure 2.10. In other words, the SVM boundary maximizes the margin between the parallel support hyper-planes. Equivalently, the SVM boundary is selected to minimize the upper bound of the true classification error under the assumption that the true boundary is actually linear (Vapnik (1963)).

The distance from the linear boundary to the closest of l training samples $\boldsymbol{x}_i$ is given by:

$$\min\{\|\boldsymbol{x} - \boldsymbol{x}_i\| : \boldsymbol{x} \in \Re^N, (\boldsymbol{w} \cdot \boldsymbol{x}) + b = 0, i = 1, \ldots, l\} \tag{2.106}$$

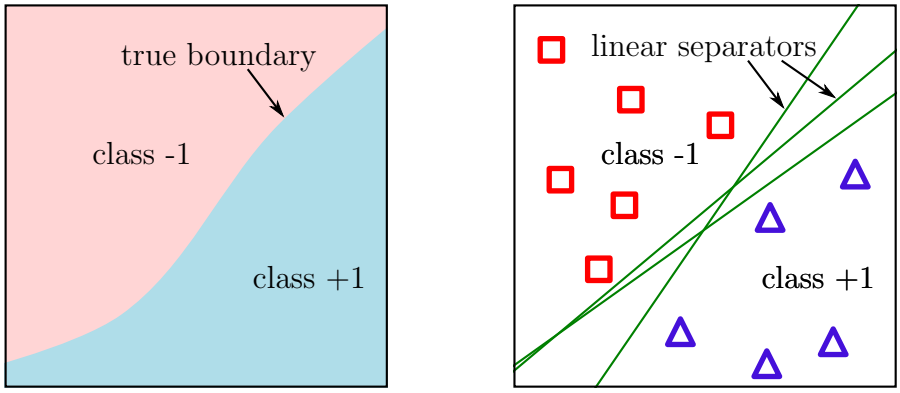

(a) True boundary separating the two different regions of the design space.

(b) Multiple linear functions separating classified training samples.

Figure 2.9: Two-dimensional design space in which a deterministic classifier labels any point as belonging to one of two classes (a) and several hyper-planes separating labeled samples (b).

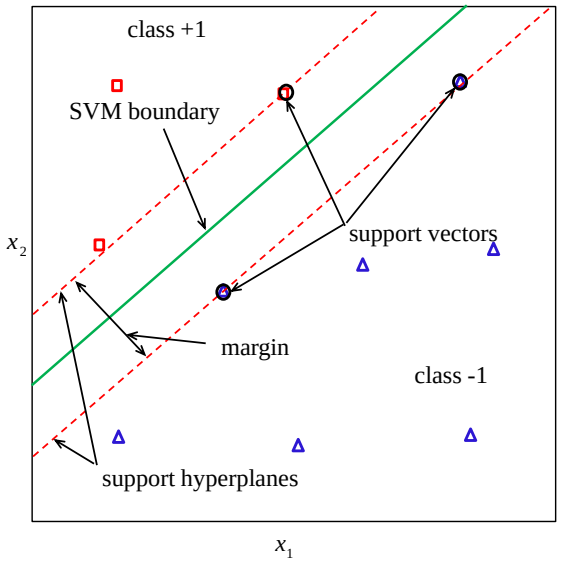

Figure 2.10: Linear SVM decision boundary (Basudhar (2012)).

Now $\boldsymbol{w}$ and b may be selected as the solution of an optimization problem, which maximizes this distance while requiring the boundary to correctly classify each sample:

$$\begin{array}{ll} \max\limits_{\mathbf{w},b} & \min\{\|\boldsymbol{x}-\boldsymbol{x}_i\| : \boldsymbol{x} \in \Re^N, (\boldsymbol{w}\cdot\boldsymbol{x})+b=0, i=1,\ldots,l\} \\ \text{such that} & y_i \cdot (b+\boldsymbol{w}\cdot\boldsymbol{x}_i) > 0 \;\forall\; i=1,\ldots,l \end{array} \tag{2.107}$$

Solution In order to obtain $\boldsymbol{w}$ and b, Equation 2.107 will be transformed into an equivalent quadratic programming problem which is solved very efficiently numerically. In a first step, the parallel support hyperplanes shown in Figure 2.10 are defined as:

$$\begin{aligned} H^+ &= \{\boldsymbol{x} \in \Re^N : b+\boldsymbol{w}\cdot\boldsymbol{x}=1\} \\ H^- &= \{\boldsymbol{x} \in \Re^N : b+\boldsymbol{w}\cdot\boldsymbol{x}=-1\} \end{aligned} \tag{2.108}$$

Considering arbitrary points on each support hyperplane, that is $\boldsymbol{x}^+ \in H^+$ and $\boldsymbol{x}^- \in H^-$, the distance between the two parallel planes d_H is derived as the projection of the difference vector on normal vector $\boldsymbol{w}$:

$$d_H = \frac{\boldsymbol{w}}{\|\boldsymbol{w}\|}\cdot(\boldsymbol{x}^+-\boldsymbol{x}^-) = \frac{1}{\|\boldsymbol{w}\|}(b+\boldsymbol{w}\cdot\boldsymbol{x}^+-(b+\boldsymbol{w}\cdot\boldsymbol{x}^-)) = \frac{2}{\|\boldsymbol{w}\|} \tag{2.109}$$

which is inversely proportional to the magnitude of $\boldsymbol{w}$. Now the parameter selection problem (Equation 2.107) is reformulated such that the distance between the support hyper-planes is maximized while forcing all training samples to remain outside of the volume between the two parallel planes:

$$\min_{\boldsymbol{w},b}\frac{1}{2}\boldsymbol{w}\cdot\boldsymbol{w} \quad \text{such that } 1 \le y_i\cdot(b+\boldsymbol{w}\cdot\boldsymbol{x}_i)\;\forall\; i=1,\ldots,l \tag{2.110}$$

Generally only a fraction of the inequality constraints in Equation 2.110 is active, that is only a few training samples lie exactly on the support hyper-planes (Figure 2.10). These support vectors, defined as:

$$X_{sv} = \{\boldsymbol{x}_i \mid y_i\cdot s(\boldsymbol{x}_i)=1\} \tag{2.111}$$

define the shape of the SVM boundary and only if a support vector is removed from the training set will the solution of Equation 2.110 be different.

In general, the solution z^* of any constrained optimization problem of the form:

$$\begin{aligned} \min_{\boldsymbol{z}} \quad & f(\boldsymbol{z}) \\ \text{such that} \quad & g_i(\boldsymbol{z}) \leq 0 \ \forall \ i = 1, \ldots, m \\ & h_j(\boldsymbol{z}) = 0 \ \forall \ j = 1, \ldots, n \end{aligned} \tag{2.112}$$

is characterized by four necessary Karush-Kuhn-Tucker (KKT) conditions (Karush (1939); Kuhn and Tucker (1951)), which stem from a generalization of the method of Lagrange multipliers:

$$\text{Stationarity: } \nabla f(\boldsymbol{z}^*) + \sum_i \mu_i \nabla g_i(\boldsymbol{z}^*) + \sum_j \tau_j \nabla h_i(\boldsymbol{z}^*) = 0 \tag{2.113}$$

$$\begin{aligned} \text{Primal Feasibility: } & g_i(\boldsymbol{z}^*) \leq 0 \ \forall \ i = 1, \ldots, m \\ & h_j(\boldsymbol{z}^*) = 0 \ \forall \ j = 1, \ldots, n \end{aligned} \tag{2.114}$$

$$\text{Dual Feasibility: } \mu_i \geq 0 \ \forall \ i = 1, \ldots, m \tag{2.115}$$

$$\text{Complementary Slackness: } \mu_i g_i(\boldsymbol{z}^*) = 0 \ \forall \ i = 1, \ldots, m \tag{2.116}$$

with KKT multipliers μ_i and τ_j. Since the objective and constraint functions in Equation 2.110 are continuously differentiable and convex, the KKT conditions are also sufficient and evaluate as:

$$\text{Stationarity: } \boldsymbol{w}^* = \sum_i^l \mu_i y_i \boldsymbol{x}_i \tag{2.117}$$

$$\sum_i^l \mu_i y_i = 0 \tag{2.118}$$

$$\text{Primal Feasibility: } 1 - y_i \cdot (b^* + \boldsymbol{w}^* \cdot \boldsymbol{x}_i) \leq 0 \ \forall \ i = 1, \ldots, l \tag{2.119}$$

$$\text{Dual Feasibility: } \mu_i \geq 0 \ \forall \ i = 1, \ldots, l \tag{2.120}$$

$$\text{Complementary Slackness: } \mu_i (1 - y_i \cdot (b^* + \boldsymbol{w}^* \cdot \boldsymbol{x}_i)) = 0 \ \forall \ i = 1, \ldots, l \tag{2.121}$$

Instead of solving Equations 2.117 to 2.121 directly for $\boldsymbol{w}^*$, b^* and μ_i, the optimization problem is transformed one more time to arrive at a quadratic programming problem. For this purpose, consider the Wolfe duality (Wolfe (1961)) which states that

$$\min_{\boldsymbol{z}} f(\boldsymbol{z}) \ \text{ such that } \ g_i(\boldsymbol{z}) \leq 0 \ \forall \ i = 1, \ldots, m \tag{2.122}$$

has the same solution as its dual:

$$\begin{aligned} &\max_{\boldsymbol{z},\boldsymbol{\mu}} \; f(\boldsymbol{z}) + \sum_{i}^{m} \mu_i g_i(\boldsymbol{z}) \\ &\text{such that } \nabla f(\boldsymbol{z}) + \sum_{i}^{m} \mu_i \nabla g_i(\boldsymbol{z}) = 0 \\ &\mu_i \geq 0 \; \forall \; i = 1, \ldots, l \end{aligned} \tag{2.123}$$

if objective and constraint functions are continuously differentiable and convex. The objective function of the Wolfe dual of Equation 2.110 may be expressed as:

$$\begin{aligned} &\frac{1}{2}\boldsymbol{w}^* \cdot \boldsymbol{w}^* + \sum_{i}^{l} \mu_i \left(1 - y_i \cdot (b^* + \boldsymbol{w}^* \cdot \boldsymbol{x}_i)\right) \\ =&\frac{1}{2}\boldsymbol{w}^* \cdot \boldsymbol{w}^* + \sum_{i}^{l} \mu_i - b^* \sum_{i}^{l} \mu_i y_i - \boldsymbol{w}^* \cdot \sum_{i}^{l} \mu_i y_i \boldsymbol{x}_i \\ =&\sum_{i}^{l} \mu_i - \sum_{i,j}^{l} \mu_i \mu_j y_i y_j \left(\boldsymbol{x}_i \cdot \boldsymbol{x}_j\right) \end{aligned} \tag{2.124}$$

where $\boldsymbol{w}^*$ and b^* are eliminated by substituting the KKT conditions (Equations 2.117 and 2.118). The constraint function of the Wolfe dual is identical to the stationarity KKT condition and simplifies to Equation 2.118. Finally, the Wolfe dual may be expressed as a quadratic programming problem in terms of the vector of multipliers $\boldsymbol{\mu}$:

$$\begin{aligned} \max_{\boldsymbol{\mu}} \quad & \sum_{i}^{l} \mu_i - \sum_{i,j}^{l} \mu_i \mu_j y_i y_j \left(\boldsymbol{x}_i \cdot \boldsymbol{x}_j\right) \\ \text{such that} \quad & \sum_{i}^{l} \mu_i y_i = 0 \\ & \mu_i \geq 0 \; \forall \; i = 1, \ldots, l \end{aligned} \tag{2.125}$$

Even for large sets of training data, Equation 2.125 can always be solved exactly efficiently (Cristianini and Schölkopf (2002)), and an extensive review of solution algorithms is given by Schölkopf et al. (1998). Once the solution $\boldsymbol{\mu}^*$ is known, $\boldsymbol{w}^*$ is provided by Equation 2.117 and b^* is obtained by solving Equation 2.121 using any

non-zero multiplier μ_k^*. Alternatively, the SVM itself is expressed in terms of the multipliers $\boldsymbol{\mu}^*$ and offset b^* by substitution of Equation 2.117 into Equation 2.105:

$$s(\boldsymbol{x}) = b^* + \sum_i^l \mu_i^* y_i (\boldsymbol{x}_i \cdot \boldsymbol{x}) \tag{2.126}$$

Nonlinear SVM

Of course in the general case, training samples may not be separable by a straight hyper-plane. Fortunately, the SVM approach may be expanded to reproduce nonlinear and disjoint boundaries via the so-called "kernel trick" (Aizerman et al. (1964)): By replacing any dot products $\boldsymbol{x} \cdot \boldsymbol{y}$ with a nonlinear scalar kernel function $K(\boldsymbol{x}, \boldsymbol{y})$, as proposed by Boser et al. (1992), it is possible to obtain complex SVM boundaries as shown in Figure 2.11, for example. This modification is equivalent to mapping the training samples $\boldsymbol{x}_i$ into a higher-dimensional feature space F, in which the samples may be separated by a linear hyper-sphere. However, since both the SVM function (Equation 2.126) and the quadratic programming problem (Equation 2.125) only contain the kernel function (dot product), the transition from linear hyper-planes to nonlinear SVM boundaries is rather small and does not actually require a mapping. That is, the new quadratic programming problem and the SVM function are simply given as:

$$\begin{aligned} \max_{\boldsymbol{\mu}} \quad & \sum_i^l \mu_i - \sum_{i,j}^l \mu_i \mu_j y_i y_j K(\boldsymbol{x}_i, \boldsymbol{x}_j) \\ \text{such that} \quad & \sum_i^l \mu_i y_i = 0 \\ & \mu_i \geq 0 \ \forall \ i = 1, \ldots, l \end{aligned} \tag{2.127}$$

and

$$s(\boldsymbol{x}) = b^* + \sum_i^l \mu_i^* y_i K(\boldsymbol{x}_i, \boldsymbol{x}) \tag{2.128}$$

where b^* is obtained by solving the modified KKT complementary condition with nonzero μ_i^*:

$$\mu_i^* (1 - y_i \cdot (b^* + \sum_j^l \mu_j y_j K(\boldsymbol{x}_j, \boldsymbol{x}_i)) = 0 \ \forall \ i = 1, \ldots, l \tag{2.129}$$

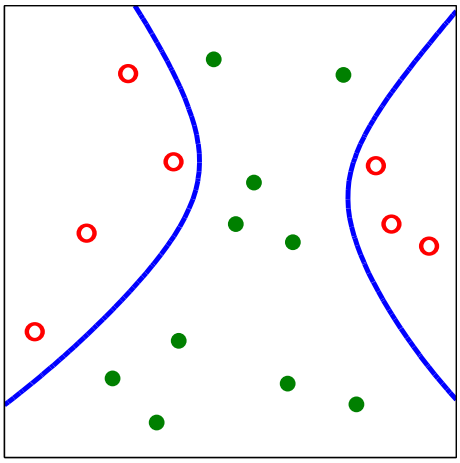

Figure 2.11: Example of nonlinear SVM decision boundary.

Selection of Kernel The choice of kernel function may greatly affect the accuracy of SVM and this situation is similar to the kernel selection problem of radial basis functions (Section 2.1.4). In theory, any scalar function $f(\boldsymbol{x}_i, \boldsymbol{x}_j)$ may be used, but in practice the vast majority of applications resort to one of the following:

- Linear: $K(\boldsymbol{x}_i, \boldsymbol{x}_j) = \boldsymbol{x}_i \cdot \boldsymbol{x}_j$
- Polynomial: $K(\boldsymbol{x}_i, \boldsymbol{x}_j) = (\gamma \boldsymbol{x}_i \cdot \boldsymbol{x}_j + \beta)^d$
- Gaussian: $K(\boldsymbol{x}_i, \boldsymbol{x}_j) = e^{-\|\boldsymbol{x}_i - \boldsymbol{x}_j\|^2 / 2\sigma^2}$
- Sigmoid: $K(\boldsymbol{x}_i, \boldsymbol{x}_j) = \tanh(\gamma \boldsymbol{x}_i \cdot \boldsymbol{x}_j + \beta)$

However, a kernel may also be designed for a specific application as demonstrated by Zien et al. (2000). As shown above, most nonlinear kernels contain parameters such as d, β, γ and σ which may be selected by minimizing a measure of approximated generalization error (Section 2.1.1). All SVM presented in this work are based on the Gaussian kernel and the parameter σ was selected based on cross-validation. One advantage of the Gaussian kernel is its "flexibility": Large values of σ will produce SVM boundaries that closely resemble linear hyper-planes, while small values

produce "more localized" boundaries as shown in Figure 2.11. Virtually any data set becomes separable if a small enough σ is chosen. A more thorough discussion of kernel functions is provided by many textbooks such as Alpaydin (2004); Abe (2010); Schölkopf and Smola (2001). It should also be mentioned that the selection of kernel parameters quickly becomes non-trivial if there are more than one or two values to select. In this case, gradient-based optimization may be employed to minimize approximated generalization error as demonstrated by Chapelle et al. (2002) on a kernel with more than 100 parameters.

As can be seen from Equation 2.100, an SVM, using one of the kernels above, is a continuous analytical function $s(\boldsymbol{x})$ for which the gradients with respect to $\boldsymbol{x}$ are available analytically. This is relevant for applications in numerical optimization, because it greatly improves the efficiency of gradient-based algorithms.

2.4.3 Discussion

Support vector machines have become a very popular tool for classification problems and the hype around SVM has been compared to the popularity of neural networks which they often replace. Successful applications include, for example, spam filtering (Guzella and Caminhas (2009)), wind speed prediction (Mohandes et al. (2004)), classification of cancer tissue (Furey et al. (2000)), recognition of handwritten digits (Scholkopf et al. (1997)) and military vehicles (Karlsen et al. (2000)) and the prediction of bankruptcy (Min and Lee (2005)). Because of the large number of publications, many review articles summarize the research for specific applications such as chemistry (Li et al. (2009)), remote sensing (Mountrakis et al. (2011)), imaging biomarkers (Orr et al. (2012)) or pattern recognition (Byun and Lee (2002)).

Advantages The general popularity of SVM may be attributed to the following advantages: SVM routinely meet or exceed the prediction accuracy of other classification approaches such as neural networks and decision trees (Joachims (1998); Bennett and Campbell (2000); Scholkopf et al. (1997)). This is in part due to the flexibility of nonlinear kernels which allows for the reproduction of nonlinear, dis-

joint, boundaries. The SVM approach is well suited for high-dimensional training samples, such as imaging data and large numbers of samples, found in extensive databases. This often eliminates the need to carefully select features and training samples. The methodology is easy to use and provides repeatable, consistent results. Further simplification is due to the availability of sophisticated software packages, such as Chang and Lin (2011), that solve the optimization problem (Equation 2.127) and aid in the selection of kernel parameters.

Specifically for application in numerical design methods, SVM has the additional advantage that the classifying function is analytical, differentiable and very cheap to evaluate, which is important for gradient-based optimization and Monte-Carlo-based uncertainty quantification. The training process is relatively quick as well, thus enabling the use of adaptive sampling as described in Section 3.3.

Disadvantages It has been criticized that SVM do not "provide an explanation or a comprehensible justification for the knowledge they learn" (Barakat and Bradley (2010)). Lack of explanation can be a major obstacle to the acceptance of black-box systems, for example in medical diagnosis and considerable research has therefore been directed towards the extraction of rules from support vector machines as reviewed by Barakat and Bradley (2010).

Specifically for applications in numerical design methods, it has been noted that SVM may require large numbers of samples to achieve the accuracy required for numerical design methods (Basudhar et al. (2008)). This is a crucial issue if the training data is not provided by an existing database, but instead requires expensive simulations. To address this drawback, samples may be selected iteratively via adaptive sampling, where, based on a preliminary SVM boundary, additional training samples are selected to refine the accuracy of the classifier. This approach, termed explicit design space decomposition (EDSD) (Basudhar and Missoum (2010); Basudhar et al. (2012); Basudhar (2012)) was integrated into the algorithm proposed in Chapter 3, that further incorporates lower-fidelity simulation models into the learning process.

CHAPTER 3

MULTI-FIDELITY ALGORITHM

As stated in the introduction of this dissertation, design constraints characterized by high cost of evaluating the corresponding simulation models and binary or discontinuous responses present a difficult obstacle to numerical optimization. Because of the high cost of each evaluation, straight-forward optimization algorithms like genetic programming are not feasible and more efficient algorithms based on surrogate models and multi-fidelity methods are limited to continuous response models.

To address this challenge, this chapter proposes a multi-fidelity algorithm for the construction of SVM representations of failure boundaries. The failure boundary, also referred to as constraint boundary, is the boundary of the feasible region in the design space. SVMs (Section 2.4) are widely used in computer science and their advantages include the ability to approximate nonlinear, disjoint failure boundaries in n-dimensional parameter spaces. Training samples are chosen iteratively, minimizing simulation cost by carefully identifying points in the parameter space where more information is needed. A key advantage of the algorithm and its main improvement over recent work by Basudhar and Missoum (2010) is the incorporation of previous knowledge about the failure boundary to be approximated. That is, the algorithm takes advantage of low-fidelity results to reduce the number of evaluations of the high-fidelity model of interest.

This chapter is organized as follows: Section 3.1 analyzes and clarifies the assumptions and goals that comprise the problem statement on which the development of the algorithm is founded. The main concepts of the algorithm are outlined in Section 3.2, followed by Section 3.3 which provides the level of detail required for implementation. Finally, Section 3.4 applies the multi-fidelity algorithm to various test problems to study its efficiency and convergence characteristics.

3.1 Specific Problem Statement

The purpose of the proposed algorithm is to approximate efficiently the failure boundary of a given constraint model via SVM over a given design space. The design space D is a closed, compact vector space over the field of real numbers and is often given as a hyperrectangle:

$$D = \{\boldsymbol{x} \in \mathbb{R}^n | x_i \in [v_i, w_i]\} \tag{3.1}$$

with finite lower and upper bounds $\boldsymbol{v}$ and $\boldsymbol{w}$.

The constraint model M_H is a deterministic function that indicates the feasibility of any point in D:

$$M_H(\boldsymbol{x}) = \begin{cases} > 0 & \text{if } \boldsymbol{x} \text{ is infeasible} \\ \leq 0 & \text{if } \boldsymbol{x} \text{ is feasible} \end{cases} \tag{3.2}$$

A feasible point in the design space represents a set of design parameters for which the design satisfies all design requirements. In general, M_H represents not an analytical function, but either one or multiple simulation model(s) or experimental setup(s) where each evaluation is associated with large cost in terms of time and resources.

The failure boundary defined by M_H is approximately known, that is a function S_L is available that predicts with unknown accuracy the feasibility of any point in D. This prior knowledge about the sought-after constraint boundary is referred to as the low-fidelity boundary and given as an analytical expression or meta-model. For example such a low-fidelity boundary may be obtained by evaluating training samples via a low-fidelity constraint model M_L to build an SVM approximation of the low-fidelity constraint boundary. In any case, the low-fidelity boundary S_L predicts deterministically, with unknown accuracy, the classification of samples by the high-fidelity model:

$$S_L(\boldsymbol{x}) = \begin{cases} > 0 & \text{if } \boldsymbol{x} \text{ is predicted infeasible} \\ \leq 0 & \text{if } \boldsymbol{x} \text{ is predicted feasible} \end{cases} \tag{3.3}$$

Though evaluations of the low-fidelity model M_L may have consumed significant resources, evaluations of the resulting low-fidelity boundary are assumed to be very inexpensive as compared to the cost of evaluating a sample via the high-fidelity model.

Using the high-fidelity constraint model M_H and the low-fidelity boundary S_L, the algorithm is to create an SVM approximation S_H of the high-fidelity failure boundary which requires the selection and labeling of training samples, as well as the proper selection of Kernel parameters (Section 2.4). The main challenge stems from the high cost of high-fidelity evaluations which severely limits their number. To address this, the proposed multi-fidelity algorithm must carefully take into account the predictions of the low-fidelity boundary to obtain a set of labeled training samples that give an accurate approximation of the high-fidelity failure boundary at minimal overall cost.

To clarify the concept of accuracy a global error measure is defined to compare two classification models (C_1 and C_2) in D:

$$\epsilon(C_1, C_2) = \frac{\int_D L(C_1(\boldsymbol{x}), C_2(\boldsymbol{x}))\,\mathrm{d}\boldsymbol{x}}{\int_D \mathrm{d}\boldsymbol{x}} \tag{3.4}$$

with loss function L:

$$L(C_1, C_2) = \begin{cases} 1 & \text{if } C_1(\boldsymbol{x}) \cdot C_2(\boldsymbol{x}) < 0 \\ 0 & \text{otherwise} \end{cases} \tag{3.5}$$

Therefore $\epsilon(C_1, C_2)$ is the fraction of the design space that is classified inconsistently by the two models. Specifically the error of the SVM approximation S_H is given by:

$$\epsilon(S_H, M_H) = \frac{\int_D L(S_H(\boldsymbol{x}), M_H(\boldsymbol{x}))\,\mathrm{d}\boldsymbol{x}}{\int_D \mathrm{d}\boldsymbol{x}} \tag{3.6}$$

Likewise, $\epsilon(S_L, M_H)$ quantifies the error of the low-fidelity boundary and this measure will be used in this paragraph to formulate the expectation that the low-fidelity boundary provides useful predictions of the high-fidelity classification of samples. First the high-fidelity model is characterized by two measures, $\epsilon(1, M_H)$ and $\epsilon(-1, M_H)$, where $\epsilon(1, M_H)$ is the fraction of the design space D that is classified

as feasible and $\epsilon(-1, M_H)$ is the fraction of the design space classified as infeasible by the high-fidelity model M_H. They are of course related to each other by:

$$\epsilon(1, M_H) + \epsilon(-1, M_H) = 1 \tag{3.7}$$

Now, based on conditional probability the expected error of an arbitrary classifier S_R is:

$$E\left[\epsilon(S_R, M_H)\right] = \epsilon(1, S_R) \cdot \epsilon(-1, M_H) + \epsilon(-1, S_R) \cdot \epsilon(1, M_H) \tag{3.8}$$

To be useful the low-fidelity boundary S_L is expected to perform much better, specifically, it is assumed that:

$$\epsilon(S_L, M_H) \ll \min\left(\epsilon(1, M_H), \epsilon(-1, M_H)\right) \tag{3.9}$$

In addition, it is assumed that inaccurate predictions of the low-fidelity boundary are contained to a relatively small region close to the limit state $S_L(\boldsymbol{x}) = 0$. This neighborhood D_N, shown schematically in Figure 3.1, may be defined in terms of Euclidean distance in the design space as:

$$D_N(m) = \left\{\boldsymbol{x} \in D \middle| \left(\exists \boldsymbol{y} \in D \middle| \, \|\boldsymbol{x} - \boldsymbol{y}\| < m \wedge S_L(\boldsymbol{x}) \cdot S_H(\boldsymbol{y}) < 0\right)\right\} \tag{3.10}$$

with positive margin m. This subspace of D includes any point $\boldsymbol{x}$ for which there exists, within Euclidean distance m, another point $\boldsymbol{y}$ which is classified differently by S_L. In two dimensions, this is a strip of width $2m$ around the low-fidelity boundary as depicted in Figure 3.1. The relative complement of $D_N(m)$ in D is very relevant to this chapter and is referred to as $D_F(m)$:

$$D_F(m) = D \setminus D_N(m) \tag{3.11}$$

where the subscripts F and N stand for "far from" and "near to" the low-fidelity boundary S_L. Now the assumption that inaccurate predictions of the low-fidelity boundary are contained to a relatively small region close to the limit state $S_L(\boldsymbol{x}) = 0$ may be clarified as postulating that there exists a margin m such that S_L makes accurate predictions outside of $D_N(m)$ which has much smaller volume than D:

$$\exists m \in \mathbb{R}^+ \,|\, \epsilon(S_L, M_H) = 0 \text{ over } D_F(m) \wedge \int_{D_N(m)} \mathrm{d}\boldsymbol{x} \ll \int_D \mathrm{d}\boldsymbol{x} \tag{3.12}$$

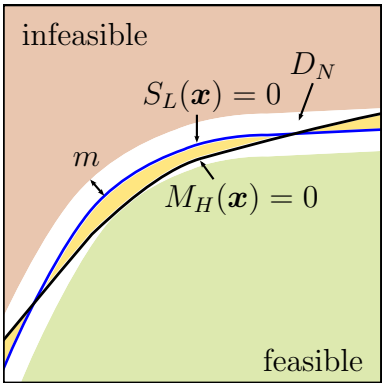

Figure 3.1: Schematic two-dimensional design space depicting the neighborhood D_N (white) that contains the regions of inaccuracy (yellow) of the low-fidelity boundary S_L

The smallest margin m such that $D_N(m)$ contains all inaccuracies is generally unknown, but is defined as:

$$m^* = \min \ m \text{ such that } \epsilon(S_L, M_H) = 0 \text{ over } D_F(m) \tag{3.13}$$

Together, Equations 3.9 and 3.12 comprise the assumptions for a low-fidelity boundary S_L that will provide useful information and therefore enable the reduction of expensive high-fidelity samples. However, the minimum margin m satisfying Equation 3.12 is generally not known and the algorithm developed in the following sections will have to account for this uncertainty.

The objective for the multi-fidelity algorithm may now be restated as follows: Assuming that Equations 3.9 and 3.12 hold, obtain labeled training samples and select appropriate kernel parameters, such that the SVM approximation S_H over the design space D has minimum error $\epsilon(S_H, M_H)$, while minimizing the number of high-fidelity evaluations.

3.2 Concept

The multi-fidelity algorithm described in detail in Section 3.3 is based on a few principles that are outlined in this section. First it should be clear from Equations 3.9 and 3.12 that without evaluating any high-fidelity samples, the low-fidelity bound-

ary S_L is the best available approximation of the high-fidelity classifier M_H and can only be improved via high-fidelity samples.

Previous research (Basudhar and Missoum (2010)) on building SVM approximations in the absence of a low-fidelity boundary has shown that training samples should be selected one-by-one such that previous evaluations guide the selection of the next sample. This process, referred to as adaptive sampling, by far outperformed static designs of experiments in terms of the evolution of the error measure (Equation 3.4) with respect to the number of evaluated samples. The same arguments hold in the multi-fidelity case, and therefore the proposed multi-fidelity algorithm also uses adaptive sampling to improve efficiency.

If the ideal margin m^* (Equation 3.13) was known, the algorithm for the selection and labeling of training samples could be rather straight forward: Since the actual failure boundary $M_H(\boldsymbol{x}) = 0$ is contained within $D_N(m^*)$, the rest of the design space may be populated with training samples evaluated by the low-fidelity boundary S_L at zero cost. Only in $D_N(m^*)$ are high-fidelity evaluations required to refine the SVM S_H via adaptive sampling. However, since for practical applications m^* is generally not known, the multi-fidelity algorithm must use a more sophisticated approach in which an initial guess for m^* is updated repeatedly based on the information gained from high-fidelity samples.

The concept for selection and labeling of training samples, shown in Figure 3.2, may be summarized as follows: Starting with an initial guess m_0, the far subspace $D_F(2m_0)$ (Equation 3.11) is populated with training samples which are labeled based on the low-fidelity boundary S_L. This forces the SVM approximation S_H to lie within $D_N(2m_0)$ in which high-fidelity samples are added adaptively to both refine the SVM and to check the assumption that $m_0 \geq m^*$. Violations of this assumption are detected by comparing the high-fidelity classification of samples to the corresponding low-fidelity classification of S_L. Care must be taken, that high-fidelity samples in $D_N(m_0)$ can neither confirm nor reject the assumption on m_0 since the low-fidelity and high-fidelity classification are not expected to match here. However, high-fidelity samples in $D_N(2m_0) \setminus D_N(m_0)$ disprove the assumption if the

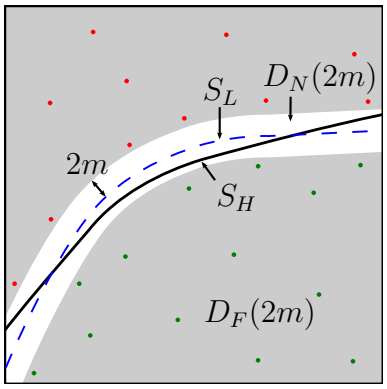

1. Constrain SVM

Constrain the SVM approximation S_H (solid black) to within $D_N(2m)$ (white) by adding training samples (dots) in $D_F(2m)$ (gray) which are evaluated by the low-fidelity boundary S_L (dashed blue)

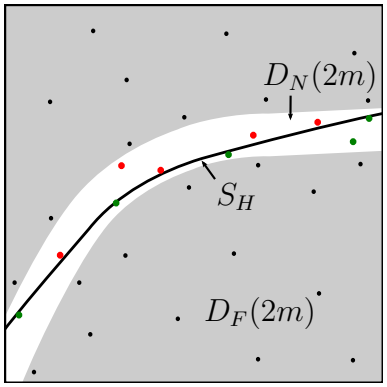

2. Adaptive Sampling

Refine the SVM S_H by adding a high-fidelity sample in $D_N(2m)$. The Figure shows the SVM after several iterations and multiple high-fidelity samples (colored dots). Low-fidelity samples are marked by small black dots.

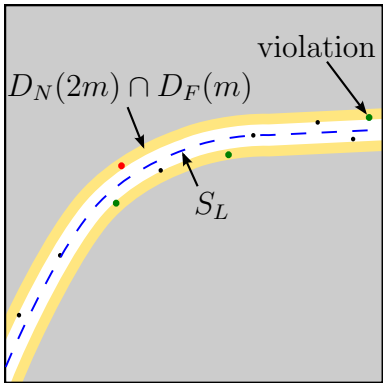

3. Margin Update

Using the available high-fidelity samples, check the assumption that S_L correctly classifies any sample in $D_F(m)$, that is: $S_L(\boldsymbol{x}) \cdot M_H(\boldsymbol{x}) > 0 \forall \boldsymbol{x} \in D_F(m)$. Only samples in $D_F(m) \cap D_N(2m)$ (yellow) may be used and are shown as colored dots. In the Figure, one sample violates the assumption, therefore the margin m must be increased.

Figure 3.2: Outline of the iterative multi-fidelity algorithm, where each iteration consists of three stages: Starting with an initial guess for margin m, proceed through steps 1 to 3 before returning to step 1 etc.

classifications do not match. In this case, a new margin $m_{n+1} > m_n$ is assumed, before the sampling process in continued. The three steps are repeated iteratively to achieve convergence of the SVM as shown in Figure 3.2.

As stated in Section 3.1, the purpose of the algorithm is not only to select and label training samples, but also to choose appropriate parameters for the SVM Kernel. Here, the algorithm takes a relatively conventional approach: The Kernel is the widely used Gaussian kernel and its parameters are selected based on cross-validation.

3.3 Algorithm

After previously outlining the main points of the multi-fidelity algorithm (Section 3.2), the current section provides the level of details required for implementation. As stated earlier, the goal is to construct an SVM (S_H) that accurately represents the failure boundary corresponding to the high-fidelity constraint model M_H. The SVM is constructed from training samples, each of which is classified as feasible or infeasible. Because of the associated cost, the algorithm seeks to use the high-fidelity model as little as possible and to classify some of the samples through a low-fidelity model instead. The algorithm uses adaptive sampling, which means that at each iteration one more sample is evaluated to refine the SVM.

Figure 3.3 provides an overview of the algorithm with references to the appropriate sections in this chapter. Splitting the design space D into several regions based on the distance to the low-fidelity boundary is a core concept of the algorithm and discussed in Section 3.3.1. Following, Section 3.3.2 provides some insights on the selection of the initial margin and approximating the low-fidelity boundary S_L. Section 3.3.3 explains how the SVM approximation S_H is constructed and constrained to the $D_N(2m)$ region around the low-fidelity boundary. The iterative selection of additional high-fidelity samples to refine the SVM within $D_N(2m)$ is treated at length in Section 3.3.4. Finally, Section 3.3.5 explains how the assumed margin m is checked after each new high-fidelity sample and updated as necessary.

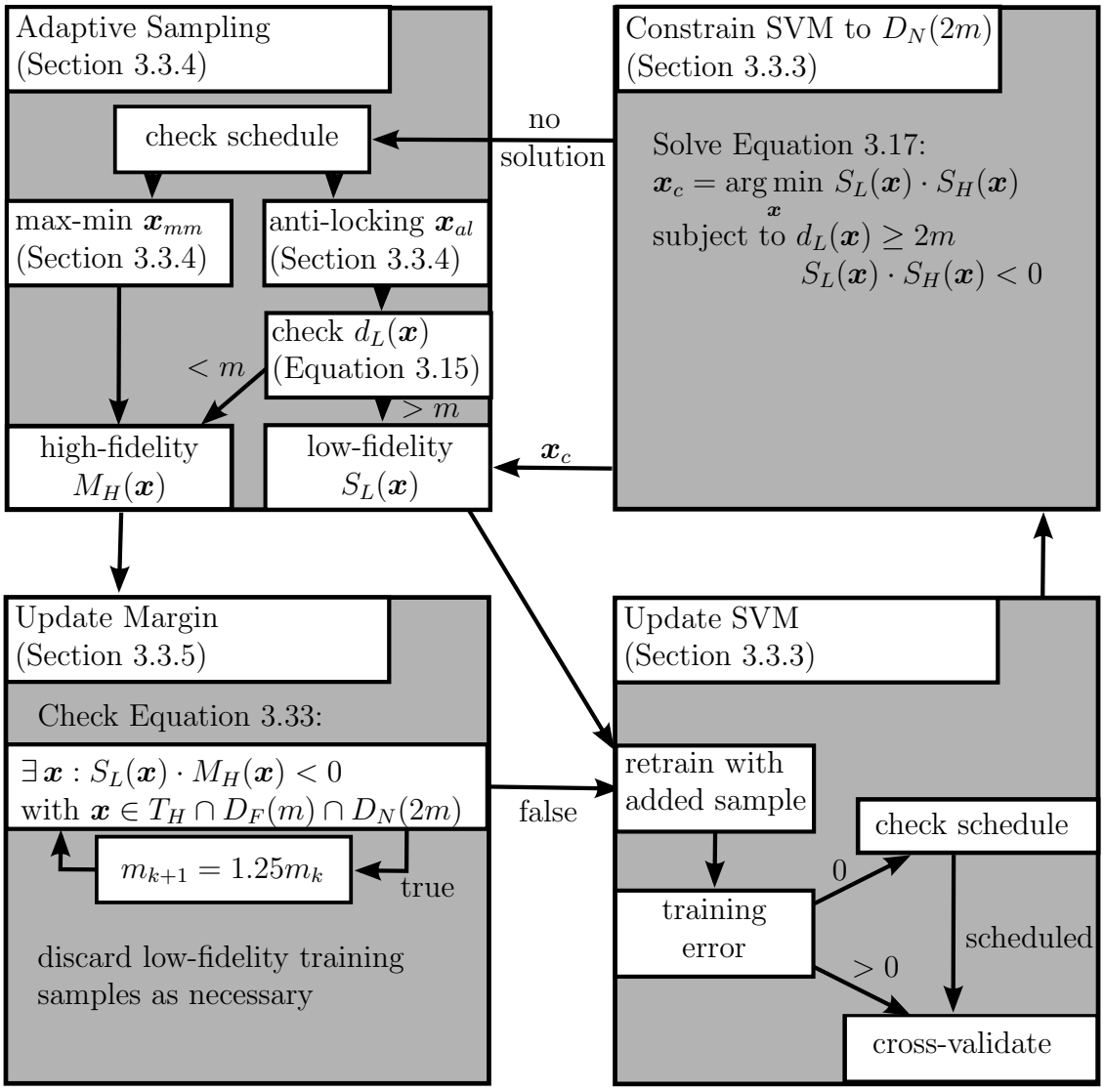

Figure 3.3: Detailed overview of the multi-fidelity algorithm with references to the corresponding sections and equations.

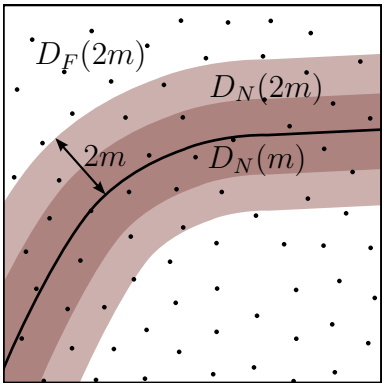

Figure 3.4: Design space regions

3.3.1 Regions of the Design Space

In Section 3.2 the design space is split up into three distinct regions that are associated with different expectations of the accuracy of the low-fidelity boundary S_F. Their definition is based on the neighborhood $D_N(m)$ of the low-fidelity boundary as defined in Equation 3.10 and repeated here for readability:

$$D_N(m) = \{\boldsymbol{x} \in D | \, (\exists \boldsymbol{y} \in D | \, \|\boldsymbol{x} - \boldsymbol{y}\| < m \wedge S_L(\boldsymbol{x}) \cdot S_H(\boldsymbol{y}) < 0)\} \tag{3.14}$$

As stated earlier, this neighborhood includes any point of the design space D that is within Euclidean distance m of the low-fidelity boundary $S_L(\boldsymbol{x}) = 0$. Logically, its relative complement in D, that is $D_F(m) = D \setminus D_N(m)$, is the set of points that are further than m from the low-fidelity boundary. The algorithm operates on the premise that any sample in $D_F(m)$ is classified correctly by the low-fidelity boundary S_L whose evaluation cost is negligible. In order to exploit, but also verify this assumption the design space is split into three regions, which are explained using a 2-dimensional schematic:

$D_F(2m)$ These far sample are always evaluated through the low-fidelity model.

$D_N(m)$ These close samples are always evaluated through the high-fidelity model. The low-fidelity model is not expected to classify these samples correctly.

$D_N(2m) \cap D_F(m)$ Though we expect the low-fidelity model to be accurate in this range, we still use the high-fidelity model. This allows us to check the margin.

If samples in this region are misclassified by the low-fidelity model the margin is increased.

Clearly, the algorithm must be able to determine which region a point $\boldsymbol{x}$ belongs to, which requires the Euclidean distance to the low-fidelity boundary. This distance $d_L(\boldsymbol{x})$ may be obtained by solving the following optimization problem which seeks the closest other point $\boldsymbol{y} \in D$ that is classified differently by the low-fidelity boundary S_L:

$$d_L(\boldsymbol{x}) = \min_{\boldsymbol{y}} \|\boldsymbol{x} - \boldsymbol{y}\| \text{ subject to: } S_L(\boldsymbol{x}) \cdot S_L(\boldsymbol{y}) < 0 \tag{3.15}$$

Solving this optimization problem efficiently is non-trivial due to the likelihood of multiple local optima. The current implementation uses a Monte-Carlo search to find a good initial guess which is then refined via gradient-based optimization (SQP) with analytical gradients. As detailed in the following Sections, the multi-fidelity algorithm may require this distance for large numbers of points, which can be addressed by building a Kriging model of $d_L(\boldsymbol{x})$. This is efficient because the required accuracy is not very high and the low-fidelity boundary S_L is fixed, which means the Kriging model must be built only once. The practical implementation of the algorithm uses d_L to determine which region a point $\boldsymbol{x}$ belongs to via the following equivalences:

$$\begin{aligned} d_L(\boldsymbol{x}) < m &\equiv \boldsymbol{x} \in D_N(m) \\ d_L(\boldsymbol{x}) \geq 2m &\equiv \boldsymbol{x} \in D_F(2m) \\ m < d_L(\boldsymbol{x}) < 2m &\equiv \boldsymbol{x} \in D_N(2m) \cap D_F(m) \end{aligned} \tag{3.16}$$

3.3.2 Initial Setup

Starting the multi-fidelity algorithm requires a high-fidelity constraint model M_H, a low-fidelity boundary S_L and an initial guess for the margin m. While M_H is considered a given, the other two invite further explanaition. First, however, to avoid any confusion, the distinction between the 4 classifiers introduced in Section 3.1 is summarized:

M_H is a high-fidelity model that classifies designs as feasible or infeasible. Each evaluation is associated with such large cost that the number of evaluations is the appropriate measure for the efficiency of the algorithm.

S_H is the SVM approximation of the failure boundary defined by M_H. Obtaining a sufficiently accurate S_H is the goal of the proposed multi-fidelity algorithm.

M_L is a low-fidelity model that predicts with some accuracy the high-fidelity classification of samples. Specifically M_L satisfies Equations 3.9 and 3.12. The cost of each evaluation of M_L is significantly lower than the cost of evaluating M_H.

S_L also satisfies the Conditions 3.9 and 3.12, but the cost of each evaluation is negligible.

If, for example, M_L is an analytical model, S_L and M_L may be identical. However if M_L is a simulation model with considerable evaluation cost, then S_L will have to be a meta-model with insignificant evaluation cost or an SVM. This can be achieved, for example, by selecting uniformly distributed training samples (Section 2.1.2) and classifying each sample as feasible or infeasible based on the low-fidelity model M_L. This training data is then used to build the SVM S_L as explained in Section 2.4. This is the only step in the algorithm where the low-fidelity model is used, that is for the rest of the algorithm only the low-fidelity SVM S_L is employed to obtain low-fidelity classifications of points in D.

The initial margin reflects an assumption about the accuracy of the low-fidelity model. The ideal value m^* is just large enough so that $D_N(m^*)$ contains all inaccuracies of S_L (Equation 3.13). However, in practical applications this value is not available and one must resort to an initial guess which is increased by the algorithm when high-fidelity samples prove the current margin to be too small. Selecting an initial margin that is much too large reduces the efficiency of the algorithm, because it will not take advantage of the low-fidelity boundary as much as possible, leading to a higher number of high-fidelity samples. On the other hand, selecting an initial margin that is much too small, forces the first few high-fidelity samples to be very

close to the low-fidelity boundary, which may be a waste as well. In general, one should try to select an initial margin that is a bit smaller than the actual ideal margin m^* to get the maximum benefit. However, convergence of the algorithm is insured even if the initial guess for the margin is very off and the penalty in terms of efficiency is very reasonable as demonstrated in Section 3.4.

3.3.3 Constraining the SVM to $D_N(2m)$

After choosing the initial margin m_0 and obtaining the low-fidelity boundary (S_L) the first high-fidelity SVM can be build. In general the high-fidelity SVM uses both low- and high-fidelity training samples, but the initial high-fidelity SVM (S_H) is obtained from low-fidelity samples only: A set of samples is selected through a design of experiments (Section 2.1.2) and any of these samples that are close to the low-fidelity boundary ($d_L(\boldsymbol{x}) < 2m$) are discarded. The remaining samples are classified by S_L and used to train the first high-fidelity SVM S_H.

S_H is always expected to be consistent with S_L for any point in $D_F(2m)$ as shown in Figure 3.5a, but depending on the number of initial training samples, there may still be unacceptable inconsistencies between the high-fidelity SVM and the low-fidelity boundary. Figure 3.5b shows such regions of the design space that are far from the low-fidelity boundary, but classified inconsistently by the high-fidelity SVM. Though it is possible to ensure consistency by simply choosing a very large design of experiments (DOE), this brute force approach is not recommended especially for higher dimensional problems where it may require an overwhelming number of points. Instead, the algorithm starts with a reasonably sized DOE and then adds targeted low-fidelity samples in regions of inconsistency. Specifically, these consistency samples are selected one-by-one from $D_F(2m)$ by solving the following optimization problem:

$$\begin{aligned} \boldsymbol{x}_c = \arg\min_{\boldsymbol{x}} \; & S_L(\boldsymbol{x}) \cdot S_H(\boldsymbol{x}) \\ \text{subject to } & d_L(\boldsymbol{x}) \geq 2m \wedge S_L(\boldsymbol{x}) \cdot S_H(\boldsymbol{x}) \leq 0 \end{aligned} \tag{3.17}$$

This global optimization problem may not have a solution, in which case the

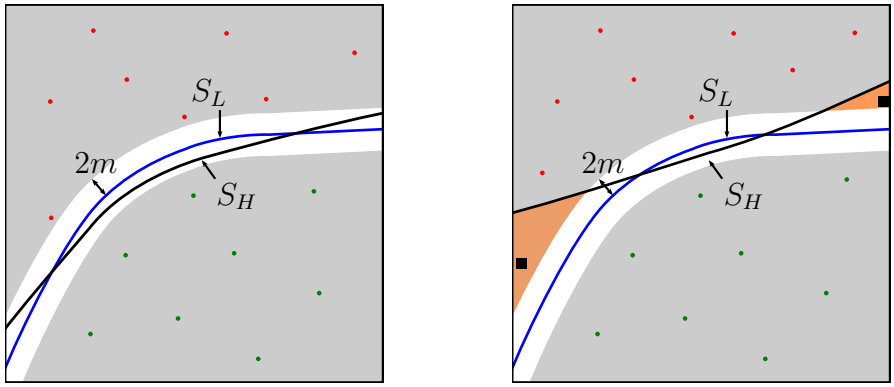

(a) acceptable inconsistencies (b) inacceptable inconsistencies

Figure 3.5: Constraining the SVM: the low-fidelity boundary (blue) is used to classify the initial training samples (green and red) to train the first high-fidelity SVM (black). Though we expect far regions to be classified consistently by the initial high-fidelity SVM (a), such inconsistencies (orange) may occur (b). They are removed by adding consistency training samples (black squares), obtained from Equation 3.17.

two boundaries are consistent and no additional low-fidelity samples are necessary. Otherwise $\boldsymbol{x}_c$ is added as a low-fidelity training sample and the high-fidelity SVM is updated before the next attempt to solve Equation 3.17.

The main difficultly of solving this optimization problem is the possibility of local optima. In order to minimize the chance of missing small inconsistent regions, the current implementation employs a combination of Monte-Carlo sampling and gradient-based optimization to seek solutions of Equation 3.17. Figure 3.5b presents two examples of consistency samples obtained by this approach in a two-dimensional test problem discussed in Section 3.4.

In summary, lack of training samples in regions far from the low-fidelity boundary can cause these regions of $D_F(2m)$ to be misclassified by the high-fidelity SVM. Adding low-fidelity training samples in $D_N(2m)$ has insignificant associated model evaluation cost, since the samples will be evaluated by the low-fidelity boundary S_L, therefore consistency samples eliminate these inaccuracies of the high-fidelity SVM at negligible cost.

Construction of Support Vector Machine

In addition to a set of classified training samples, constructing the SVM also requires the selection of a Kernel function and corresponding Kernel parameters as discussed in Section 2.4. The current algorithm uses the general-purpose Gaussian kernel:

$$K(\boldsymbol{x}_i, \boldsymbol{x}_j) = e^{-\|\boldsymbol{x}_i - \boldsymbol{x}_j\|^2/2\sigma^2} \tag{3.18}$$

with parameter σ to obtain a nonlinear SVM boundary. σ is selected from a discrete set of logarithmically spaced values to minimize the cross-validation error (Section 2.1.1). Since the multi-fidelity algorithm is geared towards deterministic constraint models, the training samples are expected to be separable and no training error is permitted (Section 2.4.2). This is achieved by ignoring all values of σ that result in non-zero training error, regardless of the corresponding cross-validation error.

3.3.4 Adaptive Sampling

After the high-fidelity SVM has been constrained to the $D_N(2m)$ neighborhood of the low-fidelity boundary S_L as described in the previous Section 3.3.3, the next step is to add a high-fidelity sample to refine S_H in $D_N(2m)$. The current section will first discuss the selection of these samples in general terms before presenting the finer details in Sections 3.3.4 and 3.3.4. The concept of adaptive sampling is to use the current SVM and its distribution of training samples to predict where additional information in the form of an evaluated sample will be most helpful to improve the SVM.

The selection of these samples as part of the multi-fidelity algorithm is based on two algorithms developed by Anirban Basudhar as part of his dissertation research (Basudhar (2012)). Specifically the max-min samples described below are identical to the primary samples proposed in Basudhar and Missoum (2010). Likewise, the anti-locking samples (Section 3.3.4) are similar to, and serve the same purpose as the secondary samples proposed in Basudhar and Missoum (2010).

The underlying idea for the max-min samples is that adding a sample right on the SVM boundary $S_H(\boldsymbol{x}) = 0$ is guaranteed to modify the SVM. Further, the

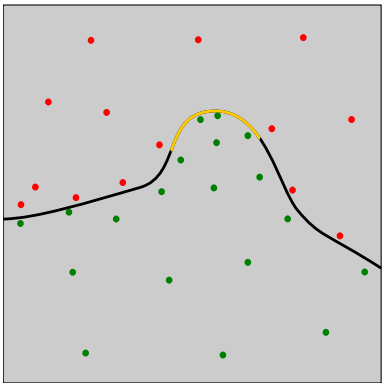

Figure 3.6: Schematic representation of an unevenly supported SVM in two dimensions. The section of the SVM (line) highlighted in yellow is unevenly supported. Lack of near-by infeasible samples (red) calls the local accuracy of the SVM into question.

change is likely to be largest if the sample is added in a region of the boundary that is relatively sparsely populated with samples as shown schematically in Figure 3.7a. Using max-min samples is generally very efficient, quickly leading to an SVM boundary that is tightly constrained by evenly distributed training samples on both sides (feasible and infeasible).

However, it has been observed that max-min samples may sometimes cause only very small changes in the SVM, leading to an approximated boundary that is unevenly supported. That is, there are regions where the SVM is tightly restricted on one side (feasible or infeasible) by training samples, but training samples on the other side are relatively far as shown schematically in Figure 3.6. Though adding more and more max-min samples will eventually resolve this situation, it is more efficient to use a sample that is placed off the boundary, on the less populated side. Such an anti-locking sample will either cause a more significant change in the SMV boundary or confirm the current boundary by constraining its location in a more balanced way as shown in Figure 3.7b

As proposed by Basudhar and Missoum (2010), the multi-fidelity algorithm uses a ratio of 2:1 between max-min samples and anti-locking samples, that is any two iterations, each adding a max-min sample, will be following by one iteration adding

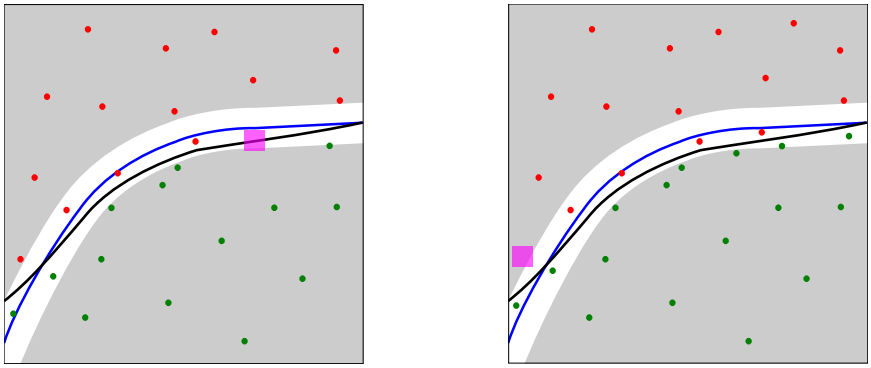

(a) max-min sample (b) anti-locking sample

Figure 3.7: (a) and (b) schematically show the selection of max-min and anti-locking samples, respectively (magenta squares). The high-fidelity SVM is shown in black, while the low-fidelity boundary is denoted by a blue line. Training samples are marked by red and green dots.

an anti-locking sample. After introducing the main ideas of adaptive sampling, the following two sections will provide the level of detail required for implementation.

Max-Min Sample

The definition of max-min samples is identical to the primary samples proposed by Basudhar and Missoum (2010), except for a small modification to account for the presence of both low- and high-fidelity samples. A max-min sample $\boldsymbol{x}_{mm}$ is a point on the SVM boundary at maximum distance to the closest training sample. For any point $\boldsymbol{x}$ on the SVM, the closest training sample $\boldsymbol{y}_c$ and its distance to $\boldsymbol{x}$ are defined as:

$$\boldsymbol{y}_c(\boldsymbol{x}, T) = \arg\min_{\boldsymbol{y}} \|\boldsymbol{x} - \boldsymbol{y}\| \quad \text{such that } \boldsymbol{y} \in T \tag{3.19}$$

$$d(\boldsymbol{x}, T) = \|\boldsymbol{x} - \boldsymbol{y}_c(\boldsymbol{x}, T)\| \tag{3.20}$$

with T being the the set of training samples. Based on this distance measure, the max-min sample is defined as the solution of an optimization problem:

$$\boldsymbol{x}_{mm} = \arg\max_{\boldsymbol{x}} d(\boldsymbol{x}, T) \text{ such that } S_H(\boldsymbol{x}) = 0 \tag{3.21}$$

However, in the multi-fidelity case, most training samples are low-fidelity and it is undesirable to let the distribution of low-fidelity samples in $D_F(2m)$ dictate the selection of high-fidelity samples in $D_N(2m)$. This is easily resolved by only considering high-fidelity training samples T_H in the definition of $\boldsymbol{x}_{mm}$:

$$\boldsymbol{x}_{mm} = \arg\max_{\boldsymbol{x}} d(\boldsymbol{x}, T_H) \text{ such that } S_H(\boldsymbol{x}) = 0 \tag{3.22}$$

which leads to max-min samples that are more evenly distributed along the SVM boundary. At the first iteration T_H may of course be empty, in which case it is replaced by the set of all training samples T.

Implementation The main difficulty of solving Equation 3.27 lies in the possibility of multiple local optima, especially as the number of training samples increases. In order to use gradient-based solvers in the implementation, Basudhar and Missoum (2010) proposed an equivalent formulation of the optimization problem in order to eliminate the non-differentiable objective function:

$$\begin{aligned} \boldsymbol{x}_{mm} = \quad & \arg\max_{\boldsymbol{x},z} \quad z \\ & \text{such that} \quad d(\boldsymbol{x}, T_H) \geq z \\ & \qquad\qquad\; S_H(\boldsymbol{x}) = 0 \end{aligned} \tag{3.23}$$

where z acts as a lower limit for the distance to the closest other high-fidelity training sample.

However, the number of optimization constraints in Equation 3.23 equals the number of training samples of the SVM and this may slow down the solver if this number is large. To address this, an alternative formulation based on the p-norm is proposed. For a unique set of positive numbers v_k, the p-norm approximates the maximum as:

$$\max\{v_1, \ldots, v_m\} \approx \|\boldsymbol{v}\|_p = \left(\sum_{k=1}^{m} v_k^p\right)^{1/p} \tag{3.24}$$

with exponent $p \gg 1$. Similarly the smallest number in the set is approximated as:

$$\min\{v_1, \ldots, v_m\} \approx \|\boldsymbol{v}\|_{-p} = \left(\sum_{k=1}^{m} v_k^{-p}\right)^{-1/p} \tag{3.25}$$

Based on Equation 3.25, the distance of point $\boldsymbol{x}$ to the closest high-fidelity training sample is approximated as:

$$d(\boldsymbol{x}, T) = \|\{\|\boldsymbol{x} - \boldsymbol{y}\| : \boldsymbol{y} \in T\}\|_{-p} \tag{3.26}$$

Using a high exponent, such as $p = 50$, provides an objective function approximation that is both accurate and differentiable, and finally the implementation of the multi-fidelity algorithm uses the following formulation to replace Equation 3.22:

$$\begin{aligned} \boldsymbol{x}_{mm} = \ & \arg\max_{\boldsymbol{x}} \ \|\{\|\boldsymbol{x} - \boldsymbol{y}\| : \boldsymbol{y} \in T_H\}\|_{-50} \\ & \text{such that } S_H(\boldsymbol{x}) = 0 \end{aligned} \tag{3.27}$$

which features a single differentiable objective function and constraint.

Anti-Locking Sample

Though max-min samples always change the SVM, the change may be very small, which is referred to as locking. The anti-locking samples (Figure 3.7b) are offset from the boundary towards the regions of fewer samples, therefore evaluating an anti-locking sample either leads to a more balanced distribution of samples on both sides or to a significant change in the SVM boundary. The definition of anti-locking samples presented here is based on the algorithm proposed by Basudhar and Missoum (2010), with few modifications.

Anti-locking samples are placed in regions of the design space where the boundary is very constrained by one class of samples (feasible or infeasible), but not the other. This unbalance of data may be formalized based on the sets of feasible and infeasible training samples, which are denoted by T^- and T^+ respectively. Obviously, their intersection is empty and their union is the set of all training samples: $T = T^- \cup T^+$. Now, referring back to Equation 3.20, for any point on the SVM boundary, $d(\boldsymbol{x}, T_H^-)$ and $d(\boldsymbol{x}, T_H^+)$ denote the distance to the closest feasible and infeasible high-fidelity training sample, respectively. This leads to the definition of the point of greatest unbalance $\boldsymbol{x}_u$ on the SVM boundary, where the absolute difference

in the distances is greatest:

$$\boldsymbol{x}_u = \arg\max_{\boldsymbol{x}} \ \left(d(\boldsymbol{x}, T_H^-) - d(\boldsymbol{x}, T_H^+)\right)^2 \text{ such that } S_H(\boldsymbol{x}) = 0 \tag{3.28}$$

After obtaining this center point, the anti-locking sample $\boldsymbol{x}_{al}$ is sought within a hypersphere of radius R:

$$R = \frac{1}{4}\left|d(\boldsymbol{x}_u, T_H^-) - d(\boldsymbol{x}_u, T_H^+)\right| \tag{3.29}$$

The anti-locking sample itself is obtained by maximizing the SVM value, while restricting the solution to be of opposite class as the closest training sample $\boldsymbol{y}_c(\boldsymbol{x}, T)$ (Equation 3.19):

$$\begin{aligned} \boldsymbol{x}_{al} = \arg\max_{\boldsymbol{x}} \ S_H^2(\boldsymbol{x}) \ \text{ such that } \ & S_H(\boldsymbol{x}) \cdot S_H(\boldsymbol{y}_c(\boldsymbol{x}, T)) \leq 0 \\ & \|\boldsymbol{x} - \boldsymbol{x}_u\|^2 \leq R^2 \end{aligned} \tag{3.30}$$

The objective function and the constraint on the SVM value maximize the impact of the anti-locking sample if its evaluation via the high-fidelity model moves the SVM boundary. The hypersphere constraint ensures that the anti-locking sample will be relatively close to the boundary and therefore eliminate unbalance of data if the sample evaluation via the high-fidelity model does not change the SVM boundary.

Implementation As with the max-min samples (Section 3.3.4) the main difficulty of solving Equation 3.28 lies in the possibility of multiple local optima, especially as the number of training samples increases. In order to use efficient gradient-based solvers in the implementation, Equation 3.28 is replaced by an approximate, differentiable formulation based on the p-norm (Equation 3.24). The derivation follows the same line of thought as in Section 3.3.4: both $d(\boldsymbol{x}_u, T^-)$ and $d(\boldsymbol{x}_u, T^+)$ are replaced by p-norms with large exponent $p = 50$. Consequently, the implementation of the multi-fidelity algorithm uses the following formulation with single differentiable objective function and constraint to replace Equation 3.28:

$$\begin{aligned} \boldsymbol{x}_u = \ & \arg\max_{\boldsymbol{x}} \ \left(\left\|\left\{\|\boldsymbol{x} - \boldsymbol{y}\| : \boldsymbol{y} \in T_H^-\right\}\right\|_{-50} - \left\|\left\{\|\boldsymbol{x} - \boldsymbol{y}\| : \boldsymbol{y} \in T_H^+\right\}\right\|_{-50}\right)^2 \\ & \text{such that } S_H(\boldsymbol{x}) = 0 \end{aligned} \tag{3.31}$$

which features a single differentiable objective function and constraint. After solving Equation 3.31, the actual anti-locking sample is obtained easily from Equation 3.30, which features a single objective function with two constraints, whose gradients are readily available analytically.

3.3.5 Margin Update

During this update step the new sample is classified and added as a training sample for the high-fidelity SVM S_H. In addition, the margin is increased if necessary, which includes removal of any low-fidelity training samples that now lie in the new $D_N(2m)$. As stated in Section 3.2, the multi-fidelity algorithm operates on the assumption that any point in $D_F(m)$ is correctly classified by the low-fidelity boundary S_L:

$$S_L(\boldsymbol{x}) \cdot M_H(\boldsymbol{x}) > 0 \; \forall \; \boldsymbol{x} \in D_F(m) \tag{3.32}$$

However, in order to be able to check this assumption, the algorithm only relies on S_L for sample evaluations in $D_F(2m)$. This precaution leads to high-fidelity samples in the intersection $D_F(m) \cap D_N(2m)$ which may disprove Assumption 3.32. Specifically, the current margin m is too small if:

$$\exists\, \boldsymbol{x} : S_L(\boldsymbol{x}) \cdot M_H(\boldsymbol{x}) < 0 \text{ such that } \boldsymbol{x} \in T_H \cap D_F(m) \cap D_N(2m) \tag{3.33}$$

where T_H is the set of high-fidelity training samples defined in Section 3.3.4. If Condition 3.33 is valid for the current margin m_k, then the margin is increased to $m_{k+1} > m_k$ at which Equation 3.33 evaluates as false. Based on the new margin, it may be necessary to eliminate some of the low-fidelity training samples employed to constrain the high-fidelity SVM (Section 3.3.3). Specifically, any low-fidelity samples within $D_N(2m_{k+1})$ must be discarded, leading to the updated set of training samples:

$$T_{k+1} = T_H \cup T_L \setminus D_N(2m_{k+1}) \tag{3.34}$$

After this last step of the current iteration, the multi-fidelity algorithm begins the next iteration by constraining the high-fidelity SVM to the new neighborhood of S_L as described in Section 3.3.3.

3.4 Analytical Test Problems

In this section the multi-fidelity algorithm is applied to several analytical test problems to study its characteristics. The first example (Section 3.4) is a two-dimensional problem that demonstrates quantitatively and visually how the algorithm converges to the failure boundary, and explains the benefit of the low-fidelity boundary via the distribution of samples. The second, three-dimensional problem is based on the natural frequencies of a simply supported plate and demonstrates the influence of varying the accuracy of the low-fidelity boundary and the initial margin (Section 3.4). Finally, an n-dimensional spherical failure boundary shows the performance of the algorithm in higher-dimensional problems (Section 3.4).

Two-dimensional Sine Problem

This first problem is defined in a two-dimensional normalized design space and the high-fidelity model classifies samples according to:

$$M_H(\boldsymbol{x}) = 0.2\ \sin(10x_1) - 0.5 - x_2 \tag{3.35}$$

The low-fidelity model uses a similar function:

$$M_L(\boldsymbol{x}) = 0.25\ \sin(10x_1) - 0.45 - x_2 \tag{3.36}$$

and Figure 3.8 shows the failure boundaries corresponding to both models. For the sake of simplicity, M_L is used directly as the low-fidelity boundary: $S_L = M_L$. The ideal margin m^* (Equation 3.13) is the greatest distance of one point on the high-fidelity boundary to the closest point on the low-fidelity boundary. Based on Equations 3.35 and 3.36 it is exactly 0.1.

To test the algorithm, it is applied to this problem with two different initial margins: Using $m_0 = 0.01$ tests the algorithm's ability to iteratively update the margin and still take advantage of the low-fidelity boundary, and using $m_0 = 2$ means that $D_N(m_0)$ encompasses the whole design space and the low-fidelity boundary is ignored. Therefore $m_0 = 2$ provides a reference solution to quantify the advantage

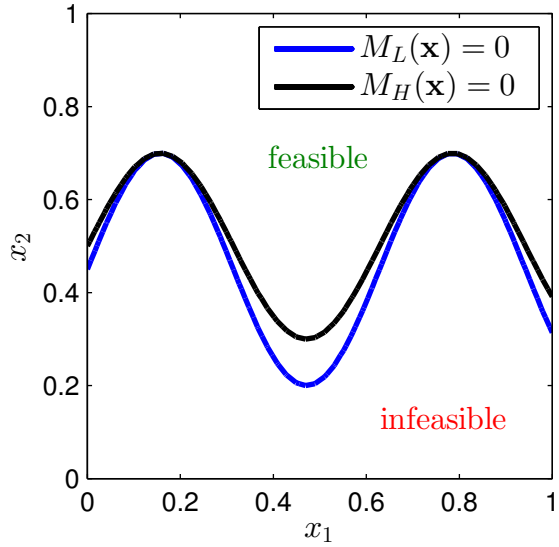

Figure 3.8: Low-fidelity (blue) and high-fidelity (black) failure boundary

obtained from the low-fidelity boundary. In this case, no low-fidelity samples are available to construct the initial SVM, and the algorithm starts with the evaluation of 10 uniformly distributed high-fidelity samples selected by a design of experiments (Section 2.1.2). Figure 3.9 presents various iterations of the algorithm with $m_0 = 0.01$ and shows clearly how the initial high-fidelity SVM S_H deviates from the low-fidelity boundary S_L as more and more high-fidelity samples are evaluated, and the margin is increased iteratively.

The error measure $\epsilon(S_H, M_H)$ (Equation 3.6) quantifies the error of the S_H approximation of the failure boundary and is equivalent to the fraction of the design space volume misclassified by S_H. In the general case, it cannot be evaluated directly, but may be approximated numerically, for example via Monte-Carlo sampling:

$$\epsilon = \frac{1}{N} \sum_{i=1}^{N} L(S_H(x_i), M_H(x_i)) \tag{3.37}$$

where L is the loss function defined in Equation 3.5 and N is the number of samples, each of which is evaluated via the current SVM S_H and the actual model M_H. For these analytical test problems we can afford to evaluate a large number of samples, therefore $N = 100000$ is chosen to eliminate any doubt in the accuracy of

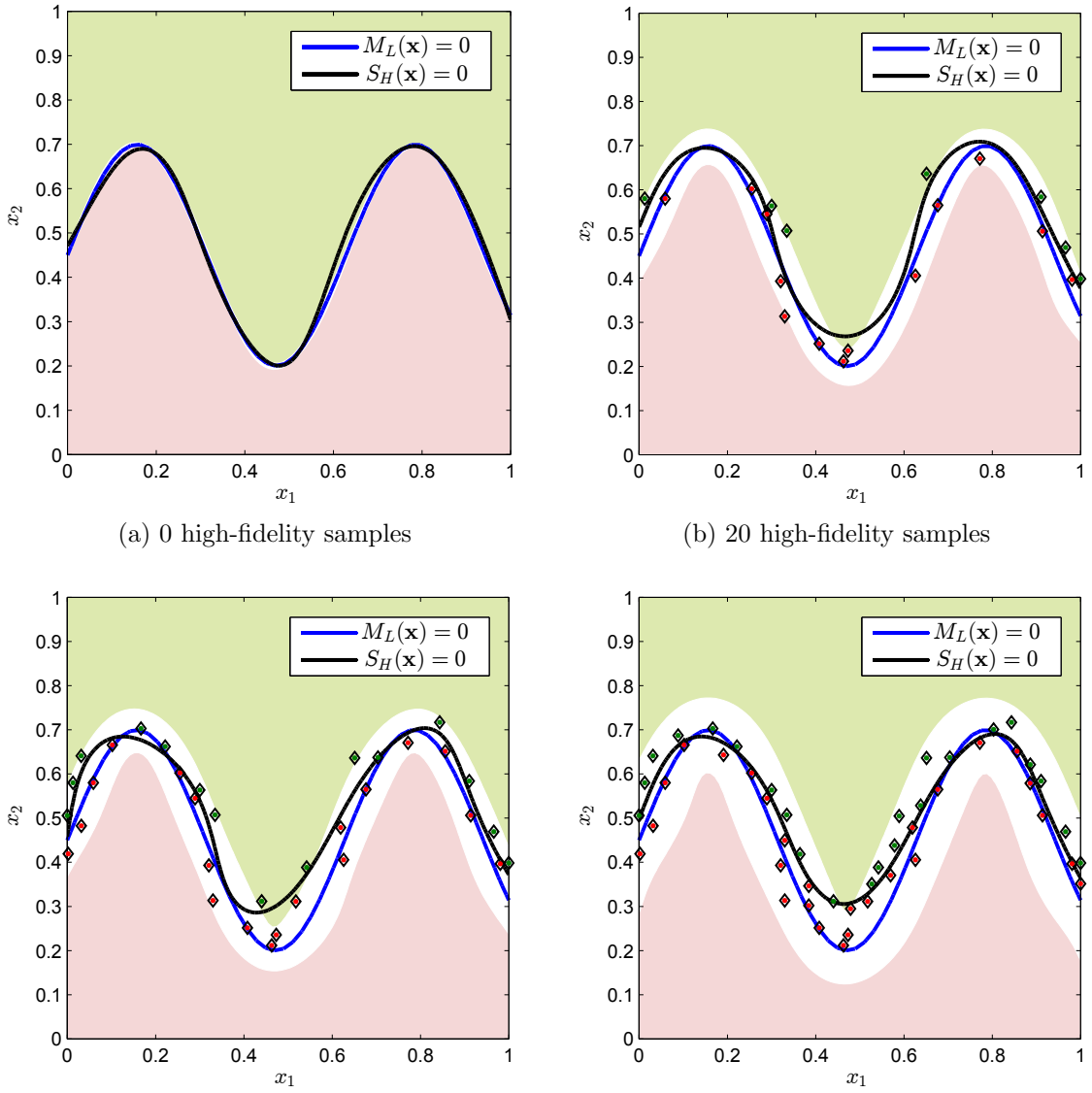

(a) 0 high-fidelity samples

(b) 20 high-fidelity samples

(c) 35 high-fidelity samples

(d) 50 high-fidelity samples

Figure 3.9: Various iterations of the algorithm with $m_0 = 0.01$: The high-fidelity SVM S_H (black) is forced away from the low-fidelity boundary S_L (blue) by high-fidelity samples (diamonds) and D_N (white) grows as the margin m is corrected iteratively.

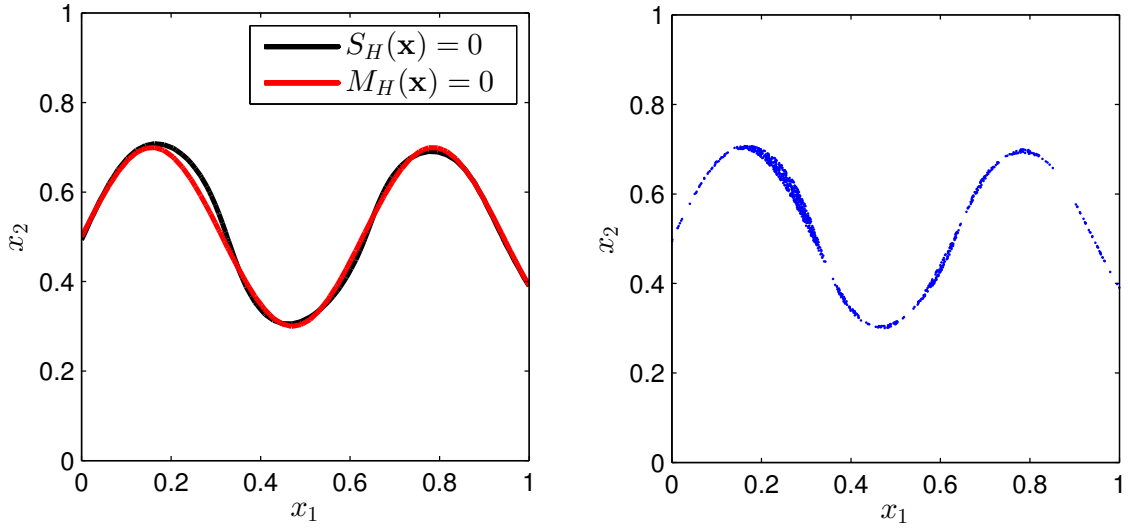

(a) M_H versus S_H (b) Monte-Carlo samples

Figure 3.10: Example of the error measure $\epsilon(S_H, M_H)$, evaluated via Monte-Carlo samples. In this two-dimentional case, $\epsilon \approx 0.01$ is the area between the two boundaries, approximated by the fraction of Monte-Carlo samples in this area (blue dots). Other MC samples are not shown.

$\epsilon(S_H, M_H)$. Specifically the 95% confidence interval in terms of percentage error of the error measure obtained via Monte-Carlo sampling may be estimated as (Haldar and Mahadevan (2000)):

$$e_{\%} = \sqrt{\frac{1 - \epsilon_T}{N \cdot \epsilon_T}} \cdot 200\%. \tag{3.38}$$

where ϵ_T is the true value of error measure $\epsilon(S_H, M_H)$. For example, assuming that the true error is 0.001, the error measure approximated via 100000 Monte-Carlo samples will be within 0.001 ± 0.0002 with 95% probability. Figure 3.10 shows an example of the Monte-Carlo approach to estimate error measure ϵ. Clearly, the number of samples is sufficient to reproduce the size of the misclassified fraction of the design space.

Calculating the error measure ϵ after each high-fidelity sample evaluation quantifies the convergence of the algorithm. Figure 3.11 shows this evolution for both cases of initial margin, where $m_0 = 0.01$ takes advantage of the low-fidelity boundary S_L and $m_0 = 2$ is so large that S_L is completely ignored. Even though $m_0 = 0.01$ is

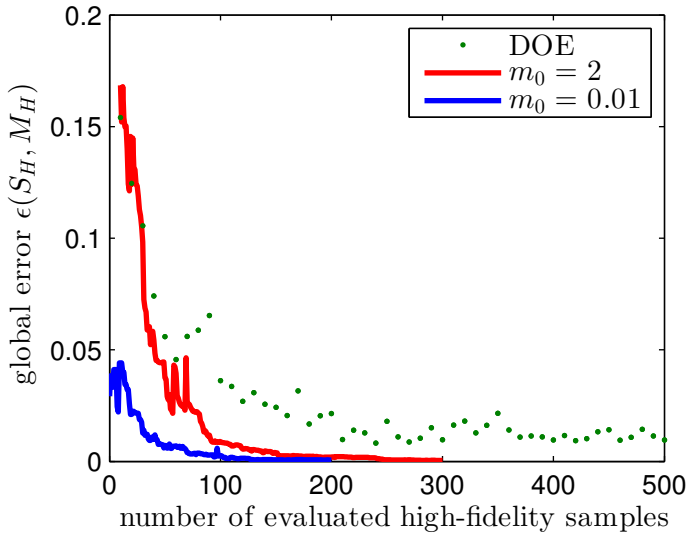

Figure 3.11: Evolution of the error $\epsilon(S_H, M_H)$ with respect to the number of evaluated high-fidelity samples. Taking advantage of the low-fidelity boundary ($m_0 = 0.01$) reduced the required evaluations as compared to ignoring the low-fidelity boundary ($m_0 = 2$). Using uniformly distributed samples (Section 2.1.2) instead of adaptive sampling is much less efficient (green dots).

much smaller than the actual best margin $m^* = 0.1$, the algorithm quickly recovers from the false assumption and still takes advantage of S_L to converge significantly faster than when the low-fidelity boundary is ignored ($m_0 = 0.01$). For reference, Figure 3.11 also shows the accuracy obtained from uniformly distributed high-fidelity samples from a Centroidal Voronoi Tesselation (Section 2.1.2). As expected based on Basudhar and Missoum (2010), selecting the high-fidelity samples via this design of experiments (DOE) is much less efficient than adaptive sampling.

Figure 3.12 shows the distribution of the first 40 high-fidelity samples for the three runs. Clearly, taking advantage of the low-fidelity boundary leads to high-fidelity samples that are concentrated close to the actual boundary, where they are the most informative. Single-fidelity adaptive sample ($m_0 = 2$) on the other hand wastes some high-fidelity samples in regions where the low-fidelity boundary is perfectly accurate.

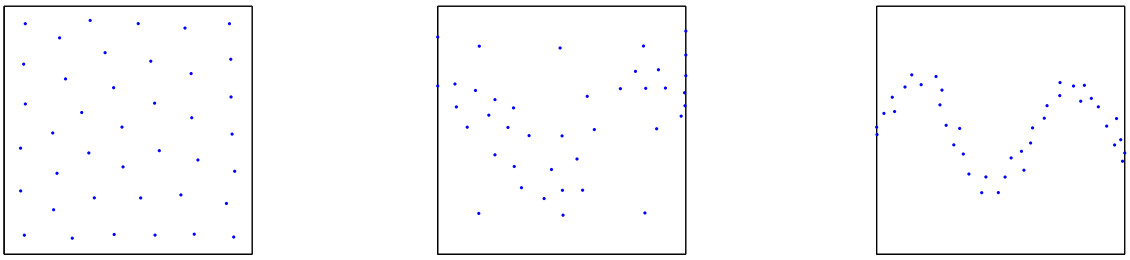

(a) Uniform DOE (b) $m_0 = 2$ (c) $m_0 = 0.01$

Figure 3.12: The distribution of the first 40 high-fidelity samples shows how the multi-fidelity algorithm does not waste samples in regions of the design space correctly classified by the low-fidelity model.

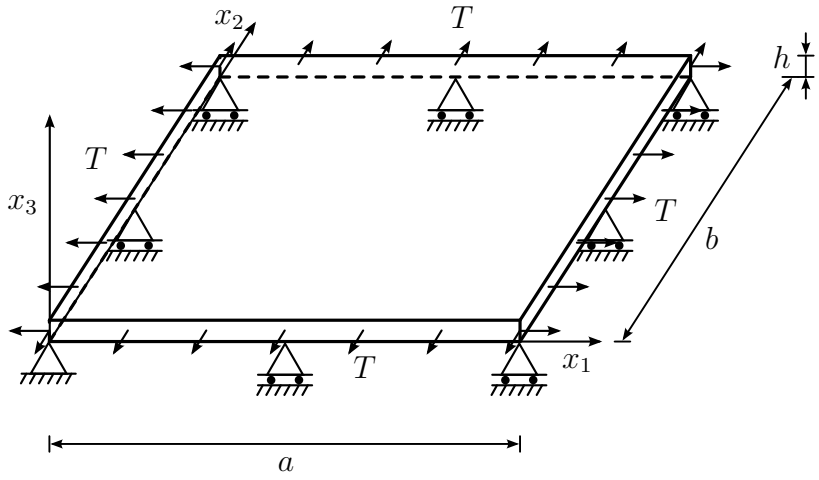

Figure 3.13: Simply supported plate: The steel plate is simply supported along its perimeter in the x_3 direction and uniform tension T is applied in the (x_1, x_2) plane.

Three-dimensional Steel Plate Problem

This three-dimensional test problem is based on an analytical formula for the natural frequencies of a simply supported, pre-stressed, isotropic plate as shown in Figure 3.13. The high-fidelity model accounts for the effects of pre-stress, while the low-fidelity model does not. For the purpose of testing the algorithm, the uniform tension T, applied to the perimeter, is used as a tuning parameter to adjust the discrepancy between the two boundaries. The first natural frequency of this rectangular plate under uniform tension is given by Antoine and Kergomard (2008):

Parameter	Value (Range)
Width a	0.5 – 1.5 m
Length b	0.5 – 1.5 m
Thickness h	2.5 – 7.5 mm
Young's Modulus E	210 $\times 10^9$ Pa
Density ρ	7800 kg/m^3
Poisson's ratio ν	0.3
Uniform tension applied on perimeter T	500 N/m, 5000 N/m, 25000 N/m

Table 3.1: Parameters affecting the natural frequency of a simply supported steel plate (Equation 3.39).

$$\omega_p = \sqrt{\frac{1}{\rho h}}\sqrt{\frac{Eh^3}{12\left(1-\nu^2\right)}\left(\frac{\pi^2}{a^2}+\frac{\pi^2}{b^2}\right)^2 + T\left(\frac{\pi^2}{a^2}+\frac{\pi^2}{b^2}\right)} \tag{3.39}$$

with parameters listed in Table 3.1. Using the dimensions of the plate as variables, the high-fidelity model classifies samples by comparing ω_p to a threshold of 120 rad/s:

$$M_H(\boldsymbol{x}) = \sqrt{\frac{1}{\rho x_3}}\sqrt{\frac{Ex_3^3}{12\left(1-\nu^2\right)}\left(\frac{\pi^2}{x_1^2}+\frac{\pi^2}{x_2^2}\right)^2 + T\left(\frac{\pi^2}{x_1^2}+\frac{\pi^2}{x_2^2}\right)} - 120\,\frac{\text{rad}}{s} \tag{3.40}$$

The low-fidelity model uses instead the natural frequency of the unstressed plate:

$$M_L(\boldsymbol{x}) = \sqrt{\frac{1}{\rho x_3}}\sqrt{\frac{Ex_3^3}{12\left(1-\nu^2\right)}\left(\frac{\pi^2}{x_1^2}+\frac{\pi^2}{x_2^2}\right)^2} - 120\,\frac{\text{rad}}{s} \tag{3.41}$$

The amount of tension T on the pre-stressed plate has a strong effect on the shape of the high-fidelity failure boundary as shown in Figures 3.15a, 3.16a and 3.17a, which depict the low- and high-fidelity failure boundaries for three values of T: 500 N/m, 5000 N/m and 25000 N/m. For each of the three cases of T, the multi-fidelity algorithm is run with three different values of the initial margin m_0: 0.03, 0.15 and 3.0. In each case, the algorithm is stopped when the high-fidelity SVM S_H reaches an error of $\epsilon(S_H, M_H) \leq 0.001$. To account for random variation, mainly due to the random selection of folds during cross-validation (Section 2.1.1), each run is repeated multiple times to obtain the average error with respect to the number of high-fidelity samples as shown in Figure 3.14. Table 3.2 summarizes the results

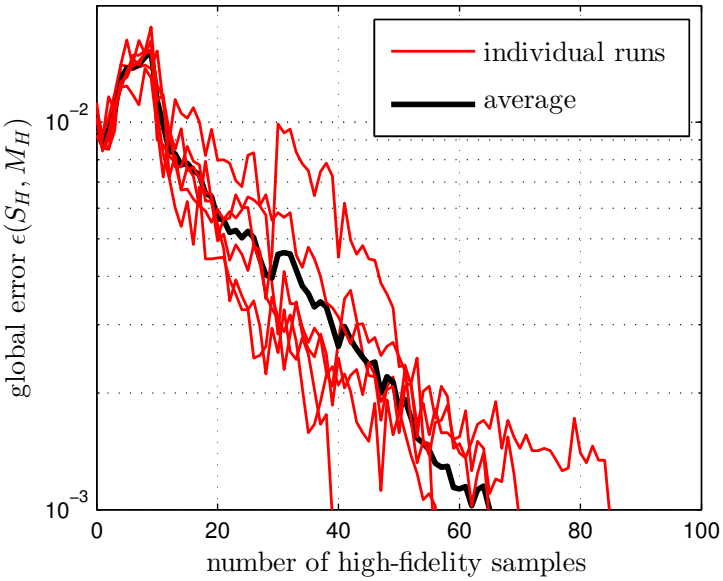

Figure 3.14: Evolution of the error measure $\epsilon(S_H, M_H)$ for the vibrating plate problem with pre-stress $T = 500$ N/m. Multiple runs (red) of the multi-fidelity algorithm with initial margin $m_0 = 0.03$ are averaged (black) to judge the performance of the algorithm.

by giving the average number of high-fidelity samples required to reach the error threshold for each of the nine cases.

In summary, this test problem shows the robustness and versatility of the algorithm: Though very large reductions ($\approx 60\%$) in the number of high-fidelity samples only occur if the low-fidelity model provides a relatively close approximation of the high-fidelity failure boundary, a low-fidelity boundary with large discrepancies still provides significant reductions (10 – 20%), especially in combination with a reasonable guess of the margin. However, even misleading the algorithm with a very inaccurate low-fidelity boundary, that is assumed to be very precise (small initial margin) leads to only a moderate increase in high-fidelity samples (5 – 10%).

N-dimensional Sphere Problem

This last test problem investigates the applicability of the multi-fidelity algorithm to higher-dimensional problems. The analytical models are formulated such that

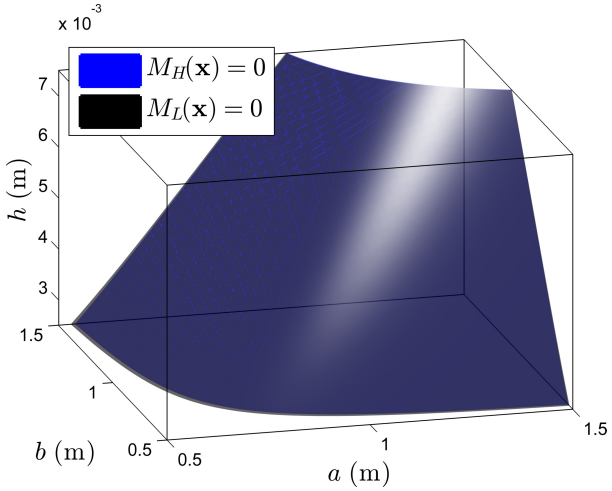

(a) Low-fidelity (black) and high-fidelity (blue) failure boundaries.

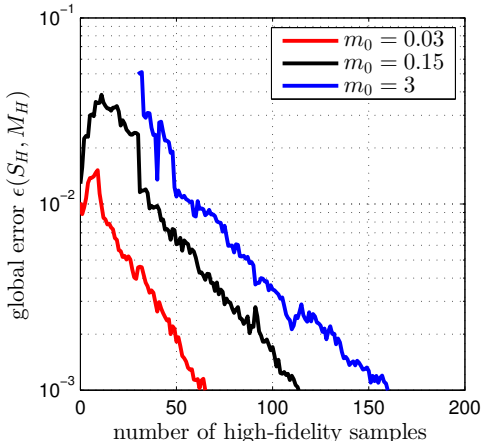

(b) Evolution of error measure for three cases of initial margin (averaged).

Figure 3.15: For small pre-stress ($T = 500$ N/m) the low- and high-fidelity failure boundaries are very close (a) and the smallest initial margin leads to the highest reduction of high-fidelity samples (b).

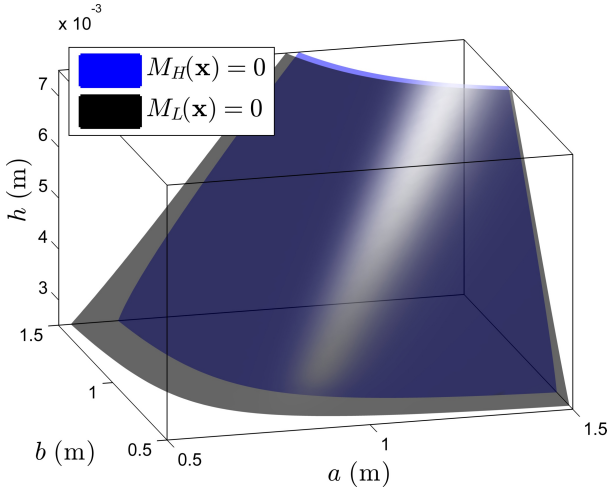

(a) Low-fidelity (black) and high-fidelity (blue) failure boundaries.

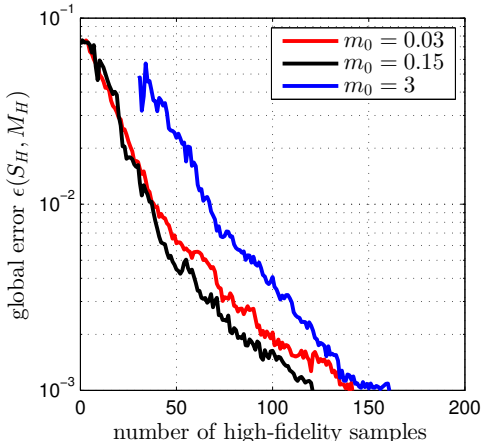

(b) Evolution of error measure for three cases of initial margin (averaged).

Figure 3.16: For large pre-stress ($T = 5000$ N/m) the low- and high-fidelity failure differ significantly (a). Both the smallest and medium initial margins reduce the number of high-fidelity samples (b) moderately. Also see Table 3.2

.

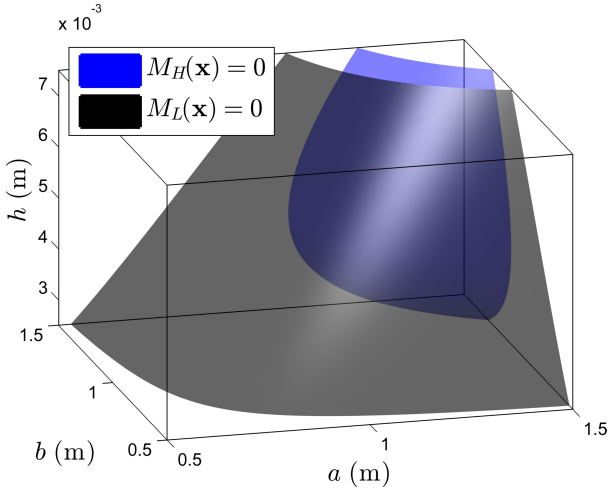

(a) Low-fidelity (black) and high-fidelity (blue) failure boundaries.

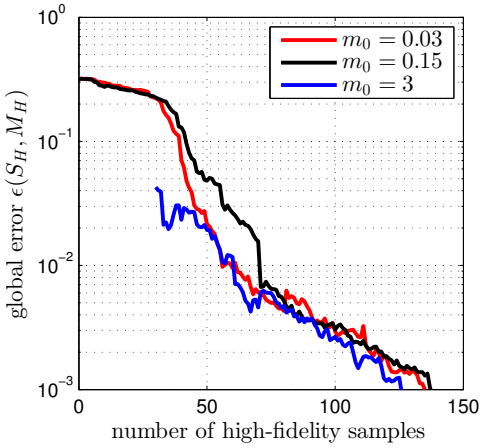

(b) Evolution of error measure for three cases of initial margin (averaged).

Figure 3.17: With very large pre-stress ($T = 25000$ N/m) the low-fidelity model (black) does not provide a useful approximation (a). Using a small initial margin is misleading to the algorithm, but causes only a slight increase of high-fidelity samples (b). Also see Table 3.2

.

Applied Tension T	Initial Margin m_0	High-fidelity sample count
500 N/m	0.03	62.0
	0.15	110.2
	3.0	152.3
5000 N/m	0.03	129.2
	0.15	115.6
	3.0	146.8
25000 N/m	0.03	136.0
	0.15	133.8
	3.0	125.3

Table 3.2: Summary of results of the vibrating steel plate problem: For each combination of initial margin m_0 and applied tension T the average number of high-fidelity samples required to reach the error threshold 0.001 quantifies the rate of convergence.

comparable problems in 3-, 5-, 7- and 9-dimensional design spaces are solved and the convergence of the algorithm is compared. Both the low- and high-fidelity models represent spherical failure boundaries with different curvatures. For each case, the design space is an n-dimensional hypercube given by:

$$D = \{\boldsymbol{x} \in \mathbb{R}^n | x_i \in [0,1]\} \text{ with } i = 1, ..., n \tag{3.42}$$

The analytical high-fidelity failure boundary is an n-dimensional hypersphere, centered at the origin with radius R_H such that 10% of the design space are classified as feasible:

$$M_H(\boldsymbol{x}) = \sum_{i=1}^{n} x_i^2 - R_H(n)^2 \tag{3.43}$$

Since the volume of an n-ball is given by

$$V_n = R^n \cdot \begin{cases} \frac{\pi^{\frac{n}{2}}}{\left(\frac{n}{2}\right)!} & \text{if } n \text{ is even} \\ \frac{2^{\frac{n+1}{2}} \pi^{\frac{n-1}{2}}}{n!!} & \text{if } n \text{ is odd} \end{cases} \tag{3.44}$$

with double factorial defined as $n!! = 1 \cdot 3 \cdot \ldots \cdot n$, the correct radius R_H, such that 10% of the design space is feasible, may be calculated as:

$$R_H(n) = \begin{cases} \left(0.1 \frac{\left(\frac{n}{2}\right)!}{\pi^{\frac{n}{2}}}\right)^{\frac{1}{n}} & \text{if } n \text{ is even} \\ \left(0.1 \frac{n!!}{\cdot 2^{\frac{n+1}{2}} \pi^{\frac{n-1}{2}}}\right)^{\frac{1}{n}} & \text{if } n \text{ is odd} \end{cases} \tag{3.45}$$

Now, the low-fidelity boundary is also a hyper-sphere, but with different radius R_L:

$$M_L(\boldsymbol{x}) = \sum_{i=1}^{n} x_i^2 - R_L(n)^2 \tag{3.46}$$

where $R_L(n)$ is chosen such that the error of the low-fidelity boundary $\epsilon(M_L, M_H)$ is exactly 5 %. Of the two solutions for $R_L(n)$, the smaller one is selected, leading to:

$$R_L(n) = \begin{cases} \left(0.05 \frac{\left(\frac{n}{2}\right)!}{\pi^{\frac{n}{2}}}\right)^{\frac{1}{n}} & \text{if } n \text{ is even} \\ \left(0.05 \frac{n!!}{\cdot 2^{\frac{n+1}{2}} \pi^{\frac{n-1}{2}}}\right)^{\frac{1}{n}} & \text{if } n \text{ is odd} \end{cases} \tag{3.47}$$

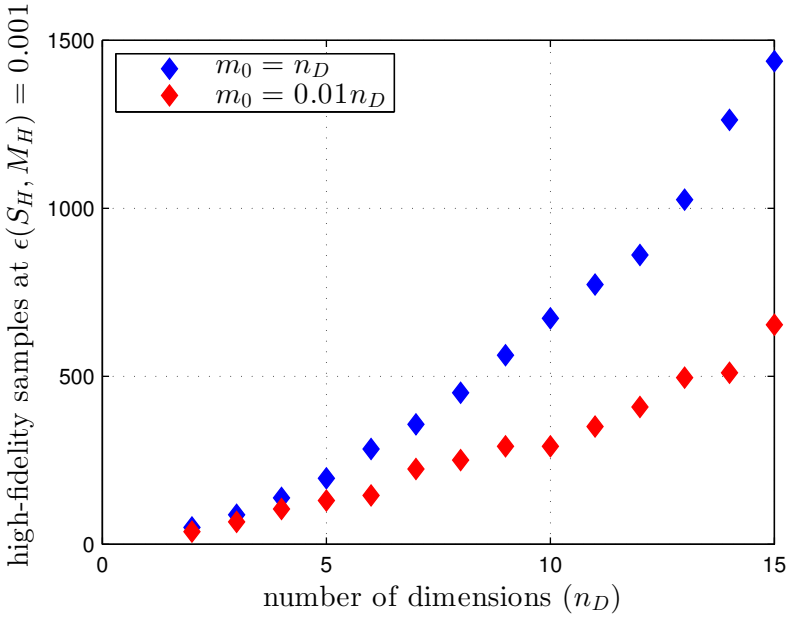

Figure 3.18: Convergence of the n-dimensional hypersphere problem: Number of high-fidelity samples required to reach the error threshold of 0.001 for all cases of dimensionality n. Taking advantage of the low-fidelity boundary ($m_0 = 0.01$) reduced the required high-fidelity evaluations significantly and the effect appears to be more pronounced with increasing dimensionality.

For each case of the dimensionality n, the multi-fidelity algorithm is applied with two values for the initial margin m_0, which are $0.01n$ and n. Using $m_0 = n$ means that the low-fidelity boundary is completely ignored and provides a reference to quantify the advantage of taking the low-fidelity boundary into consideration. Figure 3.18 summarizes the results by plotting the number of high-fidelity samples required to reach the error threshold of 0.001 with respect to the dimensionality, and Figure 3.19 shows the average evolution of the error measure $\epsilon(M_H, M_L)$ for various cases of n. It is concluded that the multi-fidelity algorithm causes a significant reduction in high-fidelity samples for all cases of n and the effect appears to be more pronounced with increasing dimensionality.

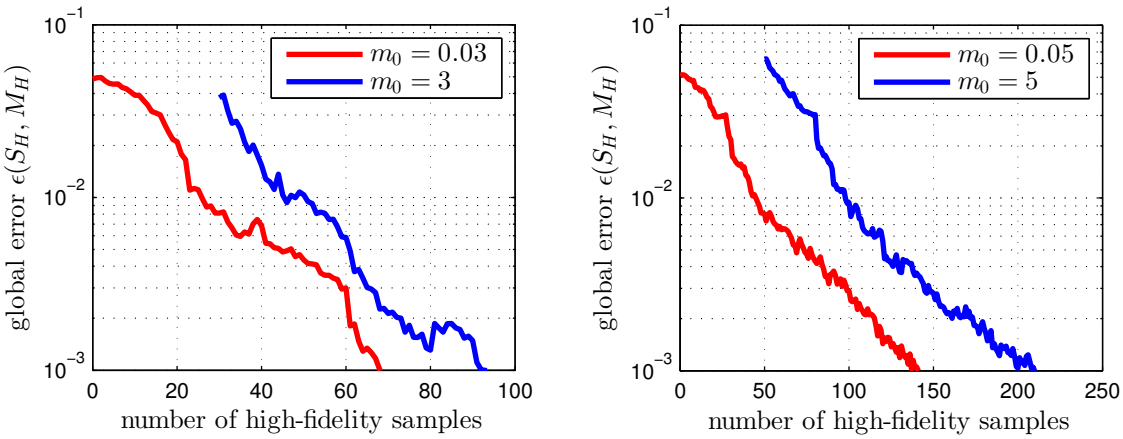

(a) 3-dimensional

(b) 5-dimensional

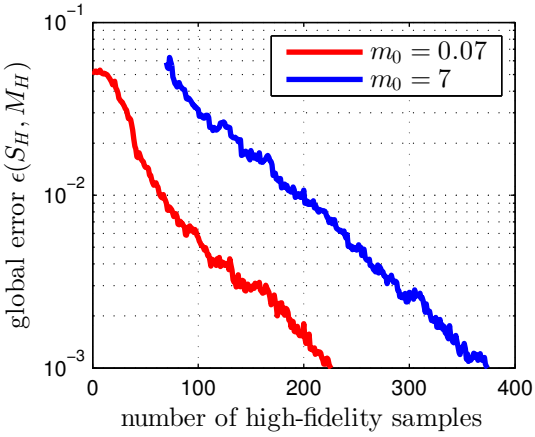

(c) 7-dimensional

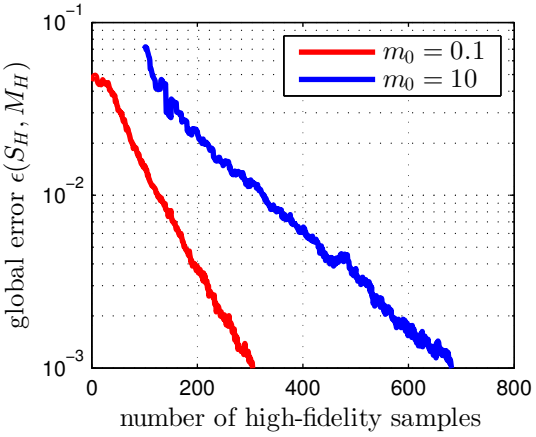

(d) 10-dimensional

Figure 3.19: Average evolution of the error $\epsilon(S_H, M_H)$ with respect to the number of evaluated high-fidelity samples for the n-dimensional hypersphere problem with $n = 3$, 5, 7 and 10.

CHAPTER 4

AEROELASTIC STABILITY BOUNDARIES

In this section, the multi-fidelity algorithm is used to obtain the aeroelastic stability boundaries for two simulation models. The first model, proposed by Lee et al. (1999a), simulates a rigid two degree-of-freedom airfoil, supported by nonlinear springs, in unsteady incompressible flow (Section 4.1). Here, the goal is to obtain the stability boundary in terms of fluid velocity and initial conditions, while taking advantage of a readily available low-fidelity stability boundary obtained from a linear analysis assuming linear springs.

The second model (Section 4.2) simulates a finite-element model of a flexible wing in unsteady potential flow (Section 2.3.3), using the G-method for flutter analysis (Section 2.3.3). For this problem, various simulation parameters related to discretization affect the accuracy of the model, and two settings are defined to obtain both a low-fidelity model for quick approximations and a slower high-fidelity model for precise results.

4.1 Nonlinear Two Degree-of-Freedom Airfoil

In this section the multi-fidelity algorithm (Chapter 3) is employed to construct the stability boundary of a rigid airfoil supported by nonlinear springs, as a function of initial pitch conditions and reduced velocity.

Figure 4.1 schematically shows the rigid airfoil, described and analyzed in great detail by Lee et al. (1999a), and its two degrees of freedom, which are the pitch angle (α) and the plunge displacement (h). The airfoil is supported at the elastic axis by nonlinear translational and rotational springs, opposing pitch and plunge,

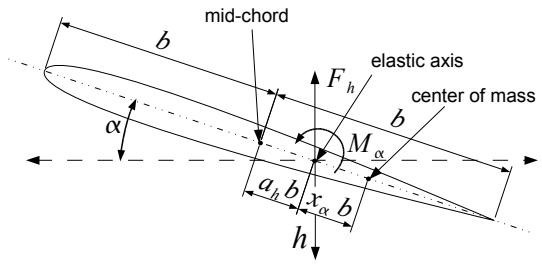

Figure 4.1: Description of the two degree of freedom airfoil (Lee et al. (1999a)). The restoring forces due to the nonlinear springs are denoted by F_h and M_α.

whose restoring force is given by polynomials of respective displacement:

$$\begin{aligned} M_\alpha &= K_\alpha(\alpha + k_{3\alpha}\alpha^3 + k_{5\alpha}\alpha^5) \\ F_h &= K_h(\xi + k_{3h}\xi^3 + k_{5h}\xi^5) \end{aligned} \tag{4.1}$$

where $\xi = \frac{h}{b}$ is the non-dimensional plunge. All parameters of the model are summarized on Table 4.1.

In the linear elastic case ($k_{3\alpha}$, $k_{5\alpha}$, k_{3h}, $k_{5h} = 0$), the aeroelastic equations of motion were derived by Fung (2002) as a system of eight first-order differential equations. Under these conditions the system will be either stable or experience static divergence or flutter. The speed at which the system becomes unstable is independent of the initial conditions and is referred to as the critical speed.

In the nonlinear case, Lee et al. (1999a) derived the equations of motion for cubic stiffnesses, which were later extended to include pentic stiffness terms (Missoum et al. (2010)). As described in Section 2.3.1, the nonlinear stiffness terms (representative of structural geometric nonlinearities for actual wings) enable limit cycle oscillations (LCO), which brings the number of possible failure modes to three: static divergence, divergent flutter and LCO. These instabilities are referred to as sub-critical if they may occur below the critical speed of the linearized (low-fidelity) model. In general, the failure mode for a given configuration depends on the geometry (x_α, r_α), the spring stiffness coefficients (Equation 4.1) and the initial conditions (Table 4.1). For example, sub-critical LCO may occur with a linear spring in plunge ($k_{3h}, k_{5h} = 0$) combined with a negative cubic and positive pentic stiffness in pitch

($k_{3\alpha} < 0, k_{5\alpha} > 0$), if the initial perturbation is large enough.

In the lower-fidelity model the airfoil is supported by linear springs and its behavior is described by a linear system of differential equations. Therefore, the Jacobian matrix of the equations of motion is available analytically and the stability classification may be achieved using a spectral analysis of the Jacobian (Lee et al. (1999a); Seydel (1988)). Due to the linearity of the low-fidelity model, the flutter velocity is independent of the initial conditions.

The higher-fidelity model includes cubic and pentic stiffness terms, which make the equations of motion nonlinear, therefore time integration is required to study the behavior of the system for given initial conditions. Specifically, the equations are integrated via the explicit Euler method and the code was fully parameterized with respect to the quantities in Table 4.1. The resulting time response is used to classify the scenario as stable or unstable based on the system energy criterion (Section 2.3.1). The classification is not based on the system energy E directly, but on the dimensionless system energy $\bar{E}$ defined by:

$$\bar{E} = \frac{E}{\rho U^2 b^2} \tag{4.2}$$

with free stream velocity U, planar air density ρ and airfoil semi-chord b. Since the airfoil itself is rigid and gravity is neglected, the only potential energy is the energy stored in the nonlinear springs. The energy stored in the translational spring (plunge) is calculated as:

$$\bar{E}_{spring\,\xi} = \mu\pi \left(\frac{\omega}{U_R}\right)^2 \left(\frac{1}{2}\xi^2 + \frac{1}{4}k_{3h}\xi^4 + \frac{1}{6}k_{5h}\xi^6\right) \tag{4.3}$$

Similarly for the rotational spring in pitch:

$$\bar{E}_{spring\,\alpha} = \mu\pi \left(\frac{r_\alpha}{U_R}\right)^2 \left(\frac{1}{2}\alpha^2 + \frac{1}{4}k_{3\alpha}\alpha^4 + \frac{1}{6}k_{5\alpha}\alpha^6\right) \tag{4.4}$$

The kinetic energy of the rigid airfoil in the translational and rotational degree-of-freedom is calculated as:

$$\bar{E}_{kinetic\,\xi} = \frac{1}{2}\mu\pi\xi'^2 + 2x_\alpha\alpha'\xi'\cos(\alpha) + (x_\alpha\alpha')^2 \tag{4.5}$$

Parameter	Value (Range)
Initial plunge $\xi(0) = \frac{h(0)}{b}$	0.0
Initial plunge Velocity $\xi'(0)$	0.0
Initial pitch angle $\alpha(0)$	-15° - 15°
Initial pitch velocity $\alpha'(0)$	0° - 2.5°
Reduced free-stream velocity $U_R = \frac{U}{b\omega_\alpha}$	3.0 - 9.0
Airfoil to air mass ratio $\mu = \frac{m}{\pi\rho b^2}$	100.0
Ratio of natural frequencies $\omega = \frac{\omega_\xi}{\omega_\alpha}$	0.2
Elastic axis-mid chord separation a_h	-0.5
Center of mass - elastic axis separation x_α	0.25
Radius of gyration of airfoil r_α	0.5
Pitch cubic stiffness coefficient $k_{3\alpha}$	-3.0
Plunge cubic stiffness coefficient k_{3h}	0.0
Pitch pentic stiffness coefficient $k_{5\alpha}$	10.0
Plunge pentic stiffness coefficient k_{5h}	0.0
Damping in pitch and plunge	0

Table 4.1: Airfoil Parameters

$$\bar{E}_{kinetic\,\alpha} = \frac{1}{2}\mu\pi U_R^2 \alpha'^2 \tag{4.6}$$

where the prime sign for the degrees-of-freedom represent the derivative with respect to the non-dimensional time $\tau = \frac{Ut}{b}$. At each time step of the integration the total energy $\bar{E}$ is calculated:

$$\bar{E} = \bar{E}_{spring\,\xi} + \bar{E}_{spring\,\alpha} + \bar{E}_{kinetic\,\xi} + \bar{E}_{kinetic\,\alpha} \tag{4.7}$$

and the system is classified as stable if this energy converges to zero.

4.1.1 Stability Boundaries

The stability boundary was obtained with respect to three parameters, which are the initial pitch angle $\alpha(0)$, initial pitch velocity $\alpha'(0)$ and the reduced free-stream velocity U_R with ranges given in Table 4.1. Also listed are the fixed parameters, which were chosen to match the values presented by Lee et al. (1999a).

Figure 4.2 shows the three dimensional stability boundary according to the low-fidelity model. Since the low-fidelity model is linear, stability does not depend on the initial state and therefore the stability boundary is a straight plane, defined by the

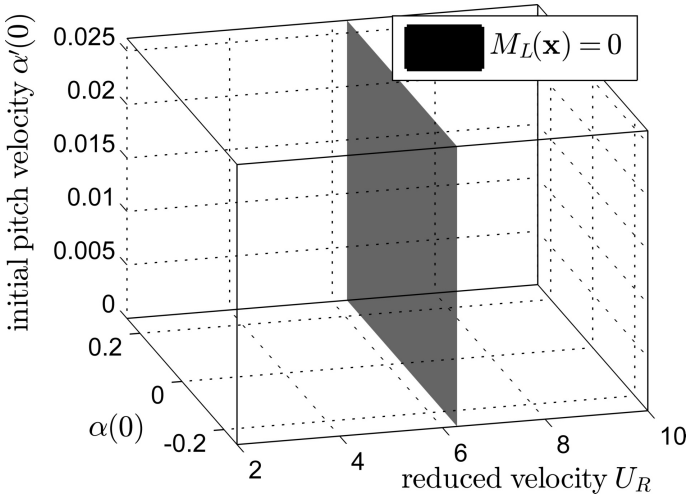

Figure 4.2: Low-fidelity stability boundary: For this linear model divergent flutter occurs beyond the critical reduced velocity of 6.29, independent of initial conditions.

critical speed. The system is asymptotically stable for lower velocities and flutter occurs to the right of the boundary. The critical velocity $U_c = 6.29$ is obtained from a one-dimensional search along the velocity axis, based on spectral analysis of the Jacobian matrix (Section 4.1). This is a very fast procedure, therefore the low-fidelity boundary is obtained in a few seconds.

Figure 4.3 shows high-fidelity SVM approximation of the high-fidelity stability boundary as obtained by adaptive sampling. As depicted, a very high number of samples (1000) was used to eliminate any doubt in the accuracy of this boundary, which is used as the reference to study the convergence of the multi-fidelity algorithm (Section 3). Like all other SVMs in this dissertation, the high-fidelity SVM itself was constructed in a normalized design space, but is plotted with respect to the actual ranges of the parameters. The high-fidelity model with nonlinear springs is asymptotically stable to the left of the boundary and divergent flutter occurs to the right of the boundary. The volume between the linear low-fidelity and the nonlinear high-fidelity boundaries is the set of scenarios that lead to sub-critical LCO, where initial conditions lead to limit-cycle oscillations even though the linearized system is stable.

Figure 4.4 presents the convergence of the multi-fidelity algorithm for three cases

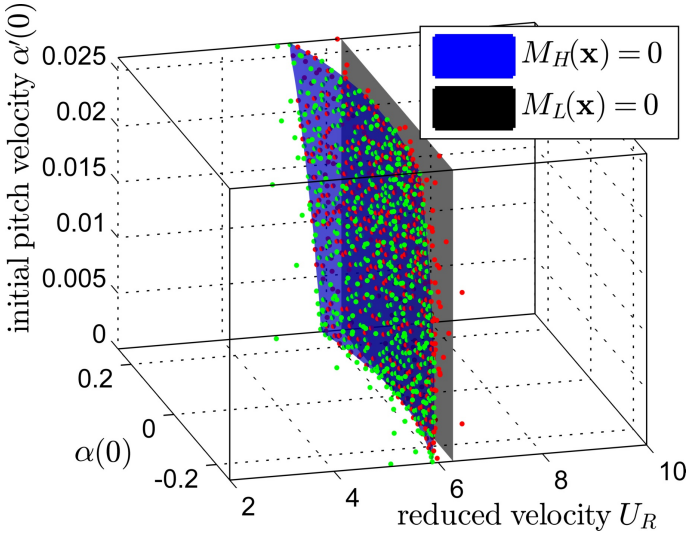

Figure 4.3: High-fidelity stability boundary: For this nonlinear model the blue boundary represents the critical reduced velocity at which limit-cycle oscillations (LCO) appear. This reference SVM boundary is constructed from 1000 evaluated high-fidelity samples (green and red dots) and the density of points, separated by the boundary, suggests that the residual error is very small.

of initial margin m_0, where the error measure $\epsilon(S_H, M_H)$ is based on comparison to the previously obtained reference boundary (Figure 4.3). The algorithm was stopped as soon as the error dropped below 1×10^{-3} and the reduction of high-fidelity samples due to taking advantage of the low-fidelity boundary is about 10 – 20%, which is comparable to the results of the second analytical test problem (Section 3.4).

4.1.2 Conclusions

This aeroelastic test problem shows the ability of the multi-fidelity algorithm to obtain the stability boundary of a nonlinear simulation model, based on classified training samples. Taking advantage of the linear low-fidelity stability boundary leads to modest, but significant reductions of high-fidelity samples (10 – 20 %). The CPU time to obtain the low-fidelity boundary was only a few seconds, which is negligible when considering the 12 seconds required to classify a single high-fidelity sample. Therefore, the achieved reduction of high-fidelity samples clearly justifies the additional effort to obtain the low-fidelity boundary.

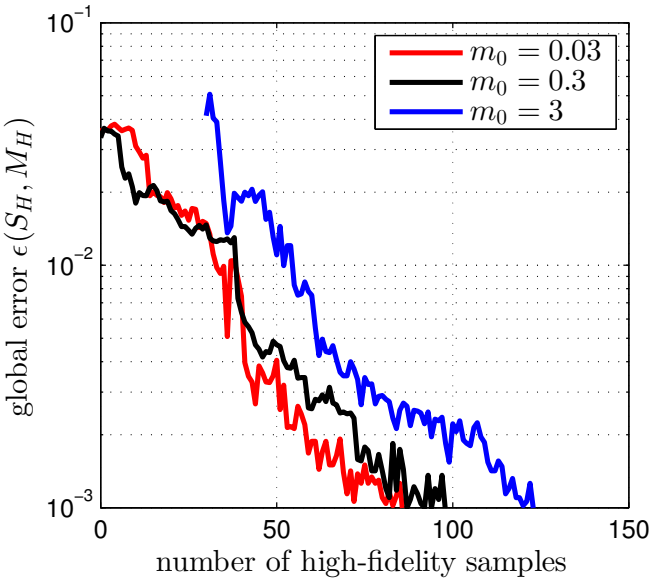

Figure 4.4: Convergence of the multi-fidelity algorithm to the 3-dimensional high-fidelity stability boundary for three values of initial margin.

4.2 Cantilevered Wing Model in ZAERO

In this problem, the aeroelastic stability of a cantilevered wing is studied via a commercial software for aeroelastic stability analysis. Using different setting for various simulation parameters, both a low-fidelity model for quick approximations and a slower high-fidelity model for more accurate results are employed to obtain the stability boundary in terms of the geometry of the wing. The simulation model (Section 4.2) simulates a finite-element model of a flexible wing in unsteady potential flow (Section 2.3.3), using the G-method for flutter analysis (Section 2.3.3).

The geometry of the solid aluminum wing is given by five parameters, which comprise the design space. As shown in Figure 4.5, the planform of the wing is defined by 3 variables: sweep angle $\Lambda_{1/4}$, taper ratio λ and semi-span $b/2$, while the area S of the wing is maintained constant. The thickness of the wing, constant chord wise, is given along the span by an exponential function with two parameters k_1 and k_2 (Equation 4.8), which are used as the two other variables of the problem.

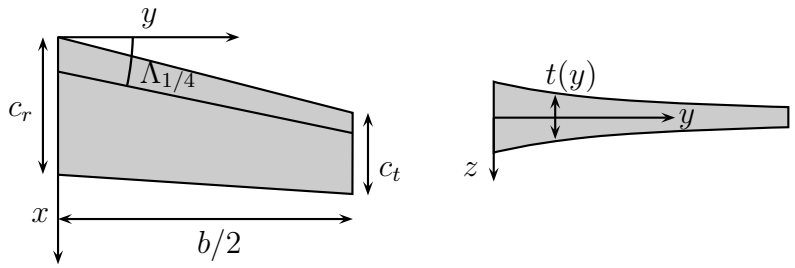

Figure 4.5: Wing Geometry. For a given wing area, the planform of the wing is given by 3 variables: Sweep angle $\Lambda_{1/4}$, taper ratio λ and semi-span $b/2$. The span-wise thickness is governed by Equation 4.8.

All design variables and their ranges are listed in Table 4.2.

$$t(y) = k_1 e^{\frac{2k_2 y}{b}} \tag{4.8}$$

A design is considered feasible if no flutter and divergence speed instabilities occur at the given flight conditions, based on the G-method for flutter analysis (Section 2.3.3) in unsteady potential flow (Section 2.3.3). This binary constraint (stable/unstable) is evaluated through the aeroelasticity code ZAERO (Zona (2011)) from Zona Technologies, which considers both failure modes. Table 4.3 lists the fixed parameters required to evaluate each design, such as material properties and flight conditions, where velocity and air density are obtained from an atmospheric table to match the altitude and Mach number. For each combination of design parameters, a structural model is built to obtain mass matrix, mode shapes and natural frequencies of the wing. Specifically, this structural FE model consists of a mapped mesh of CQUAD4 shell elements using the Genesis software (Vanderplaats (2006)). To model the aerodynamics, ZAERO uses a flat panel mesh (Section 2.3.3) and an infinite plate spline to transfer forces and displacements between the structural and aerodynamic model. All of the modeling parameters such as number of elements and number of mode shapes are listed in Table 4.4. Figure 4.6a shows the planform and the high-fidelity structural and aerodynamic model of a typical swept-back wing, and Figure 4.6b shows the thickness distribution of this wing. The first 6 mode shapes according to the high-fidelity structural model are presented in Figure 4.7.

A low-fidelity model is generated by using a coarser mesh for both the structural

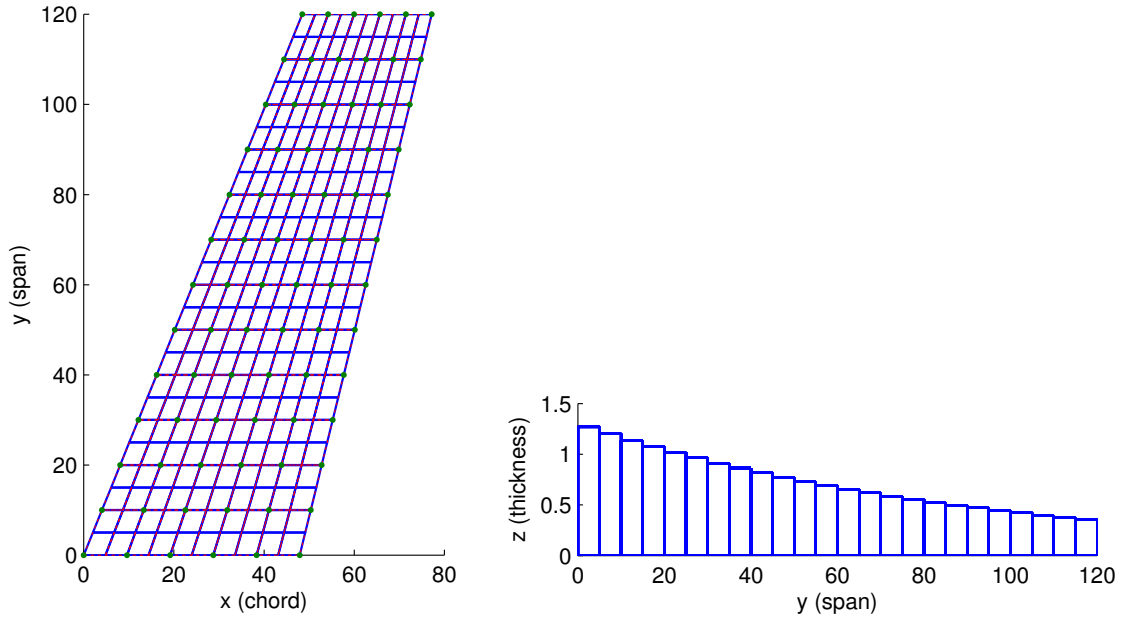

(a) Planform of the wing: Structural shell (blue) and aerodynamic flat panel mesh (dashed red). For each mode shape a spline is fitted to selected grid points (green) to transfer forces and displacements between the two models.

(b) Spanwise exponential thickness distribution (Equation 4.8) of the wing (Table 4.2). Chordwise, the thickness is constant.

Figure 4.6: Geometry of the example wing (Table 4.2) corresponding to the high-fidelity parameters in Table 4.4.

model and the aerodynamic model, while considering only a reduced number of mode shapes (Table 4.4). Each evaluation of the low-fidelity model takes 1 minute as opposed to 8 minutes for the high-fidelity model.

4.2.1 Stability Boundaries

The low-fidelity model (Table 4.4) is used to obtain an SVM approximation S_L of the low-fidelity stability boundary through adaptive sampling. For this purpose, 50 uniformly distributed low-fidelity samples (Section 2.1.2) are used to construct the initial SVM, which is then refined by 350 additional max-min and anti-locking samples (Section 3.3.4). Figures 4.8 and 4.9 show two representative three-dimensional cross-sections of this boundary, obtained by fixing two of the 5 variables.

Geometric Parameter	Lower Bound	Upper Bound	Example
Sweep angle of quarter chord $\Lambda_{1/4}$	$-25°$	$25°$	$20°$
Taper ratio $\lambda = c_t/c_r$	0.5	1.0	0.6
Semi span $b/2$	100 in	150 in	120 in
Thickness parameter k_1	0.5 in	2 in	1.3 in
Thickness parameter k_2	-2	0	-1.3

Table 4.2: Design variables defining the wing geometry. The fixed wing area is given in Table 4.3.

Fixed Parameter	Value
Mach number	0.5
Altitude	10000 ft
Velocity	538.68 ft/s (match point)
Air density	3.2686×10^{-5} lb/in^3 (match point)
Angle of attack	0
Wing area S	32 ft^2
Young's modulus	9.2418×10^6 psi
Shear modulus	3.4993×10^6 psi
Density	0.097464 lb/in^3

Table 4.3: Fixed parameters used in the aeroelasticity problem: Material properties of aluminum and flight conditions.

Simulation Parameter	Low-Fidelity	High-Fidelity
Structural shell elements along chord	8	16
Structural shell elements along semi span	60	120
Number of structural modes	5	10
Aero-boxes along chord	8	16
Aero-boxes along semi span	10	20
CPU time per evaluation	1m	8m

Table 4.4: Definition of structural and aeroelastic model. The low-fidelity model uses a coarser mesh and fewer structural modes, therefore it is about 8 times faster to evaluate, but less accurate.

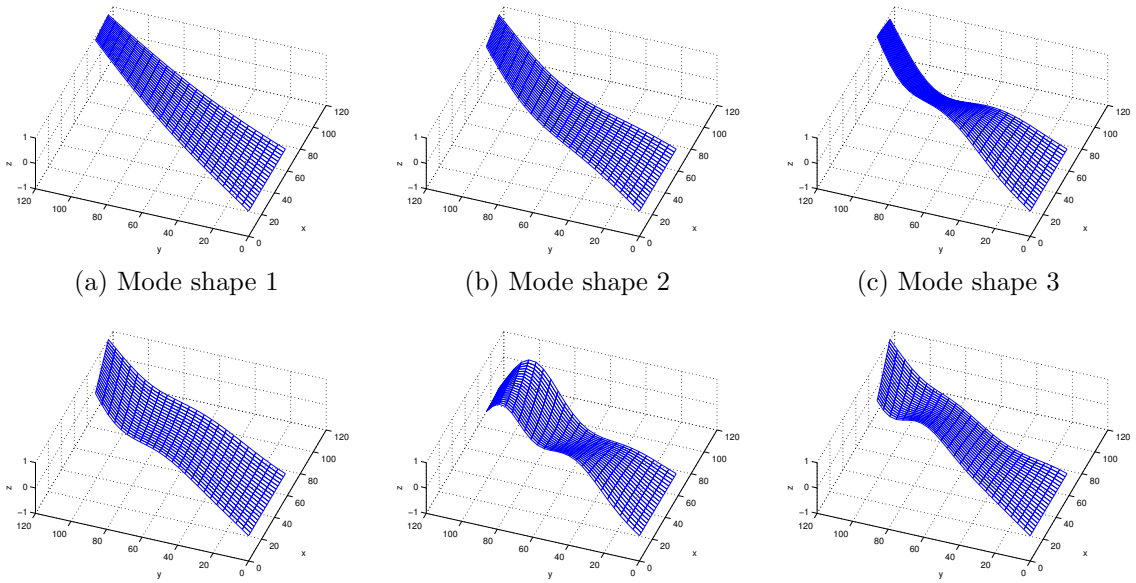

(a) Mode shape 1 (b) Mode shape 2 (c) Mode shape 3

(d) Mode shape 4 (e) Mode shape 5 (f) Mode shape 6

Figure 4.7: The first six mode shapes of the example wing (Table 4.2).

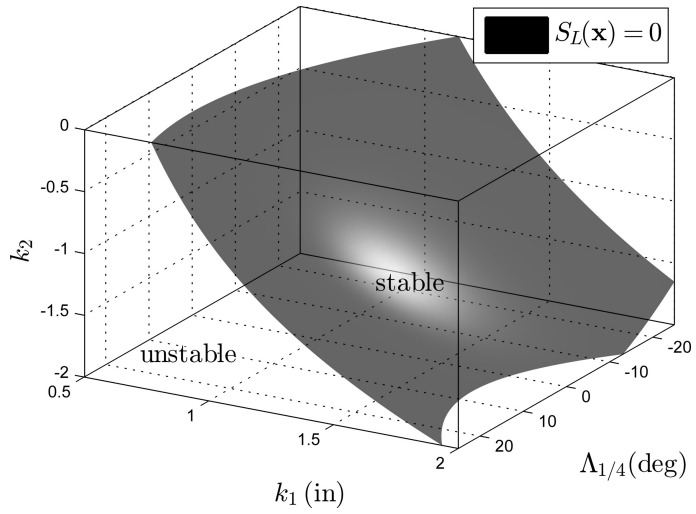

Figure 4.8: Low-fidelity stability boundary in terms of the thickness parameters k_1 and k_2 and sweep angle $\Lambda_{1/4}$ after evaluating 400 low-fidelity samples. Taper ratio λ and semi span $b/2$ are fixed at 0.75 and 125in respectively. While not shown in the figure, the unstable region of the design space is split into two segments characterized by flutter and divergence instability with divergence only occurring for forward swept wings ($\Lambda_{1/4} < 0$).

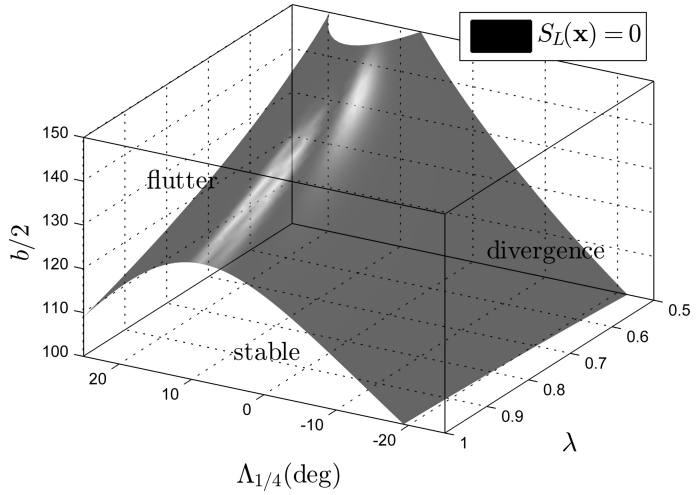

Figure 4.9: Low-fidelity stability boundary in terms of sweep angle $\Lambda_{1/4}$, taper ratio λ and semi-span $b/2$ after evaluating 400 low-fidelity samples. Thickness parameters k_1 and k_2 are fixed at 0.8in and -1, respectively. The unstable region on top of the boundary is split into flutter and divergence instabilities.

To improve efficiency in testing the multi-fidelity algorithm, a reference high-fidelity stability boundary was obtained from a very large number of adaptive samples (1500) without taking the low-fidelity boundary into account. Due to the large number of samples, this SVM was considered the true high-fidelity stability boundary and its three-dimensional cross-sections are shown in Figures 4.10 and 4.11 together with the low-fidelity boundary. Though the low-fidelity boundary appears to provide an excellent approximation in Figure 4.10, Figure 4.11 shows that the approximation is relatively poor in other regions of the design space.

The multi-fidelity scheme (Chapter 3) is used to obtain an approximation of the high-fidelity stability boundary while taking advantage of the low-fidelity boundary shown in Figures 4.8 and 4.9. As with all the test problems the initial margin is set to $0.01n$, with n being the number of dimensions and the evolution of the error measure $\epsilon(S_H, M_H)$ is shown in Figure 4.12. Clearly, taking advantage of the low-fidelity boundary ($m_0 = 0.05$) requires significantly fewer high-fidelity samples than adaptive sampling without consideration of the low-fidelity boundary ($m_0 = 5$). It should be mentioned that the low-fidelity boundary was obtained at significant

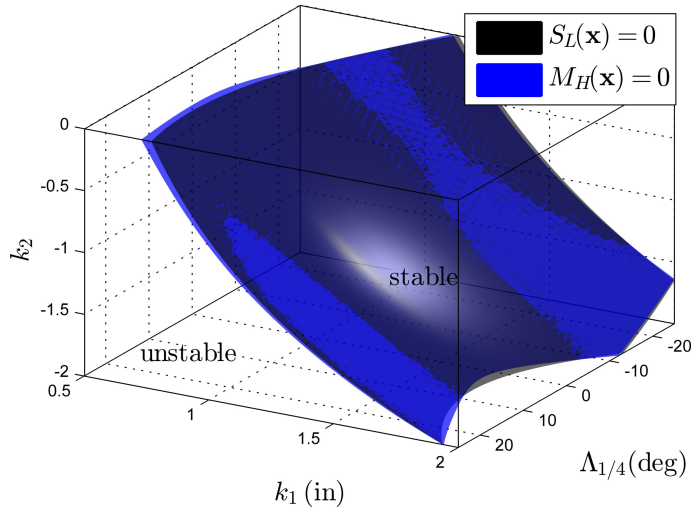

Figure 4.10: High-fidelity and low-fidelity stability boundary in terms of the thickness parameters k_1 and k_2 and sweep angle $\Lambda_{1/4}$. In this three-dimensional cross-section of the five-dimensional design space, the two stability boundaries are very close.

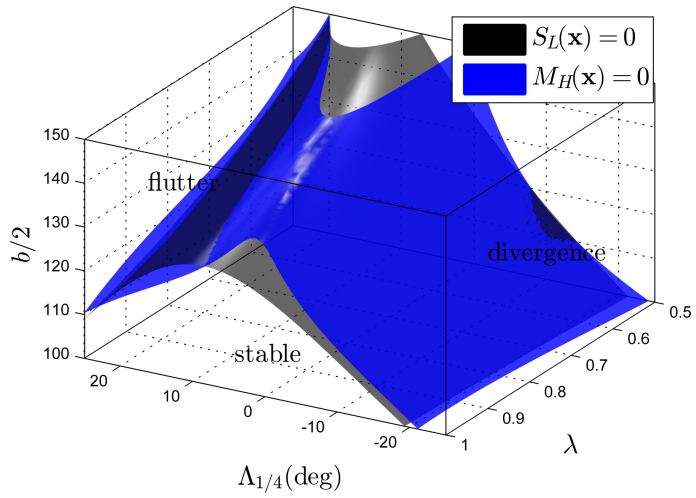

Figure 4.11: High-fidelity and low-fidelity stability boundary in terms of sweep angle $\Lambda_{1/4}$, taper ratio λ and semi-span $b/2$. In this three-dimensional cross-section of the five-dimensional design space, the low-fidelity boundary does not provide a good approximation of the high-fidelity stability boundary.

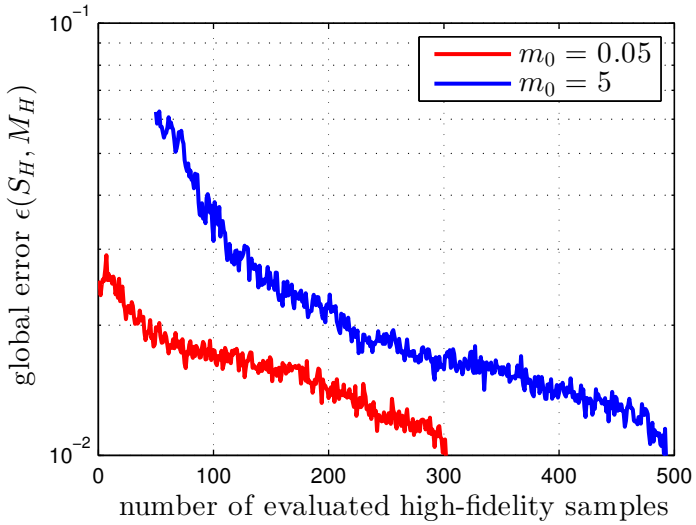

Figure 4.12: Convergence of the multi-fidelity algorithm to the 5-dimensional high-fidelity stability boundary.

computational expense, that is the 400 low-fidelity samples required as much CPU time as 50 high-fidelity samples. However, Figure 4.12 shows this to be a worthwhile investment, as the multi-fidelity algorithm requires about 180 fewer high-fidelity samples, thus reducing the overall computational expense by about 30%.

4.2.2 Conclusions

This second aeroelastic test problem shows the ability of the multi-fidelity algorithm to obtain the stability boundary of a five parameter wing model, analyzed via commercial aeroelasticity software. In comparison to the previous problem (Section 4.1), the current stability boundary is much more complex and features two different failure modes, that is flutter and static divergence. Though obtaining the low-fidelity stability boundary was associated with significant cost, the resulting reduction in high-fidelity samples clearly justifies this expense.

CHAPTER 5

MULTI-FIDELITY OPTIMIZATION

The multi-fidelity algorithm described in Chapter 3 seeks to construct an SVM constraint boundary that is accurate over the whole design space. However, for the purpose of numerical design optimization, it may be advantageous to limit high-fidelity samples to regions of the design space that are likely to contain the optimal design. Assuming a low evaluation cost of the objective function to minimize, this can be achieved by only a small modification of the multi-fidelity algorithm as presented in this section.

The main premise of this variant is the following: As soon as the algorithm has discovered a sample that is classified as feasible by the high-fidelity constraint model, it is wasteful to evaluate any other sample via the high-fidelity constraint, unless its objective function value is lower. To eliminate such waste, any high-fidelity sample $\boldsymbol{x}_i$ selected by the multi-fidelity algorithm is first evaluated via the objective function. If its value is higher than the current best feasible sample $\boldsymbol{x}^*$, then the new sample $\boldsymbol{x}_i$ is not evaluated via the high-fidelity constraint function, but instead added to the set of blocked samples X_b. This set of samples is ignored for the purpose of training the SVM, but treated as existing samples during the adaptive sampling (Section 3.3.4). Blocking samples in this way prevents the algorithm from selecting the same point again and forces the adaptive sampling routine to find max-min or anti-locking samples with lower objective function value than the current optimum $\boldsymbol{x}_k^*$.

This straight-forward modification requires only a small change to the implementation (Figure 5.1) and reduces the computational burden significantly if one only seeks to obtain the constrained optimum with respect to an inexpensive objective function. Unfortunately, this modification is not well suited for the case where evaluating the objective function is associated with significant cost, unless the ob-

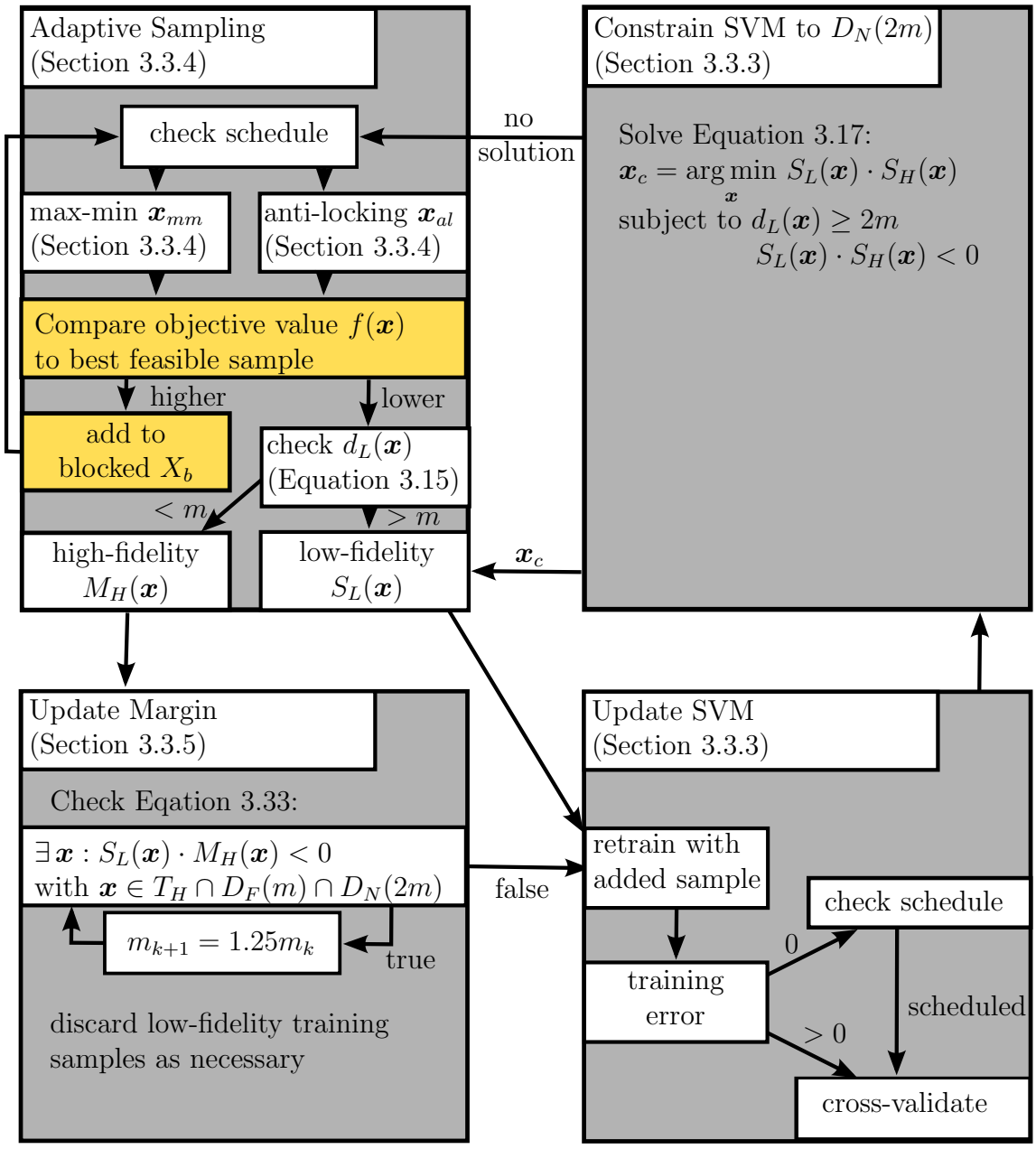

Figure 5.1: Detailed overview of the multi-fidelity algorithm. Modifications for the purpose of numerical design optimization are highlighted in yellow.

jective function is approximated via a surrogate (Section 2.1). Further, in the case of high-dimensional problems, the set of blocked samples X_b may become large and the adaptive sampling routine may require many iterations to locate another sample with lower objective function value.

However, the following sections present several problems, both analytical and based on aeroelasticity simulation models, that demonstrate the effectiveness of this variant of the algorithm to locate the constrained optimum. The first analytical problem (Section 5.1) features a two-dimensional design space in which the objective function is constrained by two constraints. The second problem is based on analytical formulas for the natural frequencies of a rectangular plate. Defined on a three-dimensional design space, it is identical to the test problem presented in Section 3.4, augmented by an objective function to minimize the weight. Finally Section 5.3, presents optimization results on the cantilevered wing introduced in Section 4.2. In this five-dimensional problem the weight of the wing is minimized, subject to aeroelastic stability constraints.

5.1 Goldstein-Price Test Problem

This first problem seeks to locate the constrained optimum of a two-dimensional objective function as shown in Figure 5.2. The design space D is defined by equal ranges on two design parameters:

$$D = \left\{ \boldsymbol{x} \in \mathbb{R}^2 | x_i \in [-2, 2] \right\} \tag{5.1}$$

The objective function f is the well-known Goldstein-Price function (Dixon (1978)) defined as:

$$A(\boldsymbol{x}) = 19 - 14x_1 + 3x_1^2 - 14x_2 + 6x_1x_2 + 3x_2^2 \tag{5.2}$$

$$B(\boldsymbol{x}) = 18 - 32x_1 + 12x_1^2 + 48x_2 - 36x_1x_2 + 27x_2^2 \tag{5.3}$$

$$f(\boldsymbol{x}) = \log((1 + A(\boldsymbol{x}) \cdot (x_1 + x_2 + 1)^2) \cdot (30 + B(\boldsymbol{x}) \cdot (2x_1 - 3x_2)^2)) \tag{5.4}$$

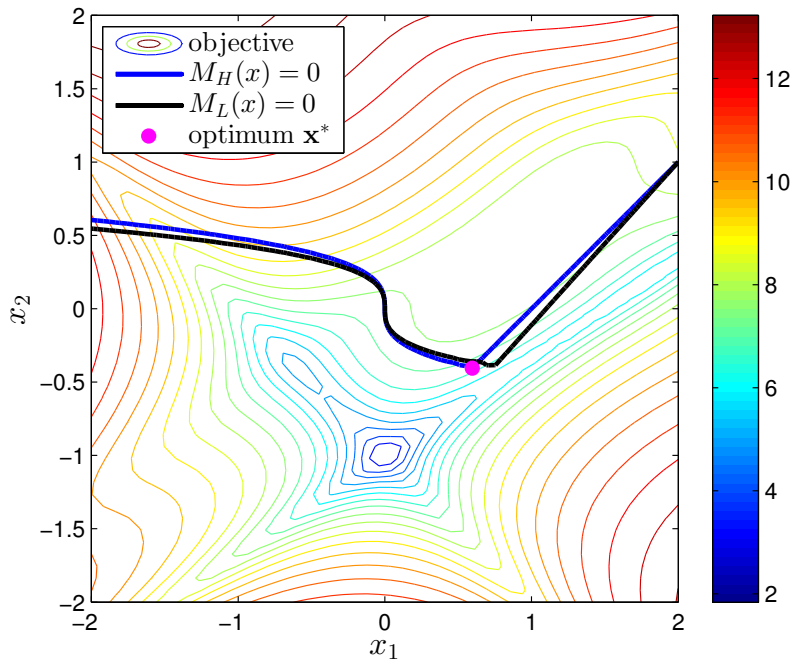

Figure 5.2: Two-dimensional optimization problem based on the Goldstein-Price function. The low- and high-fidelity constraint models impose similar restrictions on the feasible design space. The constrained optimum $\boldsymbol{x}^*$ according to the high-fidelity model is marked magenta.

and the high-fidelity constraint model classifies samples according to two constraint functions as proposed by Sasena (2002):

$$g_{H1}(\boldsymbol{x}) = -3x_1 + (-3x_2)^3 \tag{5.5}$$

$$g_{H2}(\boldsymbol{x}) = x_1 - x_2 - 1 \tag{5.6}$$

$$M_H(\boldsymbol{x}) = \max\{g_{H1}(\boldsymbol{x}), g_{H2}(\boldsymbol{x})\} \tag{5.7}$$

The low-fidelity model uses two similar functions to define feasibility:

$$g_{L1}(\boldsymbol{x}) = -3.5x_1 + (-3.5x_2)^3 \tag{5.8}$$

$$g_{L2}(\boldsymbol{x}) = x_1 - 0.9x_2 - 1.1 \tag{5.9}$$

$$M_L(\boldsymbol{x}) = \max\{g_{L1}(\boldsymbol{x}), g_{L2}(\boldsymbol{x})\} \tag{5.10}$$

Figure 5.2 shows the constraint boundaries corresponding to both models.

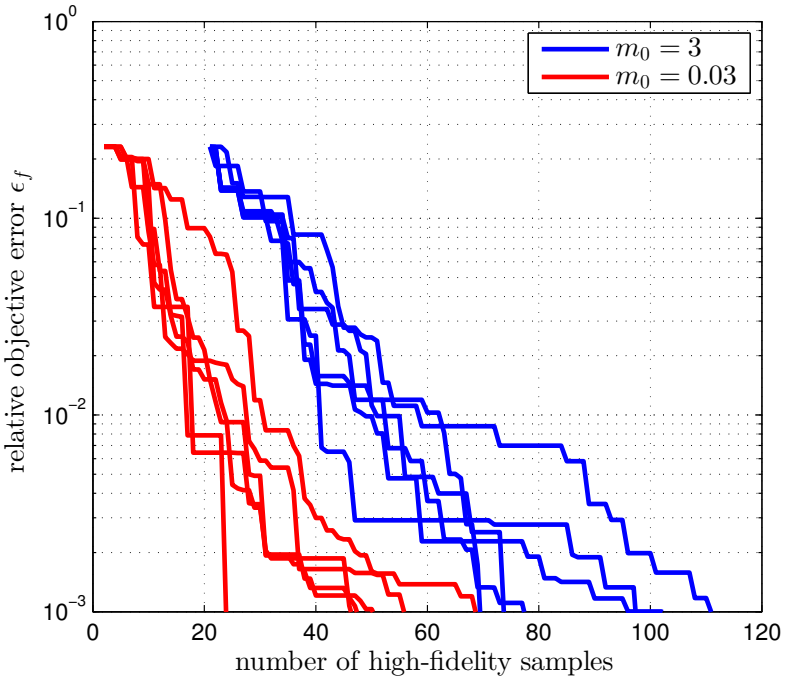

Figure 5.3: Evolution of the relative error (Equation 5.11) in objective function value of the best feasible sample with respect to the number of high-fidelity constraint evaluations. Multiple runs are shown for two values of initial margin.

To quantify the convergence of the optimization variant of the multi-fidelity algorithm, the following error measure considers the difference in objective function value between the actual optimum $\boldsymbol{x}^*$ and the current best sample $\boldsymbol{x}_k$ evaluated as feasible by the high-fidelity constraint.

$$\epsilon_f = \frac{f(\boldsymbol{x}_k) - f(\boldsymbol{x}^*)}{f(\boldsymbol{x}^*)} \tag{5.11}$$

Figure 5.3 summarizes the evolution of this error measure for multiple runs with both a small and a large initial margin. As may be expected based on Figure 5.2, taking advantage of the low-fidelity constraint boundary by selecting a small initial margin significantly reduces the number of high-fidelity samples required to converge to the constrained optimum.

5.2 Three-dimensional Steel Plate Problem

This test case for the algorithm revisits an earlier test problem introduced in Section 3.4. Again the design constraint imposes an upper limit on the first natural frequency of a rectangular steel plate described by its three dimensions. The high-fidelity model accounts for the effects of pre-stress, while the low-fidelity model does not (Equations 3.40 and 3.41). The design space is defined by Table 3.1 and the applied uniform tension on the perimeter is set to $T = 2000$ N/m.

For this design problem, the objective is to minimize the weight of the plate while satisfying the constraint on the first natural frequency. The objective function f is easily expressed in terms of the plate's density ρ and the design variables width (x_1), height (x_2), and thickness (x_3) of the plate:

$$f(\boldsymbol{x}) = \rho x_1 x_2 x_3 \tag{5.12}$$

Figure 5.4 shows the constraint boundaries corresponding to both models and the optimal design $\boldsymbol{x}^*$ derived analytically, and Figure 5.5 summarizes the evolution of the error measure for multiple runs with both a small and a large initial margin. As may be expected based on the results presented in Section 3.4, taking advantage of the low-fidelity constraint boundary by selecting a small initial margin significantly reduces the number of high-fidelity samples required to converge to the constrained optimum.

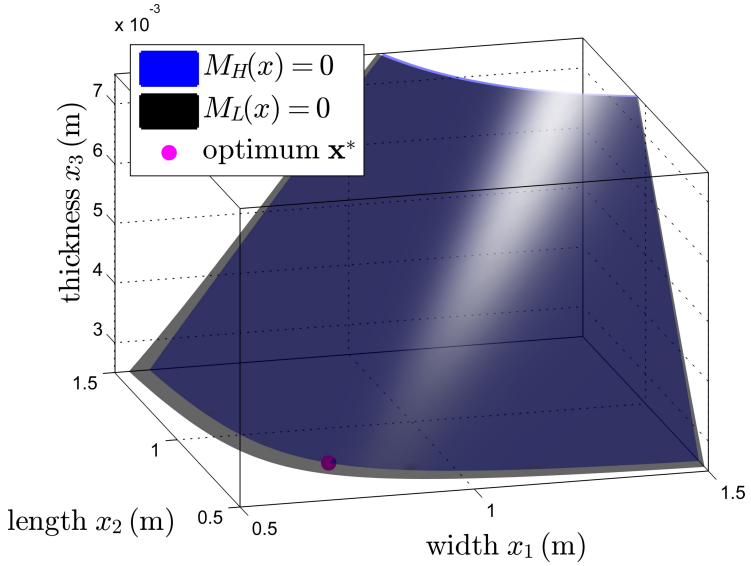

Figure 5.4: Two-dimensional optimization problem based on Goldstein-Price function. The low- and high-fidelity constraint model impose similar restrictions on the feasible design space. The constrained optimum $\boldsymbol{x}^*$ according to high-fidelity model is marked magenta.

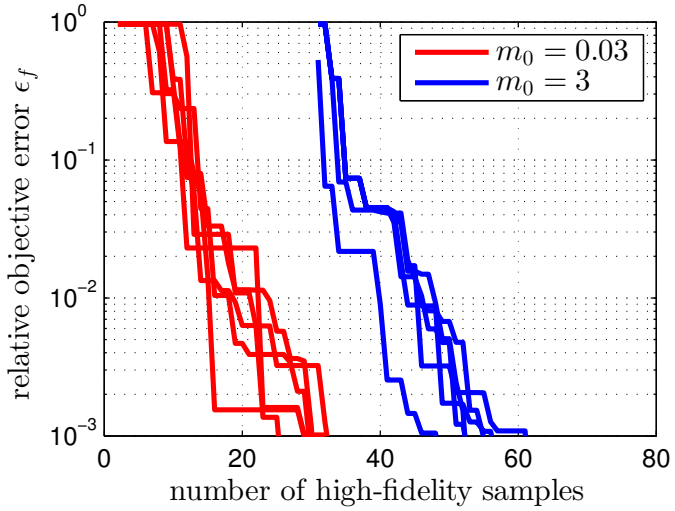

Figure 5.5: Evolution of the relative error (Equation 5.11) in objective function value of the best feasible sample with respect to the number of high-fidelity constraint evaluations. Taking the low-fidelity boundary into consideration ($m_0 = 0.03$) significantly reduces the number of high-fidelity samples required to converge to the constrained optimum.

5.3 Cantilevered Wing Problem

This last test case for the optimization variant of the multi-fidelity algorithm is identical to the cantilevered wing problem described in Section 4.2, augmented by an objective function to minimize the weight of the wing. This weight may be obtained from the finite-element structural model of the wing by summing the weight of each element:

$$f(\boldsymbol{x}) = \rho \sum_{k=1}^{N} A_k t_k \tag{5.13}$$

with area A_k and thickness t_k of shell element k of uniform density ρ. N denotes the total number of elements of the structural model. A reference stability boundary was obtained for the high-fidelity constraint model via a large number of adaptive samples (Section 4.2.1) via SVM. This provides an inexpensive, smooth, analytical function to obtain a reference solution of the optimization problem via gradient-based on optimization, which is listed in Table 5.1. Figure 5.6 shows a three-dimensional cross-section of the low- and high-fidelity stability boundaries at this reference solution. Figure 5.7 summarizes the evolution of the error measure (Equation 5.11) for multiple runs with both a small and a large initial margin. As may be expected based on the results in Section 4.2, taking advantage of the low-fidelity constraint boundary by selecting a small initial margin significantly reduces the number of high-fidelity samples required to converge to the constrained optimum.

Design Parameter	Lower Bound	Upper Bound	Optimum
Sweep angle of quarter chord $\Lambda_{1/4}$	$-25°$	$25°$	$7.74°$
Taper ratio $\lambda = c_t/c_r$	0.5	1.0	0.5
Semi span $b/2$	100 in	150 in	100 in
Thickness parameter k_1	0.5 in	2 in	0.603 in
Thickness parameter k_2	-2	0	-0.454

Table 5.1: Design variables defining the wing geometry. The optimal wing has minimum weight while satisfying the stability constraints.

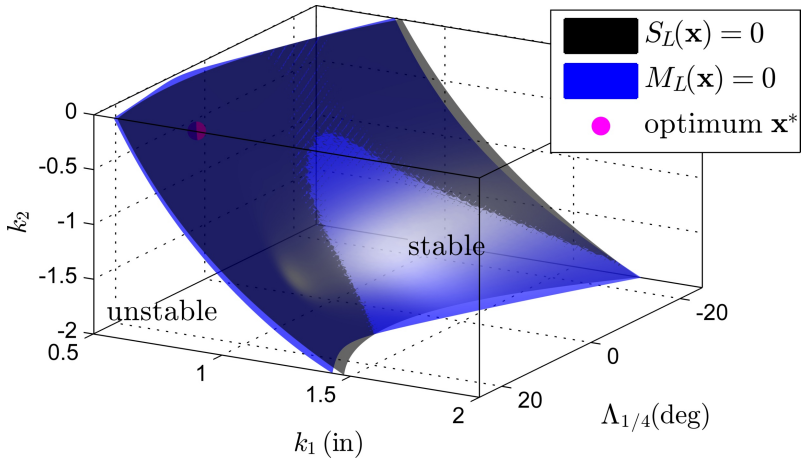

Figure 5.6: Three-dimensional cross-section of high- and low-fidelity stability boundaries at the optimal design.

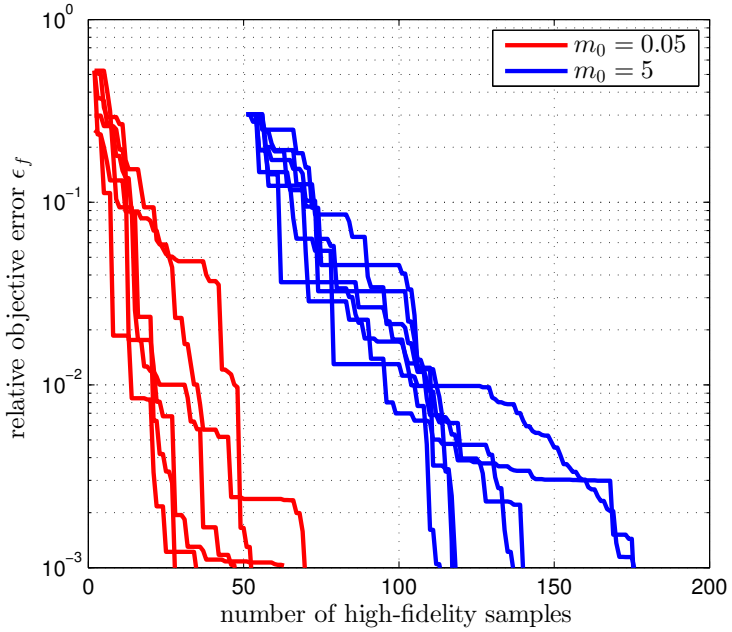

Figure 5.7: Evolution of the relative error (Equation 5.11) in objective function value of the best feasible sample with respect to the number of high-fidelity constraint evaluations. Taking the low-fidelity boundary into consideration ($m_0 = 0.05$) significantly reduces the number of high-fidelity samples required to converge to the constrained optimum.

CHAPTER 6

CONCLUSIONS

This chapter summarizes the conclusions on the proposed multi-fidelity algorithm and discusses its limitations to show opportunities for future improvements and extensions.

The multi-fidelity algorithm proposed in Chapter 3 enables the user to construct a support vector machine predictor (SVM) of design failure. To minimize simulation costs, training samples are selected iteratively and the algorithm chooses one of two levels of fidelity for each evaluation. Thereby, it addresses the challenges presented by design constraints that are expensive to evaluate and not effectively approximated by traditional meta-models due to discontinuous simulation responses. Further, since the SVM training process is based only on the classification of training samples as feasible or infeasible, it does not distinguish between various failure modes and therefore a single SVM may represent multiple design constraints. The resulting SVM function is an analytical, differentiable expression ideally suited for computational design methods, such as numerical optimization and reliability quantification.

The multi-fidelity algorithm is tested on various analytical test problems (Sections 3.4) as well as two simulation models to predict aeroelastic stability (Section 4). While the analytical problems are designed to study the performance of the algorithm in detail, the aeroelasticity models demonstrate the applicability of the algorithm to realistic engineering problems. It is found that the prediction error of the SVM constructed by the algorithm reliably converges towards zero as training samples are added iteratively. Specifically, the convergence is approximately exponential while the rate of convergence is problem dependent. The multi-fidelity algorithm takes advantage of a low-fidelity boundary to classify some of the SVM training samples and the test problems show that this multi-fidelity approach re-

duces the overall computational burden. The benefit of the multi-fidelity approach in terms of reducing the overall cost depends both of the accuracy of the low-fidelity boundary and the cost of obtaining it. For cases where the low-fidelity boundary represents a good approximation of the high-fidelity constraint model, the computational savings ranged from 10 to 60%. In addition, the third analytical test problem (Section 3.4) suggests that the benefit increases with the dimensionality of the design problem. On the other hand, the second analytical test problem (Section 3.4) demonstrates that even if the low-fidelity boundary is very inaccurate and therefore misleading to the multi-fidelity algorithm, the resulting penalty in terms of computational efficiency is small.

Chapter 5 presents a variant of the multi-fidelity algorithm specifically geared towards numerical design optimization that limits simulations to regions of the design space with the potential to improve on the current best, feasible design. The usefulness of this algorithm variant is limited to relatively low-dimensional optimization problems where the computational cost of the objective function is negligible compared to the evaluation cost of the constraints. However, for this sub-set of problems the efficiency of the algorithm is demonstrated both on analytical test problems and on the optimization of a cantilevered wing in terms of five geometrical parameters. Here the structural weight is minimized while satisfying an aeroelastic stability constraint and the convergence towards the constrained optimum is approximately exponential.

Several limitations of the algorithm present opportunities for future improvements. For example, it is assumed that the high-fidelity constraint model classifies samples consistently such that feasible and infeasible samples may be separated entirely by an SVM boundary. This assumption is generally justified in the case of simulation models, but if experimental data is incorporated, there might be several sources of uncertainty. This leads to non-separable data sets, where the best SVM approximation of the true boundary misclassifies some of the samples. Adapting the multi-fidelity algorithm for such a scenario would require major modifications to how assumptions on the accuracy of the low-fidelity boundary are generated and

how the SVM is constructed (Section 3.3.5).

In addition, the algorithm is not suited for very high-dimensional problems with, for example, hundreds of variables. This limitation is due to the large role of Euclidean distance in the iterative selection of training samples in the design space and also for the selection of fidelity levels. With increasing dimensionality, more and more adaptive samples would be located on the boundary of the design space, and convergence of the SVM to the actual boundary of the feasible space would likely to be very slow. However, with a different criterion for the selection of samples, the multi-fidelity approach may well be applicable to such problems.

REFERENCES

Abe, S. (2010). *Support Vector Machines for Pattern Classification*. Springer.

Aizerman, A., E. Braverman, and L. Rozoner (1964). Theoretical Foundations of the Potential Function Method in Pattern Recognition Learning. *Automation and remote control*, **25**, pp. 821–837.

Alexandrov, N., J. Dennis, R. Lewis, and V. Torczon (1998). A Trust-Region Framework for Managing the Use of Approximation Models in Optimization. *Structural and Multidisciplinary Optimization*, **15**(1), pp. 16–23. doi:10.1007/BF01197433.

Alexandrov, N., R. Lewis, C. Gumbert, L. Green, and P. Newman (2001). Approximation and Model Management in Aerodynamic Optimization with Variable-Fidelity Models. *Journal of Aircraft*, **38**(6), pp. 1093–1101.

Alexandrov, N. M., E. J. Nielsen, R. M. Lewis, and W. K. Anderson (2000). First-Order Model Management With Variable-Fidelity Physics Applied to Multi-Element Airfoil Optimization. Technical report, Nasa Langley Research Center.

Alpaydin, E. (2004). *Introduction to Machine Learning*. The MIT Press. ISBN 0262012111.

Antoine, C. and J. Kergomard (2008). *Acoustique des Instruments de Musique*. Belin.

Balabanov, V., R. T. Haftka, B. Grossman, W. H. Mason, and L. T. Watson (1998). Multifidelity Response Surface Model for HSCT Wing Bending Material Weight. In *7th AIAA/USAF/NASA/ISSMO Symposium on Multidisciplinary Analysis and Optimization*, AIAA–1998–4804, pp. 778–788.

Balabanov, V. and G. Venter (2004). Multi-Fidelity Optimization with High-Fidelity Analysis and Low-Fidelity Gradients. In *10 th AIAA/ISSMO Multidisciplinary Analysis and Optimization Conference*.

Bandler, J., Q. Cheng, S. Dakroury, A. Mohamed, M. Bakr, K. Madsen, and J. Sondergaard (2004). Space Mapping: The State of the Art. *Microwave Theory and Techniques, IEEE Transactions on*, **52**(1), pp. 337–361.

Barakat, N. and A. P. Bradley (2010). Rule Extraction from Support Vector Machines: A Review. *Neurocomputing*, **74**(13), pp. 178 – 190. ISSN 0925-2312. doi:10.1016/j.neucom.2010.02.016. ¡ce:title¿Artificial Brains¡/ce:title¿.

Basudhar, A. (2012). *Computational Optimal Design and Uncertainty Quantification of Complex Systems Using Explicit Decision Boundaries*. Ph.D. thesis, The University of Arizona.

Basudhar, A., C. Dribusch, S. Lacaze, and S. Missoum (2012). Constrained Efficient Global Optimization with Support Vector Machines. *Structural and Multidisciplinary Optimization*, **46**(2), pp. 201–221. ISSN 1615-147X. doi: 10.1007/s00158-011-0745-5. 10.1007/s00158-011-0745-5.

Basudhar, A. and S. Missoum (2010). An Improved Adaptive Sampling Scheme for the Construction of Explicit Boundaries. *Structural and Multidisciplinary Optimization*, **42**, pp. 517–529. ISSN 1615-147X. doi:10.1007/s00158-010-0511-0. 10.1007/s00158-010-0511-0.

Basudhar, A., S. Missoum, and S. Harrison (2008). Limit State Function Identification Using Support Vector Machines for Discontinuous Responses and Disjoint Failure Domains. *Probabilistic Engineering Mechanics*, **23**(1), pp. 1–11. ISSN 0266-8920. doi:10.1016/j.probengmech.2007.08.004.

Bennett, K. and C. Campbell (2000). Support Vector Machines: Hype or Hallelujah? *ACM SIGKDD Explorations Newsletter*, **2**(2), pp. 1–13.

Beran, P., T. Strganac, K. Kim, and C. Nichkawde (2004). Studies of Store-Induced Limit-Cycle Oscillations Using a Model with Full System Nonlinearities. *Nonlinear Dynamics*, **37**(4), pp. 323–339.

Berci, M., P. H. Gaskell, R. W. Hewson, and V. V. Toropov (2011). Multifidelity Metamodel Building as a Route to Aeroelastic Optimization of Flexible Wings. *Proceedings of the Institution of Mechanical Engineers, Part C: Journal of Mechanical Engineering Science*, **225**(9), pp. 2115–2137. doi: 10.1177/0954406211403549.

Berci, M., V. V. Toropov, R. W. Hewson, and P. Gaskell (2009). Metamodelling Based on High and Low Fidelity Model Interaction for UAV Gust Performance Optimization. In *50th AIAA/ASME/ASCE/AHS/ASC Structures, Structural Dynamics, and Materials Conference*, AIAA–2009–2215. AIAA, AIAA.

Bhatia, K. G. (2003). Airplane Aeroelasticity: Practice and Potential. *Journal of Aircraft*, **40**(6), pp. 1010–1018.

Bisplinghoff, R. L., H. Ashley, and R. L. Halfman (1962). *Aeroelasticity*. Dover, New York.

Boser, B., I. Guyon, and V. Vapnik (1992). A Training Algorithm for Optimal Margin Classifiers. In *Proceedings of the fifth annual workshop on Computational learning theory*, pp. 144–152. ACM.

Box, G. E. P. and N. R. Draper (1987). *Empirical Model-Building and Response Surfaces (Wiley Series in Probability and Statistics)*. John Wiley & Sons, New York. ISBN 0471810339.

Broomhead, D. and D. Lowe (1988). Multivariable Functional Interpolation and Adaptive Networks. *Complex systems*, **2**, pp. 321–355.

Byun, H. and S. Lee (2002). Applications of Support Vector Machines for Pattern Recognition: A Survey. *Pattern recognition with support vector machines*, pp. 571–591.

Carpenter, J. and J. Bithell (2000). Bootstrap Confidence Intervals: When, Which, What? A Practical Guide for Medical Statisticians. *Statistics in medicine*, **19**(9), pp. 1141–1164.

Chang, C.-C. and C.-J. Lin (2011). LIBSVM: A Library for Support Vector Machines. *ACM Trans. Intell. Syst. Technol.*, **2**(3), pp. 27:1–27:27. ISSN 2157-6904. doi:10.1145/1961189.1961199.

Chang, K. J., G. L. Giles, R. T. Haftka, and P.-J. Kao (1993). Sensitivity-Based Scaling for Approximating Structural Response. *Journal of Aircraft*, **30**(2), pp. 283–288. ISSN 0021-8669. doi:10.2514/3.48278.

Chapelle, O., V. Vapnik, O. Bousquet, and S. Mukherjee (2002). Choosing Multiple Parameters for Support Vector Machines. *Machine Learning*, **46**, pp. 131–159. ISSN 0885-6125. 10.1023/A:1012450327387.

Chen, P. (2000). Damping Perturbation Method for Flutter Solution: The G-Method. *AIAA journal*, **38**(9), pp. 1519–1524.

Clarke, S. M., J. H. Griebsch, and T. W. Simpson (2005). Analysis of Support Vector Regression for Approximation of Complex Engineering Analyses. *Journal of Mechanical Design*, **127**(6), pp. 1077–1087. doi:10.1115/1.1897403.

Cressie, N. (1990). The Origins of Kriging. *Mathematical Geology*, **22**, pp. 239–252. ISSN 0882-8121. 10.1007/BF00889887.

Cressie, N. (1993). *Statistics for Spatial Data*. Wiley series in probability and mathematical statistics: Applied probability and statistics. J. Wiley, 2 edition. ISBN 9780471002550.

Cristianini, N. and B. Schölkopf (2002). Support Vector Machines and Kernel Methods: The New Generation of Learning Machines. *Artificial Intelligence Magazine*, **23**(3), pp. 31–41.

Den Hertog, D., J. Kleijnen, and A. Siem (2005). The Correct Kriging Variance Estimated by Bootstrapping. *Journal of the Operational Research Society*, **57**(4), pp. 400–409.

Dixon, L. (1978). *Towards Global Optimisation 2*. Towards Global Optimisation. North-Holland Pub. Co. ISBN 9780444851710.

Dowell, E. and D. Tang (2002). Nonlinear Aeroelasticity and Unsteady Aerodynamics. *AIAA Journal*, **40**(9), pp. 1697–1707. doi:10.2514/2.1853.

Du, Q., V. Faber, and M. Gunzburger (1999). Centroidal Voronoi Tessellations: Applications and Algorithms. *SIAM Review*, **41**(4), pp. pp. 637–676. ISSN 00361445.

Duch, W. and N. Jankowski (1999). Survey of Neural Transfer Functions. *Neural Computing Surveys*, **2**(1), pp. 163–212.

Efron, B. (1983). Estimating the Error Rate of a Prediction Rule: Improvement on Cross-Validation. *Journal of the American Statistical Association*, pp. 316–331.

Efron, B. and R. Tibshirani (1993). *An Introduction to the Bootstrap*, volume 57. Chapman & Hall/CRC.

Eldred, M. S. and D. M. Dunlavy (2006). Formulations for Surrogate-Based Optimization with Data-Fit, Multifidelity and Reduced-Order Models. In *11 th AIAA/ISSMO Multidisciplinary Analysis and Optimization Conference*, AIAA–2006–7117. AIAA, AIAA.

Eldred, M. S., A. A. Giunta, S. S. Collis, N. A. Alexandrov, and R. M. Lewis (2004). Second-Order Corrections for Surrogate-Based Optimization with Model Hierarchies. In *Proceedings of the 10th AIAA/ISSMO Multidisciplinary Analysis and Optimization Conference*, 4457.

Fish, J. and T. Belytschko (2007). *A First Course in Finite Elements*. John Wiley & Sons. ISBN 9780470035801.

Floudas, C. and C. Gounaris (2009). A Review of Recent Advances in Global Optimization. *Journal of Global Optimization*, **45**, pp. 3–38. ISSN 0925-5001. 10.1007/s10898-008-9332-8.

Forrester, A. and D. Jones (2008). Global optimization of Deceptive Functions with Sparse Sampling. In *12th AIAA/ISSMO multidisciplinary analysis and optimization conference, Victoria, British Columbia, Canada*, pp. 10–12.

Forrester, A. I. and A. J. Keane (2009). Recent Advances in Surrogate-Based Optimization. *Progress in Aerospace Sciences*, **45**(1-3), pp. 50 – 79. ISSN 0376-0421. doi:10.1016/j.paerosci.2008.11.001.

Friedman, J., T. Hastie, and R. Tibshirani (2001). *The Elements of Statistical Learning*, volume 1. Springer Series in Statistics.

Fung, Y. (2002). *An Introduction to the Theory of Aeroelasticity*. Courier Dover Publications.

Furey, T., N. Cristianini, N. Duffy, D. Bednarski, M. Schummer, and D. Haussler (2000). Support Vector Machine Classification and Validation of Cancer Tissue Samples using Microarray Expression Data. *Bioinformatics*, **16**(10), pp. 906–914.

Gano, S., J. Renaud, J. Martin, and T. Simpson (2006). Update Strategies for Kriging Models Used in Variable Fidelity Optimization. *Structural and Multidisciplinary Optimization*, **32**(4), pp. 287–298. doi:10.1007/s00158-006-0025-y.

Gano, S., J. Renaud, and B. Sanders (2005). Hybrid Variable Fidelity Optimization by Using a Kriging-Based Scaling Function. *AIAA Journal*, **43**(11), pp. 2422–2433. doi:10.2514/1.12466.

Gibbs, M. (1997). *Bayesian Gaussian Processes for Regression and Classification*. Ph.D. thesis, Citeseer.

Giunta, A., V. Balabanov, M. Kaufman, S. Burgee, B. Grossman, R. Haftka, W. Mason, and L. Watson (1995a). Variable-Complexity Response Surface Design of an HSCT Configuration. In *Proceedings of ICASE/LaRC Workshop on Multidisciplinary Design Optimization, Hampton, VA*.

Giunta, A., R. Narducci, S. Burgee, B. Grossman, W. Mason, L. Watson, and R. Haftka (1995b). Variable-Complexity Response Surface Aerodynamic Design of an HSCT Wing. In *13th AIAA Applied Aerodynamics Conference*, AIAA–1995–1886. AIAA, AIAA.

Glaz, B., T. Goel, L. Liu, P. Friedmann, and R. Haftka (2009). Multiple-Surrogate Approach to Helicopter Rotor Blade Vibration Reduction. *AIAA Journal*, **47**, pp. 271–282. doi:10.2514/1.40291.

Goel, T., R. Haftka, W. Shyy, and N. Queipo (2007). Ensemble of Surrogates. *Structural and Multidisciplinary Optimization*, **33**, pp. 199–216. ISSN 1615-147X. 10.1007/s00158-006-0051-9.

Gunn, S. (1998). Support Vector Machines for Classification and Regression. Technical report, University of Southampton.

Gutmann, H.-M. (2001). A Radial Basis Function Method for Global Optimization. *Journal of Global Optimization*, **19**, pp. 201–227. ISSN 0925-5001. doi:10.1023/A:1011255519438. 10.1023/A:1011255519438.

Guzella, T. S. and W. M. Caminhas (2009). A Review of Machine Learning Approaches to Spam Filtering. *Expert Systems with Applications*, **36**(7), pp. 10206 – 10222. ISSN 0957-4174. doi:10.1016/j.eswa.2009.02.037.

Haftka, R. T. (1991). Combining Global and Local Approximations. *AIAA Journal*, **29**(9), pp. 1523–1525.

Haldar, A. and S. Mahadevan (2000). *Probability, Reliability, and Statistical Methods in Engineering Design*. John Wiley. ISBN 9780471331193.

Hall, P. (1986). On the Bootstrap and Confidence Intervals. *The Annals of Statistics*, **14**(4), pp. pp. 1431–1452. ISSN 00905364.

Hodges, D. and G. Pierce (2011). *Introduction to Structural Dynamics and Aeroelasticity*. Cambridge Aerospace Series. Cambridge University Press. ISBN 9780521195904.

Hodges, D. H. (2012). Book Review: Theoretical and Computational Aeroelasticity. *Journal of Aircraft*, **50**(4), pp. 990–991. doi:10.2514/1.J051738.

Huber, P. (1964). Robust Estimation of a Location Parameter. *The Annals of Mathematical Statistics*, **35**(1), pp. 73–101.

Hutchison, M. G., B. Grossman, R. T. Haftka, W. H. Mason, and E. R. Unger (1994). Variable-Complexity Aerodynamic Optimization of a High-Speed Civil Transport Wing. *Journal of Aircraft*, **31**(1), pp. 110–116. ISSN 0021-8669. doi:10.2514/3.46462.

Irwin, C. and P. Guyett (1965). The Subcritical Response and Flutter of a Swept-Wing Model. Technical Report 3497, United Kingdom Ministry of Technology, Aeronautical Research Council.

Joachims, T. (1998). Text Categorization With Support Vector Machines: Learning With Many Relevant Features. *Machine learning: ECML-98*, pp. 137–142.

Jones, D. (2001). A Taxonomy of Global Optimization Methods Based on Response Surfaces. *Journal of Global Optimization*, **21**(4), pp. 345–383.

Jones, D., M. Schonlau, and W. Welch (1998). Efficient Global Optimization of Expensive Black-Box Functions. *Journal of Global optimization*, **13**(4), pp. 455–492.

Karlsen, R., D. Gorsich, and G. Gehart (2000). Target Classification Via Support Vector Machines. *Optical Engineering*, **39**(3), pp. 704–711. doi:10.1117/1.602417.

Karush, W. (1939). *Minima of Functions of Several Variables with Inequalities as Side Constraints*. Master's thesis, Dept. of Mathematics, Univ. of Chicago.

Kaufman, M., V. Balabanov, A. A. Giunta, B. Grossman, W. H. Mason, S. L. Burgee, R. T. Haftka, and L. T. Watson (1996). Variable-Complexity Response Surface Approximations for Wing Structural Weight in HSCT Design. *Computational Mechanics*, **18**(2), pp. 112–126. doi:10.1007/BF00350530.

Keane, A. (2003). Wing Optimization Using Design of Experiment, Response Surface, and Data Fusion Methods. *Journal of Aircraft*, **40**(4), pp. 741–750.

Keane, A. and P. Nair (2005). *Computational Approaches for Aerospace Design*. Wiley Online Library. doi:10.1002/0470855487.fmatter.

Kleijnen, J. (2009). Kriging Metamodeling in Simulation: A Review. *European Journal of Operational Research*, **192**(3), pp. 707–716.

Kleijnen, J., W. van Beers, and I. van Nieuwenhuyse (2012). Expected Improvement in Efficient Global Optimization Through Bootstrapped Kriging. *Journal of Global Optimization*, **54**, pp. 59–73. ISSN 0925-5001. 10.1007/s10898-011-9741-y.

Knill, D. L., A. A. Giunta, C. A. Baker, B. Grossman, W. H. Mason, R. T. Haftka, and L. T. Watson (1998). HSCT Configuration Design Using Response Surface Approximations of Supersonic Euler Aerodynamics. In *36th Aerospace Sciences Meeting and Exhibit*, AIAA-1998-0905. AIAA, AIAA.

Koehler, J. and A. Owen (1996). Computer Experiments. *Handbook of statistics*, **13**(13), pp. 261–308.

Kousen, K. and O. Bendiksen (1994). Limit Cycle Phenomena in Computational Transonic Aeroelasticity. *Journal of Aircraft*, **31**(6), pp. 1257–1263. doi:10.2514/3.46644.

Koziel, S., Q. Cheng, and J. Bandler (2008). Space Mapping. *Microwave Magazine, IEEE*, **9**(6), pp. 105 –122. ISSN 1527-3342. doi:10.1109/MMM.2008.929554.

Krige, D. G. (1951). A Statistical Approach to Some Basic Mine Valuation Problems on the Witwatersrand. *Journal of the Chemcial, Metallurgical and Mining Society of South Africa*, **52**, pp. 119–139.

Kuhn, H. W. and A. W. Tucker (1951). Nonlinear Programming. In *Second Berkeley symposium on mathematical statistics and probability*, volume 1, pp. 481–492.

Lachenbruch, P. and M. Mickey (1968). Estimation of Error Rates in Discriminant Analysis. *Technometrics*, pp. 1–11.

Leary, S. J., A. Bhaskar, and A. J. Keane (2003). A Knowledge-Based Approach To Response Surface Modelling in Multifidelity Optimization. *Journal of Global Optimization*, **26**(3), pp. 297–319. doi:10.1023/A:1023283917997.

Lee, B., L. Jiang, and Y. Wong (1999a). Flutter of an Airfoil with Cubic Restoring Force. *Journal of Fluids and Structures*, **13**(1), pp. 75–101. doi:10.1006/jfls.1998.0190.

Lee, B., S. Price, and Y. Wong (1999b). Nonlinear Aeroelastic Analysis of Airfoils: Bifurcation and Chaos. *Progress in Aerospace Sciences*, **35**(3), pp. 205–334. doi:10.1016/S0376-0421(98)00015-3.

Li, H., Y. Liang, and Q. Xu (2009). Support Vector Machines and Its Applications in Chemistry. *Chemometrics and Intelligent Laboratory Systems*, **95**(2), pp. 188–198.

Lloyd, S. (1982). Least Squares Quantization in PCM. *Information Theory, IEEE Transactions on*, **28**(2), pp. 129 – 137. ISSN 0018-9448. doi:10.1109/TIT.1982.1056489.

Martin, J. and T. Simpson (2005). Use of Kriging Models to Approximate Deterministic Computer Models. *AIAA journal*, **43**(4), pp. 853–863.

McKay, M., R. Beckman, and W. Conover (1979). A Comparison of Three Methods for Selecting Values of Input Variables in the Analysis of Output from a Computer Code. *Technometrics*, pp. 239–245.

Min, J. and Y. Lee (2005). Bankruptcy Prediction Using Support Vector Machine with Optimal Choice of Kernel Function Parameters. *Expert systems with applications*, **28**(4), pp. 603–614.

Missoum, S., C. Dribusch, and P. Beran (2010). Reliability-Based Design Optimization of Nonlinear Aeroelasticity Problems. *Journal of Aircraft*, **47**(3), pp. 992–998. doi:10.2514/1.46665.

Mohandes, M., T. Halawani, S. Rehman, and A. A. Hussain (2004). Support Vector Machines for Wind Speed Prediction. *Renewable Energy*, **29**(6), pp. 939 – 947. ISSN 0960-1481. doi:10.1016/j.renene.2003.11.009.

Mountrakis, G., J. Im, and C. Ogole (2011). Support Vector Machines in Remote Sensing: A Review. *ISPRS Journal of Photogrammetry and Remote Sensing*, **66**(3), pp. 247–259.

Myers, R., D. Montgomery, and C. Anderson-Cook (2009). *Response Surface Methodology: Process and Product Optimization Using Designed Experiments*, volume 705. John Wiley & Sons Inc.

Myers, R. H. and D. C. Montgomery (1995). *Response Surface Methodology: Process and Product Optimization Using Designed Experiments*. Wiley-Interscience, 1 edition.

Nocedal, J. and S. Wright (2006). *Numerical Optimization*. Springer series in operations research. Springer. ISBN 9780387303031.

Noll, T., J. Brown, M. Perez-Davis, S. Ishmael, G. Tiffany, and M. Gaier (2004). Investigation of the Helios Prototype Aircraft Mishap Volume I Mishap Report. Technical report, NASA.

Okabe, A., B. Boots, K. Sugihara, and S. Chiu (1992). *Spatial Tessellations: Concepts and Applications of Voronoi Diagrams*. Wiley & Sons Chichester.

Orr, G., W. Pettersson-Yeo, A. F. Marquand, G. Sartori, and A. Mechelli (2012). Using Support Vector Machine to Identify Imaging Biomarkers of Neurological and Psychiatric Disease: A Critical Review. *Neuroscience & Biobehavioral Reviews*, **36**(4), pp. 1140 – 1152. ISSN 0149-7634. doi:10.1016/j.neubiorev.2012.01.004.

Parr, J. M., A. J. Keane, A. I. Forrester, and C. M. Holden (2012). Infill Sampling Criteria for Surrogate-Based Optimization with Constraint Handling. *Engineering Optimization*, **0**(0), pp. 1–20. doi:10.1080/0305215X.2011.637556.

Patil, M., D. Hodges, and C. Cesnik (2001). Limit-Cycle Oscillations in High Aspect Ratio Wings. *Journal of Fluids and Structures*, **15**(1), pp. 107–132.

Plackett, R. and J. Burman (1946). The Design of Optimum Multifactorial Experiments. *Biometrika*, **33**(4), pp. 305–325.

Queipo, N., R. Haftka, W. Shyy, T. Goel, R. Vaidyanathan, and P. Kevin Tucker (2005). Surrogate-Based Analysis and Optimization. *Progress in Aerospace Sciences*, **41**(1), pp. 1–28. doi:10.1016/j.paerosci.2005.02.001.

Ralston, A. and P. Rabinowitz (1978). *A first Course in Numerical Analysis*. International series in pure and applied mathematics. McGraw-Hill. ISBN 9780070511583.

Redhe, M. and L. Nilsson (2006). A Multipoint Version of Space Mapping Optimization Applied to Vehicle Crashworthiness Design. *Structural and Multidisciplinary Optimization*, **31**, pp. 134–146. ISSN 1615-147X. 10.1007/s00158-005-0544-y.

Robinson, T. (2007). *Surrogate-Based Optimization Using Multifidelity Models with Variable Parameterization*. Ph.D. thesis, Massachusetts Institute of Technology.

Robinson, T., M. Eldred, K. Willcox, and R. Haimes (2006a). Strategies for Multifidelity Optimization with Variable Dimensional Hierarchical Models. In *Proceedings of the 47th AIAA/ASME/ASCE/AHS/ASC Structures, Structural Dynamics, and Materials Conference (2nd AIAA Multidisciplinary Design Optimization Specialist Conference), Newport, RI*, pp. 2006–1819.

Robinson, T., M. Eldred, K. Willcox, and R. Haimes (2008). Surrogate-Based Optimization Using Multifidelity Models with Variable Parameterization and Corrected Space Mapping. *Aiaa Journal*, **46**(11), pp. 2814–2822.

Robinson, T., K. Willcox, M. Eldred, and R. Haimes (2006b). Multifidelity Optimization for Variable-Complexity Design. In *11th AIAA/ISSMO Multidisciplinary Analysis and Optimization Conference*, AIAA–2006–7114. AIAA, AIAA.

Rodden, W. (2011). *Theoretical and Computational Aeroelasticity*. Crest Publishing. ISBN 9780692012413.

Rodden, W. and E. Johnson (1994). *MSC/NASTRAN Aeroelastic Analysis: User's Guide, Version 68*. MacNeal-Schwendler Corporation.

Rodden, W. and J. Love (1985). Equations of Motion of a Quasisteady Flight Vehicle Utilizing Restrained Static Aeroelastic Characteristics. *Journal of Aircraft*, **22**(9), pp. 802–809. doi:10.2514/3.45205.

Rodden, W. P., R. L. Harder, and E. D. Bellinger (1979). Aeroelastic Addition to Nastran. Technical Report 3094, NASA.

Sacks, J., S. Schiller, and W. Welch (1989a). Designs for Computer Experiments. *Technometrics*, pp. 41–47.

Sacks, J., W. Welch, T. Mitchell, and H. Wynn (1989b). Design and Analysis of Computer Experiments. *Statistical science*, **4**(4), pp. 409–423.

Saijal, K., R. Ganguli, and S. Viswamurthy (2011). Optimization of Helicopter Rotor Using Polynomial and Neural Network Metamodels. *Journal of Aircraft*, **48**(2), pp. 553–566. doi:10.2514/1.53495.

Sasena, M. J. (2002). *Flexibility and Efficiency Enhancements for Constrained Global Design Optimization with Kriging Approximations*. Ph.D. thesis, Citeseer.

Schölkopf, B., C. J. C. Burges, and A. J. Smola (eds.) (1998). *Advances in Kernel Methods*. The MIT Press.

Schölkopf, B. and A. Smola (2001). *Learning with Kernels: Support Vector Machines, Regularization, Optimization, and Beyond*. MIT press.

Scholkopf, B., K.-K. Sung, C. Burges, F. Girosi, P. Niyogi, T. Poggio, and V. Vapnik (1997). Comparing Support Vector Machines with Gaussian Kernels to Radial Basis Function Classifiers. *Signal Processing, IEEE Transactions on*, **45**(11), pp. 2758 –2765. ISSN 1053-587X. doi:10.1109/78.650102.

Schuster, D. M., D. D. Liu, and L. J. Huttsell (2003). Computational Aeroelasticity: Success, Progress, Challenge. *Journal of Aircraft*, **40**(5), pp. 843–856. doi:10.2514/2.6875.

Seydel, R. (1988). *From Equilibrium to Chaos: Practical Bifurcation and Stability Analysis*. Elsevier Science Ltd.

Simpson, T., J. Poplinski, P. N. Koch, and J. Allen (2001). Metamodels for Computer-Based Engineering Design: Survey and Recommendations. *Engineering with Computers*, **17**, pp. 129–150. ISSN 0177-0667. 10.1007/PL00007198.

Sóbester, A. (2003). *Enhancements to Global Design Optimization Techniques*. Ph.D. thesis, University of Southampton.

Stone, M. (1974). Cross-Validatory Choice and Assessment of Statistical Predictions. *Journal of the Royal Statistical Society. Series B (Methodological)*, **36**(2), pp. pp. 111–147. ISSN 00359246.

Swiler, L., R. Slepoy, and A. Giunta (2006). Evaluation of Sampling Methods in Constructing Response Surface Approximations. In *Proc. 47th AIAA/ASME/ASCE/AHS/ASC Structures, Structural Dynamics, and Materials Conference, number AIAA-2006-1827, Newport, RI*.

Theodorson, T. (1935). General Theory of Aerodynamic Instability and the Mechanism of Flutter. Technical Report 496, National Advisory Commitee for Aeronautics.

Toropov, V., V. Markine, P. Meijers, and J. Meijaard (1997). Optimization of a Dynamic System Using Multipoint Approximations and Simplified Numerical Model. In *Proceedings of the Second World Congress of Structural and Multidisciplinary Optimization*, pp. 613–618. Polish Academy of Sciences.

Toropov, V. V. and E. Van der Giessen (1993). Parameter Identification for Nonlinear Constitutive Models: Finite Element Simulation–Optimization–Nontrivial Experiments. In Pedersen, P. (ed.) *Proceedings of IUTAM Symposium on Optimal Design of Advanced Materials, The Frithiof I. Niordson Volume*, pp. 113–130. IUTAM, Elesevier Scientific Publishers, Amsterdam.

Unger, E., M. Hutchinson, X. Huang, W. Mason, R. Haftka, and B. Grossmann (1992). Variable-Complexity Aerodynamic-Structural Design of a High-Speed

Civil Transport. In *4th AIAA/NASA/USAF/OAI Symposium on Multidisciplinary Analysis and Optimization*, AIAA–1992–4695. AIAA, AIAA.

Vanderplaats (2006). *Genesis Analysis Manual Version 9.0*. Vanderplaats Research & Developement, Inc.

Vanderplaats, G. (2005). *Numerical Optimization Techniques for Engineering Design*. Vanderplaats Research & Development, Incorporated. ISBN 9780944956021.

Vapnik, V. (1963). Pattern Recognition Using Generalized Portrait Method. *Automation and Remote Control*, **24**, pp. 774–780.

Vapnik, V. (1995). *The Nature of Statistical Learning Theory*. Springer-Verlag New York Inc.

Vapnik, V. (1998). *Statistical Learning Theory*. Adaptive and learning systems for signal processing, communications, and control. Wiley. ISBN 9780471030034.

Vapnik, V., S. Golowich, and A. Smola (1996). Support Vector Method for Function Approximation, Regression Estimation, and Signal Processing. In *Advances in Neural Information Processing Systems 9*. Citeseer.

Viana, F. (2011). *Multiple Surrogates for Prediction and Optimization*. Ph.D. thesis, University of Florida.

Viana, F., R. Haftka, and V. Steffen (2009). Multiple Surrogates: How Cross-Validation Errors Can Help Us to Obtain the Best Predictor. *Structural and Multidisciplinary Optimization*, **39**, pp. 439–457. ISSN 1615-147X. 10.1007/s00158-008-0338-0.

Viana, F. A. C., G. Venter, and V. Balabanov (2010). An Algorithm for Fast Optimal Latin Hypercube Design of Experiments. *International Journal for Numerical Methods in Engineering*, **82**(2), pp. 135–156. ISSN 1097-0207. doi:10.1002/nme.2750.

Voronoi, G. (1908). Nouvelles Applications des Paramtres Continus la Thorie des Formes Quadratiques. Premier Mmoire. Sur Quelques Proprits des Formes Quadratiques Positives Parfaites. *Journal fr die reine und angewandte Mathematik (Crelle's Journal)*, **1908**(133), pp. 97–102. doi:10.1515/crll.1908.133.97.

Welch, W., R. J. Buck, J. Sacks, H. Wynn, T. Mitchell, and M. Morris (1992). Screening, Predicting, and Computer Experiments. *Technometrics*, pp. 15–25.

Welch, W., T. Yu, S. Kang, and J. Sacks (1990). Computer Experiments for Quality Control by Parameter Design. *Journal of Quality Technology*, **22**(1), pp. 15–15.

Wolfe, P. (1961). A Duality Theorem for Nonlinear Programming. *Quarterly of applied mathematics*, **19**(3), pp. 239–244.

Wright, J. and J. Cooper (2007). *Introduction to Aircraft Aeroelasticity and Loads*. Aerospace Series. John Wiley & Sons. ISBN 9780470858400.

Ye, K., W. Li, and A. Sudjianto (2000). Algorithmic Construction of Optimal Symmetric Latin Hypercube Designs. *Journal of statistical planning and inference*, **90**(1), pp. 145–159. doi:10.1016/S0378-3758(00)00105-1.

Zien, A., G. Rtsch, S. Mika, B. Schlkopf, T. Lengauer, and K.-R. Mller (2000). Engineering Support Vector Machine Kernels That Recognize Translation Initiation Sites. *Bioinformatics*, **16**(9), pp. 799–807. doi:10.1093/bioinformatics/16.9.799.

Zona (2011). *ZAERO Theoretical Manual Version 8.5*. ZONA Technology Inc, 21st edition.